Max Planck Graduate Center
mit der Johannes Gutenberg-Universität Mainz

JG|U

3D-ultrastructure, functions and stress responses of rhogocytes from the freshwater gastropods *Biomphalaria glabrata* and *Lymnaea stagnalis*

Dissertation zur Erlangung des Grades
"Dr. rer. nat."
an der Johannes Gutenberg-Universität Mainz

Maria Kokkinopoulou
geb. am 26.04.1984 in Thessaloniki, Griechenland

Mainz, Dezember 2014

Dekan: [redacted]

1. Berichterstatter: [redacted]
2. Berichterstatter: [redacted]
3. Berichterstatter: [redacted]

Tag der mündlichen Prüfung: 09.03.2015

΄Αν ο ένας δρόμος είναι καλύτερος απ΄ τον άλλο,
να είσαι σίγουρος ότι αυτός είναι ο δρόμος της φύσης

'If one way be better than another, that you may be sure is nature's way'
Aristoteles, De incessu animalium 704 b 14-18

Contents

Abbreviations

μm	micrometer
3D	three dimensional
Å	Angstrom
A	adenine
AP	alkaline phosphatase
BCIP	5-bromo-4-chloro-3-indoxyl phosphate
Bg	*Biomphalaria glabrata*
BgAChBP	*Biomphalaria glabrata* acetylcholine-binding protein
BgHb	*Biomphalaria glabrata* hemoglobin
BSA	bovine serum albumin
CCD	charge-coupled device
$CdCl_2$	cadmium chloride
cDNA	complementary DNA
DIG	digoxigenin
DNA	deoxyribonucleic acid
EDTA	ethylendiaminetetraacetic acid
EDX	energy-dispersive X-ray spectroscopy
FEG	field emission gun
FU	functional unit
G	guanine
h	hour

H_2O_2	hydrogen peroxide
H & E	hematoxylin and eosin
HCl	hydrochloric acid
KH_2PO_4	monopotassium phosphate
KOH	potassium hydroxide
LaB_6	lanthanum hexaboride
LB medium	lysogeny broth medium
LsH	*Lymnaea stagnalis* hemocyanin
MAB	maleic acid buffer
$MgCl_2$	magnesium chloride
$MgSO_4$	magnesium sulfate
min	minute
MOPS	3-(N-morpholino)propanesulfonic acid
MP	movat pentachrome
Na_2HPO_4	disodium phosphate
NaCl	sodium chloride
NBT	nitro blue tetrazolium chloride
nm	nanometer
O_2	oxygen
OsO_4	osmium tetroxide
PBS	phosphate buffer saline
PCR	polymerase chain reaction
PPE	poly(2.6-dimethyl-1.4-phenylene ether)

RNA	ribonucleic acid
RT	reverse transcriptase
s	seconds
SDS	sodium lauryl sulfate
SSC	saline sodium citrate
STEM	scanning transmission electron microscopy/microscope
T	thymine
TBE	Tris-borate
TEM	transmission electron microscopy/microscope
U	uracil
UA	uranyl acetate

Part I.

Introduction

1. Transmission electron microscopy of tissue samples

In 1926, Louis de Broglie discovered that electrons, negatively charged point-like particles, which had both particle and wave characteristics, could be accelerated to a high speed in vacuum by an electrostatic field. The electrons have a wavelength substantially less than visible light (100,000 times smaller).

The first transmission electron microscope (TEM) was built based on these characteristics in 1931 by Ernst Ruska (University of Berlin). Nowadays, a TEM has magnetic lenses (the number of which depends on the model) and a resolution of 0.1 nm (= 1 Å) at achievable magnifications of over 1 million times (Fig. 1.1). Resolution is the smallest distance between two points that the eyes can resolve; it is about 100 μm with the nacked eye and 100 nm with the light microscope (Williams & Carter, 1996). The source of the electrons in the TEM is an electron gun. It comprises a filament which is heated to 2700 °C, a Wehnelt cylinder and an anode. Two other sources of electrons that are brighter are the lanthanum hexaboride (LaB_6) gun and the field emission gun (FEG). The electrons travel in vacuum (otherwise they would collide with residual gas atoms) inside the electromagnetic field and they hit the specimen (object of interest). Apertures stop the electrons that are not required for image formation. The electron microscope is equipped with a goniometer, which is a specimen stage that can provide tilting around one or two axes and rotation around the optical axis. This gives more information for understanding the structural organization.

The electrons hit the sample on their way to a fluorescent screen, which emits visible light when hit by the electrons. In the standard TEM, two phenomena contribute to the image formation: the amplitude contrast (electrons that are absorbed) and the phase contrast (electrons that are scattered over small angles). Modern technology has provided CCD (charge-coupled device) cameras that enable scientists to record images directly in a digital form. However, for collecting high resolution data many laboratories still favour films because of their large size and high resolution properties. Furthermore, the construction of phase plates allows the improvement of the contrast by shifting the phase of the unscattered electrons.

Nowadays, there are many different techniques used for sample preparation for the TEM. The most widely applied method is chemical fixation that preserves many cellular components. The samples are embedded in water-insoluble resins and contrasted with heavy metals. Alternatively, in order to keep the samples at close-to-native conditions, they can be cooled rapidly by high pressure freezing, so

that the water molecules are practically immobilized before ice crystals can start to form. This technique can be followed by freeze substitution. This means that the cryofixed samples are put into an organic substitution medium and brought slowly to room temperatures, while being embedded in resins. (For more details on sample preparation techniques see Part II)

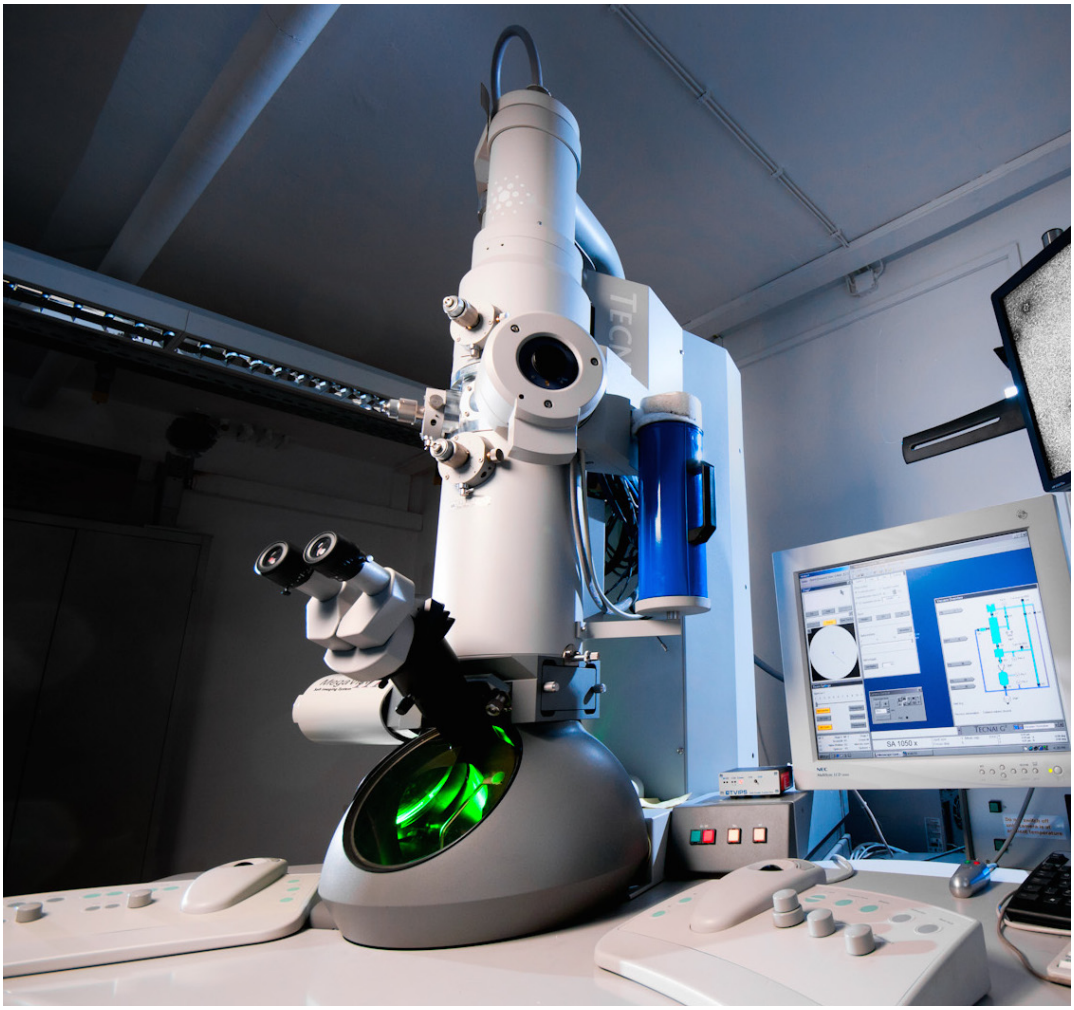

Figure 1.1. ***Transmission electron microscope Tecnai12*** *(image C. Kühne)*

2. Molluscs

The molluscs compose the second largest phylum of invertebrate animals. The term 'mollusc' is derived from the latin word *mollis* for soft. The number of living species is estimated to more than 100,000. They are important members of many marine, limnic and terrestrial habitats. The molluscs are divided in several taxonomic classes from which the Gastropoda (limpets, snails and slugs) comprise the largest group. The gastropod body consists of four basic parts: head, foot, visceral mass and mantle. The mantle is the dorsal body wall that often protrudes like a cloak to form a mantle cavity. In many species it secretes a hard calcium carbonate shell. The mantle is used for breathing, excretion and other vital processes. The foot contains the locomotory muscles. The visceral mass that is located above the foot contains the digestive system, the heart and other internal organs. Besides sensory organs, brain and mouth, the head contains a specific molluscan organ termed the radula, a rasping tongue with chitinous teeth. Most gastropods transport oxygen in their hemolymph using hemocyanin, a large extracellular copper protein. In a single taxon of freshwater snails, the Planorbidae, a large extracellular hemoglobin is used instead (Lieb et al., 2006).

3. Rhogocytes (Pore Cells)

Rhogocytes are prominent pore cells, either embedded in the connective tissue or circulating freely in the hemolymph of gastropods and other molluscan taxa (Haszprunar, 1996). The rhogocytes are dynamic cells that follow the physiological conditions of the animal. The entire cell is surrounded by an external basal lamina-like membrane, often composed of collagen fibers (Plummer, 1966), which prevents connection to the neighboring cells and suggests a mesenchymal origin of this cell type. Rhogocytes are often found in clusters. Their plasma membrane shows many invaginations, occasionally containing granular material. These extracellular lacunae (also called 'subsurface cisternae') are covered by cytoplasmic bars, forming slits of 20 nm width (Fig. 3.1-3.3). The slits are bridged by a thin diaphragm (Sminia, 1972; Albrecht et al., 2001). The name 'rhogocyte' (proposed by Fioroni et al., 1984) points out exactly this unique characteristic structure, because the greek word *rhogos* means 'slit'. Other proposed names for these cells are pore cells, Leydig cells, cellulae nucale, Blasenzellen or brown cells (reviewed by Haszprunar, 1996).

Rhogocytes appear in different size and shape. They can reach up to 30 μm in length, and can be round, elongated or irregularly shaped. They are easily identified at a lower magnification due to their well-developed endoplasmic reticulum and a rather large nucleus, containing a prominent nucleolus. No cell polarity is observed. Mitochondria and Golgi bodies are scattered through the cytoplasm. They show numerous electron dense granula and secretory vesicles (Sminia, 1972). The vacuoles are probably the site of material storage and accumulation. Vesicles on the other hand are involved in the transport and degeneration of materials, as some exhibit lysosomal activity (Jones & Bowen, 1979; Martin et al., 2011). The area below the cytoplasmic bars often contains floccular material (Plummer, 1966; Sminia et al., 1972; Jones & Bowen, 1979).

Several ideas have been proposed so far regarding the biological functions of rhogocytes. Their most obvious function is hemocyanin biosynthesis. This was guessed from electron microscopical images (Skelding & Newell, 1975; Sminia & Boer, 1973; Sminia & Vlugt-van Daalen, 1977; Wood et al., 1981) and experimentally proven by *in situ* hybridization (Albrecht et al., 2001; Martin et al., 2011). Hemocyanin is the extracellular oxygen carrier in the hemolymph of many molluscs (reviewed by Markl, 2013). But there is another snail family, the Planorbidae, for example *Biomphalaria glabrata* and *Planorbarius corneus*, that use a multimeric hemoglobin for oxygen (O_2) transport (for its molecular structure and function, see Lieb et al., 2006). The site of hemoglobin synthesis is still not known, but rhogocytes are good candidates, as proposed by Sminia et al. (1972).

Furthermore, rhogocytes play an important role in metal ion homeostasis (Marigomez et al., 2002), are involved in transport and storage of nutrients (Sminia, 1972; Bani et al., 1990; Haszprunar, 1996) and act in detoxification (Marigomez, 1990) and defense systems (Meister, 1977). They participate in calcium mobilization for shell formation (Fournie & Chetail, 1982). Additionally, they synthesize and release tropocollagen (Plummer, 1966). After it is released from the cell, the tropocollagen begins to polymerize forming thin collagen fibrils. Jones & Bowen (1979) identified three types of rhogocytes, all of which synthesize collagen. A secondary function of rhogocytes as a site for polysaccharide storage was discussed by Sminia (1972).

Direct homologues of rhogocytes have not been identified in other animal phyla (Haszprunar, 1996), but it is proposed that they have a common phylogenetic basis with mammalian podocytes and insect nephrocytes (Boer & Sminia 1976; Haszprunar 1996; Weavers et al., 2009). This suggestion is based on their morphological similarities, such as the slit apparatus with the diaphragms, the pores of the slits and the surrounding basal lamina-like structure (Boer & Sminia 1976; Haszprunar 1996; Weavers et al., 2009). The relatedness of podocytes and nephrocytes is proven by the identification of common slit diaphragm proteins (Zhuang et al., 2009). A recent study of Stewart et al. (2014) on larval rhogocytes demonstrated their relationship to protonephridia.

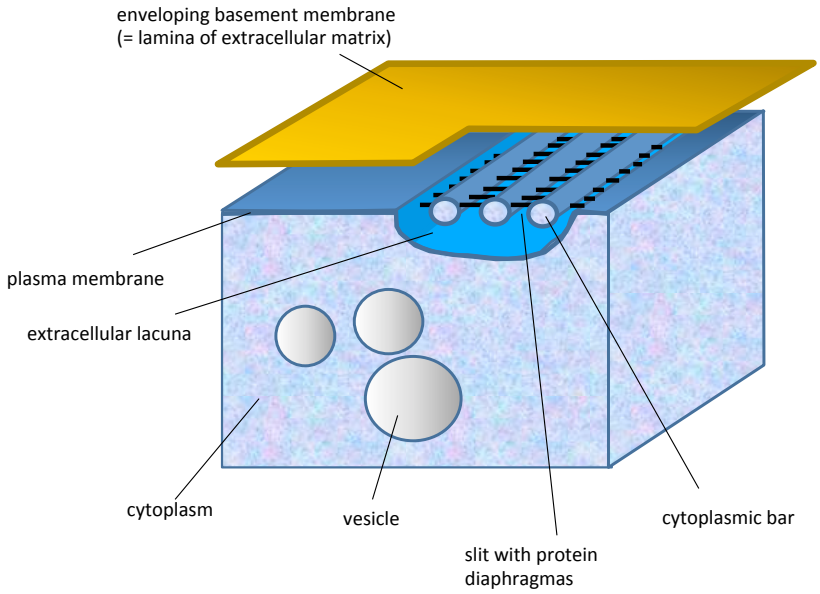

Figure 3.1. ***Rhogocyte structure.*** *Lamina of extracellular matrix = enveloping basement membrane (m), plasma membrane = cell membrane (c), extracellular lacuna (e), slit (s), diaphragma (d), cytoplasmic bar (b), vesicle (v) and cytoplasm (cp). (Graphic:J. Markl)*

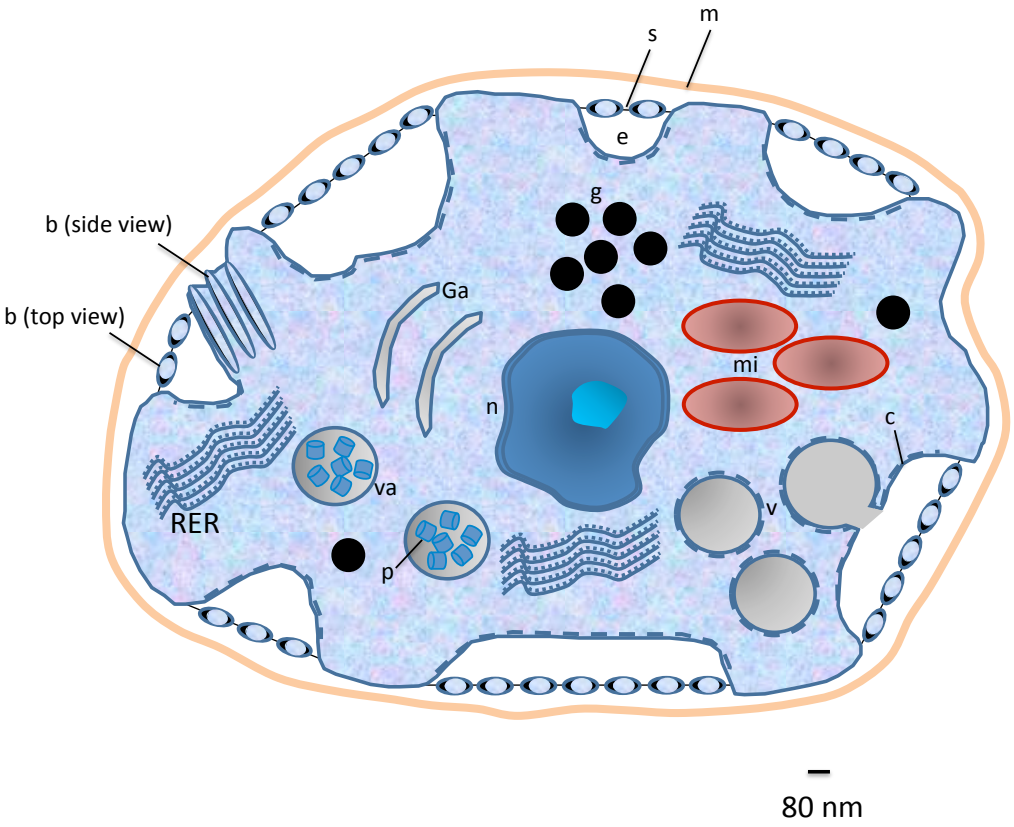

Figure 3.2. ***Typical molluscan rhogocyte.*** *Nucleus (n), mitochondria (mi), Golgi apparatus (Ga), rough endoplasmatic reticulum (RER), electron dense granula (g), vacuole (va), vesicle (v), protein molecule (p), extracellular lacunae (e), cytoplasmic bar (b), slit (s), coated plasma membrane (c), lamina of extracellular matrix (m). (Graphic: J. Markl)*

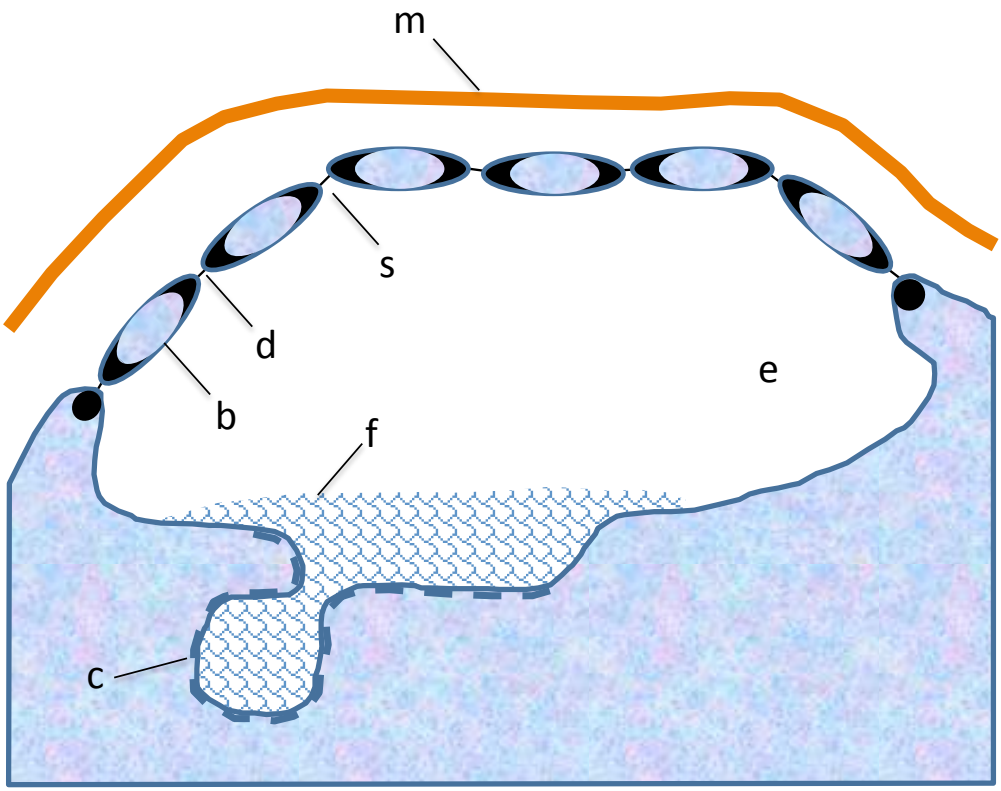

Figure 3.3. ***Drawing of the slit apparatus of a rhogocyte.*** *Extracellular lacuna (e), coated cell membrane (c), floccular material (f), cytoplasmic bar (b), slit (s), diaphragma (d), lamina of extracellular matrix (m). (Graphic: J.Markl)*

4. The hemoglobin of *Biomphalaria glabrata* (BgHb)

The planorbid snail *B. glabrata*, an intermediate host of the human parasite *Schistosoma mansoni* that causes bilharziosis, is a widely used model organism. It gives strong incentives to conduct research on various aspects of epidemiology (for studies on the ultrastructure and function of the different cell types of *B. glabrata*, see Kitajima & Paraense, 1983; Bielefeld et al., 1993; Gao & Wiederhold, 1997; Dos Santos Souza & Andrade, 2006; Cavalcanti et al., 2012). *B. glabrata* expresses only minute amounts of hemocyanin (Lieb et al., 2006); instead it uses a multimeric hemoglobin to bind, transfer and release oxygen molecules. The hemoglobin of *B. glabrata* has been studied structurally and functionally (Bugge & Weber, 1999; Lieb et al., 2006; Moeller et al., 2011). It evolved from pulmonate myoglobin, possibly to replace a less efficient hemocyanin (Arndt et al., 1998; Lieb et al., 2006). Due to its high oxygen affinity, this hemoglobin is the better oxygen transporter in hypoxic environments.

The hemoglobin multimer is a 1.44 MDa complex of six 240 kDa polypeptide subunits, arranged as three disulfide-bridged dimers (for reconstruction see Fig. 4.1). The *B. glabrata* hemoglobin is a glycoprotein with carbohydrates at approx. 3% carbohydrates (Afonso et al., 1976; Almeida & Neves, 1974). Lieb et al. (2006) sequenced two different isoforms, each containing 13 different, cysteine-free heme domains, plus a small N-terminal non-heme 'plug' domain with three cysteines for subunit dimerization.

Apart from hemoglobin and traces of hemocyanin, two acetylcholine-binding proteins (BgAChBP1 and BgAChBP2) exist in the hemolymph of this animal. BgAChBP1 is a regular pentagonal dodecahedron of 22 nm in diameter (Saur et al., 2012).

The data from a genome project on *B. glabrata* are available (Raghavan & Knight, 2006).

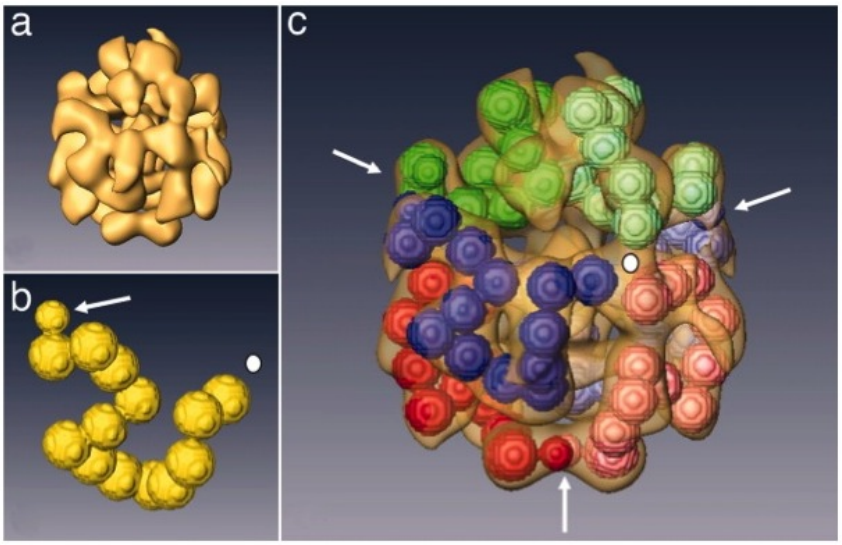

Figure 4.1. ***Three-dimensional reconstruction of the quaternary structure of BgHb.*** *(A) 3D reconstruction of native BgHb. (B) Model of the BgHb polypeptide subunit with 13 globular masses for the heme domains and N-terminally a smaller mass for the plug domain (arrow). (C) The same view as in (A), incorporating six polypeptide subunits as modeled in (B), distinguished by different colors. By bridging together the N-terminal plug domains (arrows) of pairs of polypeptide chain subunits, this model is consistent with the occurrence of disulfide-bridged dimers of polypeptide chains, as was demonstrated biochemically. Additionally, subunits form triplets by joining C-temrinal domains (white dot). (Taken from Lieb et al., 2006)*

5. The hemocyanin of *Lymnaea stagnalis* (LsH)

L. stagnalis is a large air-breathing freshwater snail that is worldwide distributed. It expresses hemocyanin as respiratory protein (Hall et al., 1975). Hemocyanin contains two copper ions in its active site. It is found freely circulating in the hemolymph of molluscs and arthropods (Miller & van Holde, 1982; Ellerton et al., 1983; van Holde, 1997), but molluscan hemocyanin is structurally very different from arthropod hemocyanin (Bonaventura & Bonaventura, 1980; Markl & Decker, 1992; Harris & Markl, 1999; van Holde et al., 2001).

In case of molluscan hemocyanins, the basic structure is a cylindrical decamer with an external diameter of 35 nm and a molecular mass of 3.5 MDa (cephalopods) or 4 MDa (other molluscs) (for reconstruction see Fig. 5.1). Therefore, hemocyanins are among the largest proteins in the nature. They are organized as decamers, didecamers or multidecamers of 350 kDa or 400 kDa polypeptide subunits containing seven or eight functional units (FUs, termed a-b-c-d-e-f-g-h) (Harris et al., 1997; Decker et al., 2007; Gatsogiannis et al., 2007; Gatsogiannis & Markl, 2009; Markl, 2013). FU-a to FU-g have a molecular mass of 45-50 kDa, whereas FU-h carries an additional C-terminal tail of 100 amino acids and has a molecular mass of 60 kDa. Within the gastropod taxon Cerithioidea, a special 'mega-hemocyanin' has been discovered that contains a 550 kDa subunit (Lieb et al., 2010).

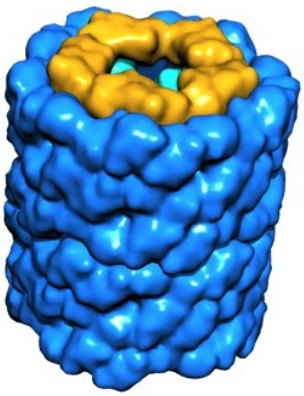

Figure 5.1. ***Low resolution model of a hemocyanin didecamer.*** *(Source: J. Markl)*

Each FU contains one oxygen-binding site consisting of two copper ions, each bound to three histidine residues. In gastropods, five pairs of the additional FU-h form an outer collar complex. The structure of gastropod hemocyanins has been studied in detail by DNA sequencing and 3D-electron microscopy (reviewed by Markl, 2013).

L. stagnalis hemocyanin is a didecamer like the one shown in Fig. 5.1; the complete amino acid sequence of two isoforms is also available.

6. Aim of this thesis

The rhogocytes of *B. glabrata* have been studied previously (Sminia et al., 1972), and TEM data on the rhogocytes of *L. stagnalis* are also available (e.g. Sminia & Boer, 1973). However, in both species, and generally in molluscan rhogocytes, many questions are still open. Approaching the project with EM techniques could reveal information about the existence of different types of rhogocytes. Aim of this work is to study the structure in more details than previously described, especially in the area of the slit apparatus. Focus should be given in the highly dense material that is observed in the cytoplasmic bars at the insertion side of the slits. In order to answer these questions and explain the release of proteins into the hemolymph, the slit apparatus will be studied by electron tomography and a 3D model will be calculated. These data will be supported by biochemical experiments so as to set light into the mechanism of the biosynthesis of hemoglobin and hemocyanin. Apart of the synthesis of the respiratory proteins, more data will be collected to answer the questions regarding the function of rhogocytes in other pathways, such as heavy metal detoxification, protein uptake and degradation. Furthermore, the hypothesis of a common phylogenetic basis with mammalian podocytes and insect nephrocytes will be tested and discussed. Last but not least, an approach to study the structure of rhogocytes under cryo-conditions will take place in order to keep the cells in close to native conditions.

Part II.

Material & Methods

7. Animals

7.1. *Biomphalaria glabrata*

Table 7.1. ***Taxonomic hierarchy of B. glabrata.***

Kingdom	Animalia
Phylum	Mollusca
Class	Gastropoda
Order	Basommatophora
Superfamiliy	Planorboidea
Family	Planorbidae
Subfamiliy	Planorbinae
Genus	*Biomphalaria*
Species	*B. glabrata*

B. glabrata is an air-breathing freshwater snail belonging to the family Planorbidae (see Fig. 7.1). It inhabits small streams, ponds and marshes and is able to survive for a long time if it is removed from this environment. This genus is extremely important, as an intermediate host of *Schistosoma mansoni* that infects about 83 million people. It lays egg masses at a rather high rate (1 per day). Within a lifespan of max. 15-18 months in natural conditions, it can reach a length up to 2 cm. Its hemolymph is red because of hemoglobin, which is an iron containing oxygen-transport metalloprotein in the red blood cells of all vertebrates.

Figure 7.1. ***The freshwater snail Biomphalaria glabrata.*** *(Source: C. Kühne)*

Hemoglobin consists of protein subunits, which are folded chains of large number of different amino acids. *B. glabrata* has a strong muscle which allows the snail to pull its body completely inside the external shell of calcium carbonate. *B. glabrata* was obtained from a freshwater tank culture (20 °C) established in our research group.

7.2. *Lymnaea stagnalis*

Table 7.2. ***Taxonomic hierarchy of L. stagnalis.***

Kingdom	Animalia
Phylum	Mollusca
Class	Gastropoda
Order	Basommatophora
Superfamiliy	Lymnaeoidea
Family	Lymnaeidae
Subfamiliy	Lymnaeinae
Genus	*Lymnaea*
Species	*L. stagnalis*

L. stagnalis is a widely distributed large air-breathing freshwater snail (see Fig. 7.2). The snail has a shell of 2-5 cm in length. *L. stagnalis* has a simple neuron system, organized in a ring of interconnected ganglia. It has a shiny, yellowish brown shell, delicate and transparent. The shell is hard, rigid and covering most of its body, which is yellowish grey in color, with a large head and long tentacles. A unique organ called radula is used for feeding. It is an odontophore, a lingual ribbon of tooth-like processes. It obtains food by rasping or licking action. There is a soft

Figure 7.2. ***The freshwater snail Lymnaea stagnalis.***

mantle that surrounds the body, lines the inner surface of the shell and secretes the material that will form this shell. The foot is used for contraction, expansion and locomotion. *L. stagnalis* shows selective feeding responses to different chemicals. In poor oxygen conditions, it moves to the surface of water to carry out aerobic breathing.

L. stagnalis was collected from a pond at the university campus and maintained in controlled freshwater tanks at 20 °C.

The animals were fed 3-4 times per week. Animal work on both snails has been conducted according to the national guidelines. In case of the experiments presented here, there was no need for approval of an ethics committee. All surgery was performed under 7 % magnesium chloride ($MgCl_2$)/ice anesthesia, and the animals were killed during anesthesia. Thus, all efforts were made to minimize suffering.

8. Biochemical Methods

8.1. Sample preparation for histological analysis

In order to study the structure of the snails, whole individuals were laid on the Histosette® (VWR, Darmstadt) and dehydrated in a series of increasing alcohol concentrations (60-100 %) followed by xylol. For the performance of cross sectioning, they were embedded in paraffin (Fig. 8.1). The 3-5 μm sections were prepared on a rotation microtome (Leica Microsystems GmbH, Wetzlar) and collected with glass object slides (AA00000102E, Menzel, Braunschweig).

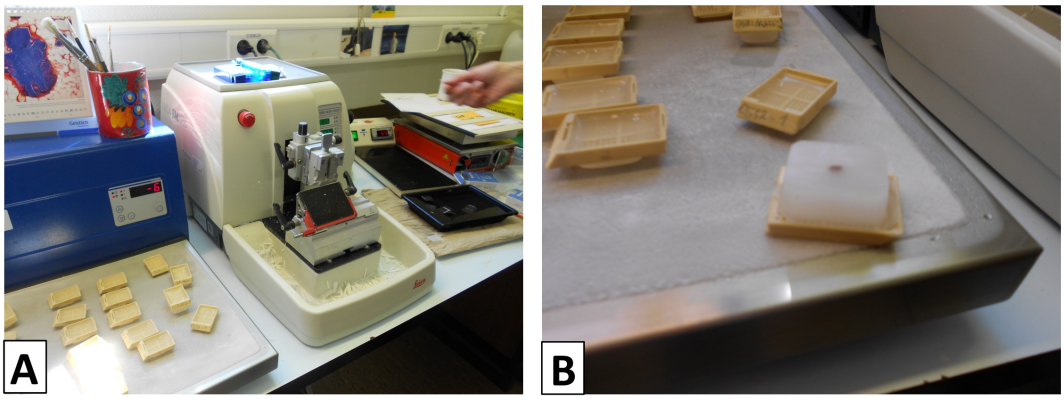

Figure 8.1. ***Histological analysis.*** *(A) Rotation microtome. (B) Paraffin embedded sample.*

8.2. Immunohistochemistry

Using the MaxLSABTM Rabbit HRP Detection Kit (Max Vision Biosciences, Washington, USA), immunohistochemistry on paraffin-embedded tissue sections was performed. The applied rabbit antibodies were specifically directed against *B. glabrata* hemoglobin and were diluted 1:100,000 with 50 mM Tris/HCl, pH 7.6. In case of *L. stagnalis*, anti-*Aplysia* hemocyanin antibodies diluted 1:20,000, 1:35,000 & 1:50,000 were applied on the sections. These polyclonal antibodies were ordered from Charles River (Sulzfeld). Biotinylated anti-rabbit secondary antibody included in the kit was used. The sections were incubated for 1 h at room temperature with the primary antibodies and rinsed with 50 mM Tris/HCl, pH 7.6. The color reaction was stopped after 10 min and the sections were air-dried, mounted

and observed under the fluorescence microscope Leitz DM/RBD equipped with the Camera Leica DC 500 (Leica Microsystems GmbH, Wetzlar).

The images were collected using the program Paint Shop Pro (PSP, Jasc Software, Eden Prairie, Minnesota, USA).

The chemicals were ordered from Carl Roth GmbH (Karlsruhe).

8.3. RNA extraction

The RNA was extracted from the animal tissue according to the total RNA isolation NucleoSpin RNA II Kit (Macherey-Nagel). In order to homogenize the sample, 30 mg of tissue was disrupted.

8.4. Primer design

The primers were designed by means of the program GENEIOUS (Drummond et al., 2011). When designing the primers, the following information were considered carefully:

- primers should be 17-28 bases in length
- base composition should be 50-60 % (G + C)
- annealing temperature of 55-80 °C are preferred
- no palindroms
- no self- complementarity

In the case of *B. glabrata*, the primer design was based on the sequence of the heme domains BgHb1-h and BgHb2-i of the *B. glabrata* hemoglobin (BgHb) isoform BgHb1 and BgHb2 (Moeller et al., 2011) (see Table 8.1).

In the case of *L. stagnalis*, specific primers were designed for the functional unit LsH-h of *L. stagnalis* hemocyanin (LsH), the sequence of which can be found in Table 8.2.

Table 8.1. ***Primers and cDNA sequence for B. glabrata.***

forward primer (isoform 1)	TCCGTAACCAGGTCAGGGCCA
reverse primer (isoform 1)	GCTGGTGGCAGACAAAACTTCGGT
cDNA (isoform 1)	TCCGTAACCAGGTCAGGGCCATCAC CCGTGGTATCGAGTCATTTGTGAAC AGTCAACAACCCCGCTGCTCTCCAG TCCAGCATTGAGAATCTGGTCGATG CTCATTTGAACTTCCAACCCAGCAT TGGTCTTTCCTACTTTGGATCCGTC CAACAATACATCCATCTCTACATCG CAAGCTCTCGGTGTTGCTTCTAACA GTGATGAGGCCAAATCATGGACTAA CTTGTTCGCTGCCTTCAACAAAGTC TTGAAAGAGCATTCCCTCGAGAAAA TCGGTATTTCAGATAGCGATAAAAG AGCACTTGTCAGCTCCTGGAAGAAA CTAACTGCTGGTGGCAGACAAAACT TCGGT
forward primer (isoform 2)	GGTGTGGCTGCCAACAGTGA
reverse primer (isoform 2)	TGGGCTCCTTGGTGGACGTTG
cDNA (isoform 2)	GGTGTGGCTGCCAACAGTGATGAAG CTACATCCTGGACTAACCTTTGGGC TGCTTTCAATAAAGTTCTCAAAGAG CATTCTCTAGAAAAACTTGGAATCA CTGACAATGAAAGAAAAATTCTGGT TAGTTCTTGGAAAAGATTGACAACT GAAGCCAATGGTCAGCAAAGTCTCG GAGTCAAACTAGTTCTCTGGATGTT GGACAGTGCCCAATATGCGTGACCA ATTCACAAAGTTCAATGCACGCCAA TCCAATGATGATTTGAAGAGAGATG CTGGCTTTCTGAAACAAGTTAAGAA AATTATTGGAGGCTTGGGCTCCTTG GTGGACGTTG

8.5. mRNA isolation

The RNA that was extracted during the previous step (Section 8.3) was used as a template to create cDNA ('complementary' DNA), which in comparison with genomic DNA has no introns. For this method, the Super Script III First-Strand Synthesis System for RT-PCR (Invitrogen, Darmstadt) was used. The synthesis of cDNA took place (according to the protocol included in the kit) at 50 °C for 50 min and the reaction was terminated at 85 °C for 5 min. 5 μl was removed from this

Table 8.2. ***Primers and cDNA sequence for L. stagnalis.***

forward primer	CCGAGGCTATCCGCAAGGGC
reverse primer	GGTGTGCACGACACCGAGGG
cDNA	GAGGCTATCCGCAAGGGCAAAATCT CTACTGACCATGCCGTTAAGGCAAG ATTCACCTCCACTGATTACCAGGGT AATTTAAACCACCAAGACACCGATT ATGCCATCATTGTTGAGAGGCATGC TGAGCAGGACTACGATGTTGTCGAG ATTCCAGTCGGCAGAAAGTATCCTT TACCACCTAAGATTGTCTTGAAGAA GGGATCCCGTGTCAAGTTTTACCCT GGCAGCGACACCTTCAACTCACCCC TCGAGAACCTCGGCAGCTACACTTC TTTCAGCAAGTGCTCCATCCCACCG TTCTCCTACCAGAGCTACGCCCTCG GTGTCGTGCACACC

reaction and used further as a template for the following polymerase chain reaction (PCR) (see Tables 8.3 & 8.4):

Table 8.3. ***Components of PCR for the cDNA synthesis.***

RT product	5 μl
2 $\times$ PCR Mix	10 μl
forward primer (10 pmol/μl)	1 μl
reverse primer (10 pmol/μl)	1 μl
H_2O	3 μl

Table 8.4. ***PCR Program for the cDNA synthesis.***

denaturation	92 °C, 2 min
denaturation annealing elongation	94 °C, 20 s 55 °C, 30 s 72 °C, 30 s $\times$ 30
final elongation	72 °C, 10 min
cooling	4 °C

In order to amplify a piece of DNA we performed PCR in the PCR machine. This method relies on thermal cycling, consisting of cycles of repeated heating and cooling of the reaction for DNA melting and enzymatic replication of the DNA. We used a *Taq* polymerase (Invitrogen, Darmstadt) isolated from *Thermus aquaticus* (Sambrook & Russell, 2001).

8.6. Determination of hemocyanin consentration

The protein concentration of the samples was estimated in the nanodrop 1000 (Thermo Fisher scientific, Wilmington, USA). 1.5 μl of the probe was applied and the wavelength was detected at 260 nm to test the absorption of nucleic acids. There were some extra measurements done at 280 nm and 230 nm. A260/A280 provides information on the quality of the probe. For uncontaminated DNA and RNA the right value is 1.8 and 2.0 respectively. Furthermore the value of A260/A230 (uncontaminated probe is 2.0) will give information regarding the contamination with polysaccharides, peptides und phenols.

8.7. DNA gel electrophoresis

The size of the PCR products was checked through a DNA gel electrophoresis. The technique is simple, rapid to perform and capable of resolving fragments of DNA variying from 50 bp to several megabases in length (Sambrook & Russell, 2001). Large molecules migrate more slowly because of greater frictional drag and because they find their way through the pores of the gel less efficiently than small molecules. In our case this was performed in a 1.5 % Tris-borate (TBE) agarose gel (1.5 % agarose in 1x TBE), run at 120 V for 45 min. 6x loading dye (Fermentas, St. Leon-Rot) was used to dye the DNA, and the size was estimated with the help of GeneRuler^{TM} DNA Ladder Mix (Fermentas, St. Leon-Rot) (see Fig. 8.2). The presence of ethidium bromide allows the gel to be examined by UV illumination at any stage during electrophoresis. Ethidium bromide contains a tricyclic planar group that intercalates between the stacked bases of DNA. It binds to DNA with no sequence reference. As a stock, the 10x TBE buffer was prepared in advance as follows: 0.9 M Tris/HCl, 0.9 M boric acid, 20 mM EDTA; fill up to 1 l with distilled H_2O.

8.8. Gel extraction

In order to extract the DNA fragments from the gel, the GeneJET^{TM} Gel Extraction Kit (Fermentas, St. Leon-Roth) was utilized. The bands with the size of interest were extracted with a small knife from the gel with the help of UV-light. The following steps were done according to the protocol of the kit. The final product was sent for sequencing (6 μl DNA product + 1 μl primer) at the StarSEQ® GmbH (Mainz).

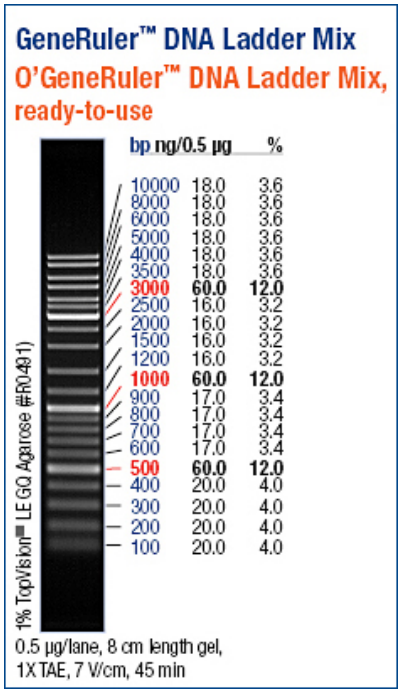

Figure 8.2. ***GeneRuler^{TM} DNA Ladder Mix.*** *(Fermentas, St. Leon-Roth). Source: http://www.thermoscientificbio.com/nucleic-acid-electrophoresis/generuler-1-kb-dna-ladder-ready-to-use-250-to-10000-bp*

8.9. Cloning of PCR products

The DNA product from the gel extraction was inserted in a vector and then transformed in bacterial cells. For this work the StrataClone^{TM} PCR Cloning Kit (Agilent, Böblingen) which combines the efficient DNA rejoining activity of DNA topoisomerase I and the DNA recombination activity of Cre recombinase, was used. The procedure was followed according to the protocol provided with the kit (for overview of the cloning and information about the vector see Fig. 8.3 & Fig. 8.4). The bacterial cells were incubated on ice for 20 min and after a heat shock for 45 s at 42 °C, they were further incubated on ice for 2 min. After the transformation the bacterial cells were mixed with 250 μl of LB medium and let to shake for 1 h at 37 °C. Afterwards, the cells were given to agar plates with resistance to ampicillin and incubated at 37 °C overnight (for solutions, see Table 8.5).

8.10. Selection of white colonies

The agar plates have resistance to ampicillin, preventing bacterial cells other than those where the transformation of the plasmid was successful from growing. The

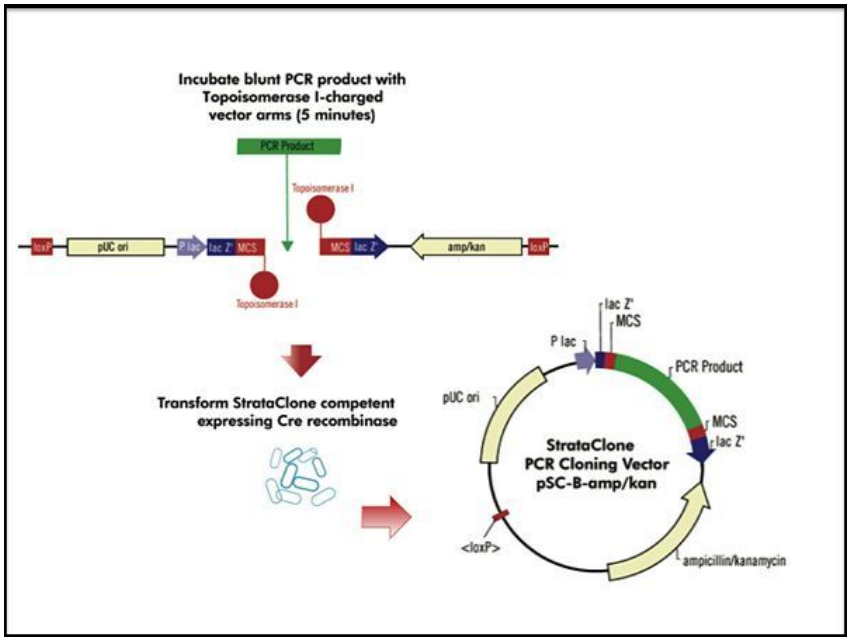

Figure 8.3. ***Overview of the StrataClone^{TM} PCR cloning method.*** *(Agilent, Böblingen)*

Table 8.5. ***Solutions for the cloning.***

LB medium	5 g yeast extract, 10 g Trypton, 10 g NaCl, pH 7.0
LB agar	20 g agar-agar in 1 l LB medium
Ampicillin-X-Gal-Agar	1 l LB agar, 0.5 mM IPTG, 80 μl/ml X-Gal, 100 mg ampicillin

white colonies are therefore selected, picked up using a pipette and added in a tube with 3 ml LB medium with ampicillin (100 μl/ml). This culture was let to shake overnight at 37°C.

8.11. Preparation of plasmid DNA and sequencing

The GeneJet^{TM} Plasmid Miniprep Kit (Fermentas, St. Leon-Roth) was used to isolate the plasmid DNA. In order to get rid of the recombinant vectors, the bacterial cells were centrifuged for 2 min and the supernatant was discarded. The pellet with the bacteria was re-suspended and the next steps were followed according to the protocol provided with the kit. The DNA was bound to the membrane of the columns and was eluted with the elution buffer. The products were stored at -20 °C. Furthermore, the product was sent for sequencing to make sure that it includes the

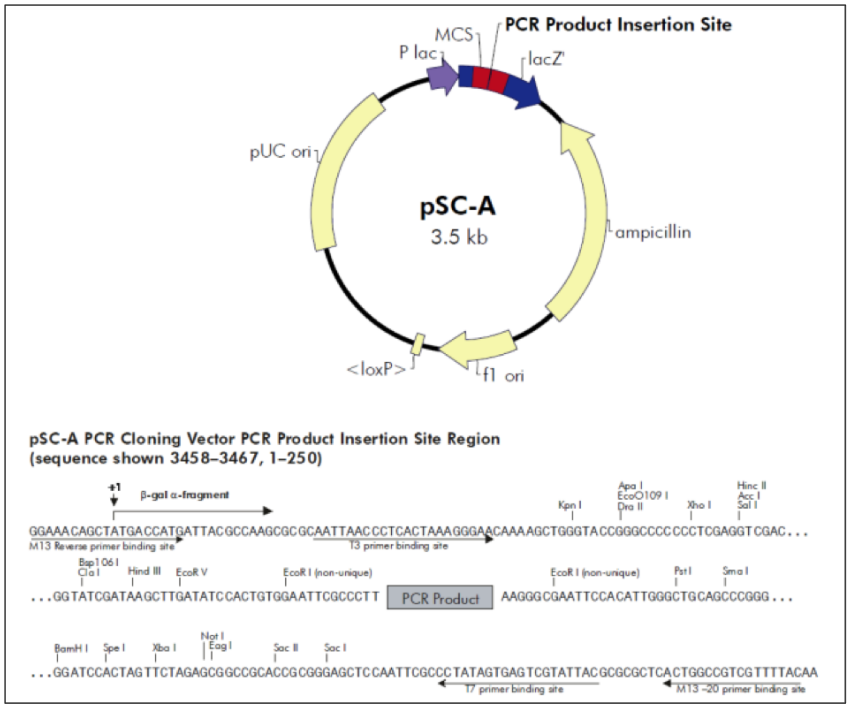

Figure 8.4. ***StrataClone^{TM} PCR Cloning vector pSC-A-amp/kan.*** *(Agilent, Böblingen)*

sequence of the right domain of the hemocyanin. The result (in FASTA-format) was observed in the program 'FINCH TV 1.4.0' (Geospiza, Inc., Seattle, WA). The quality of the data and the removal of the vector were checked. The cDNA sequence was translated into amino acids and aligned with the databank 'NCBI' (National Center of Biotechnology Information).

8.12. PCR to control the size of plasmid DNA

In order to control the size of the products, the following PCR reaction took place (see Tables 8.6 & 8.7). The products were controlled in an agarose gel as described above (Section 8.7).

8.13. Digoxigenin (DIG) labeling

DIG-dNTPs (Roche, Mannheim) were used so that the amplicons could act as a DNA probe in the PCR digoxigenin-labeled deoxynucleoside triphosphates (see Tables 8.8 & 8.9). Specific alkaline phosphatase (AP) coupled anti-digoxigenin

Table 8.6. ***Components of the PCR reaction to control the size of plasmid DNA.***

Dream Taq^{TM} Green PCR Master Mix	5 µl
forward primer	1 µl
reverse primer	1 µl
plasmid DNA	0.5 µl
H_2O	2.5 µl

Table 8.7. ***PCR Program for controlling the size of plasmid DNA.***

denaturation	95 °C, 2 min
denaturation annealing elongation	95 °C, 10 s 50 °C, 30 s 72 °C, 30 s × 30
final elongation	72 °C, 10 min

(anti-DIG) antibody bound to this probe. The AP catalyzed the addition of 5-bromo-4-chloro-3-indoxyl phosphate (BCIP) and nitro blue tetrazolium chloride (NBT), a reaction that formed a blue formazan. This was important for later on, so that the DNA probe could be detected in the tissue.

Table 8.8. ***Components of DIG labeling PCR.***

10 × PCR buffer – $MgCl_2$ (Invitrogen)	5 µl
50 mM $MgCl_2$ (Invitrogen)	1.5 µl
PCR DIG-labeling Mix (Roche)	1 µl
primer forward (10 pM/µl)	1 µl
primer reverse (10 pM/µl)	1 µl
Taq DNA polymerase recombinant (Invitrogen)	0.5 µl
DNA (10 pM/µl)	1 µl
H_2O	39 µl

8.14. PCR purification

To purify the PCR-products and isolate the DNA fragments of interest, the PCR/DNA Clean-Up Purification Kit (EURx Ltd., Gdansk, Polen) was utilized by using the bands of the gel electrophoresis. This removed contaminants such as ethidium bromide, primers, *Taq* DNA polymerase and other proteins/lipids effectively.

Table 8.9. ***PCR Program for DIG labeling.***

denaturation	94 °C, 3 min
denaturation annealing elongation	94 °C, 45 s 55 °C, 30 s 72 °C, 1 min × 35
final elongation	72 °C, 10 min
cooling	4 °C

8.15. Southern blot

The specificity of each probe can be detected by means of the Southern blot test (for solutions see Table 8.10). The gene to be detected and a negative control were applied to a nylon membrane and hybridized with the probe. The test is positive and the probe specific, if only the DNA of the gene to be detected is colored. To avoid any cross reaction, the DNA of both isoforms together with a negative probe were applied together on a nylon membrane. In addition, different dilutions were tested in order to avoid wrong results because of high DNA concentration. For the Southern blot, the following dilutions were tested: 1:10, 1:20, 1:50, 1:100.

1 μl of each of these dilutions was dropped and air-dried on a nylon membrane. The Whatman paper was soaked in denaturation buffer and then the nylon membrane was placed on it for 5 min, so that it could fully absorb. The nylon membrane was dried on a Whatman paper for 5 min. These steps were repeated with neutralization and equilibration buffer. The nylon membrane was subsequently dried in a drying cabinet at 80 °C for 30 min to fix the DNA in the membrane. Specific binding sites were blocked by double treatment with equilibration buffer for 5 min each, followed by pre-hybridization at 68 °C in a shaking water bath with the hybridization buffer for 1 h. 20 μl of each probe was denatured (PCR, 10 min at 95 °C), and added to the hybridization buffer in a shaking water bath. The hybridization took place overnight at 68 °C. The buffer was then removed and the nylon membrane was washed in 2x SSC / 0.1 % SDS twice for 5 min at room temperature and then 2x 15 min in 0.5x SSC / 0.1 % SDS at 68 °C. Afterwards, the nylon membrane was equilibrated in a wash buffer on a shaker and treated for 30 min in blocking solution. Incubation with anti-DIG-AP fab fragment (Roche, Mannheim) was performed in a 1:7,500 fold dilution in blocking solution on a shaker for 60 min at room temperature. The nylon membrane was washed in washing buffer 3x 5 min and then equilibrated for 10 min in AP-buffer. At the end, the nylon membrane was incubated with the color solution for 15 min.

The dot blot, which was performed afterwards, gave an indication of the amount of sample to be used for the *in situ* hybridization (for solutions see Table 8.11). The probes were applied and air-dried on the nylon membrane. Afterwards, the nylon

Table 8.10. ***Solutions for the southern blot.***

denaturation buffer	0.5 M NaOH 1.5 M NaCl	wash buffer (pH 7.5)	0.15 M NaCl 0.1 M Tris/HCl
neutralization buffer (pH 8)	0.5 M Tris/HCl 1.5 M NaCl	blocking solution	wash buffer 1 % blocking reagent
equilibrium buffer (pH 7)	0.3 M NaCl 0.03 M NaCitrate	AP buffer (pH 9.5)	0.1 M Tris 0.1 M NaCl 0.005 M $MgCl_2$
hybridization buffer	5 × SSC with: 0.02 % SDS 1 % blocking reagent 0.1 % N-Lauryl-sarosin	substrate NBT	50 mg/ml NBT in 70 % Dimethylformamide
20 × SSC	3 M NaCl 0.3 M NaCitrate pH 7.0	substrate BCIP	50 mg/ml BCIP in 100 % Dimethyl-formamide
2× SSC / 0.1 % SDS	3 M NaCl 0.03 M NaCitrate 0.1 % SDS	color solution	6.6 μl NBT 3.3 μl BCIP 1 ml AP Buffer

membrane was placed in MAB buffer and blocked for 30 min in blocking solution on a shaker. The antibody incubation was carried out in a dilution of 1:7,500 in AP buffer on a shaker in the dark (for 30 min). The membrane was then washed 2x 15 min with washing buffer and incubated for 2 min in AP buffer. The color reaction took place and stopped with H_2O (Fig. 8.5 A & B). For the dot blot the following dilutions were tested: 1:2, 1:8, 1:16, 1:32, 1:64.

Table 8.11. ***Solutions for the dot blot.***

MAB buffer (pH 7.5)	0.1 M maleic acid 0.15 M NaCl 0.1 % Tween 20	wash buffer (pH 7.5)	0.15 M NaCl 0.1 M Tris/HCl
blocking solution	MAB buffer 2 % blocking reagent	AP buffer (pH 9.5)	0.1 M Tris/HCl 0.1 M NaCl

8.16. Whole mount *in situ* hybridization

The chemicals for the *in situ* experiements were ordered from the following companies: Carl Roth GmbH (Karlsruhe), Eppendorf AG (Hamburg), Gilson Inc. (Middleton, USA), Starlab GmbH (Ahrensburg), Biozym Scientifc GmbH (Hessisch-Oldendorf), Fluka Chemical GmbH (Buchs), Whatman GmbH (Dissel), Invitrogen (Darmstadt), Roche (Mannheim), Sigma-Aldrich (Deisenhofen) and Merck (Darmstadt). For solutions see Table 8.12.

The primers were designed and generated by a commercial service (Sigma-Aldrich, Hamburg).

DNA probes of *B. glabrata* were kindly provided by Dr. Vanessa Moeller.

The equipment that was used during *in situ* hybridization:

- thermocycler T Gradient 96 and T Personal Combi (Biometra GmbH, Göttingen)
- centrifuge Micro liter desk centrifuge 5417 R (Eppendorf AG, Hamburg)
- gel chambers (Biotec Fischer, Reichskirchen)
- gel documendation 8UV-transilluminator TFX-20 M (Viber Lorumat GmbH, Eberhart-Zell) and Sony XC-75E S7W camera (Sony, Berlin)
- nanodrop 1000 (Thermo Fisher scientific; Wilmington, USA)
- photometer Ultraspec 3100 Pro (Amersham Bioscience, Switzerland)
- epifluorescence microscope Leitz DM/RBD, equipped with the Camera Leica DC 500 (Leica Microsystems GmbH, Wetzlar)
- petri dishes, falcon tubes and well plates (Greiner Bio-One GmbH, Frickenhausen)
- PCR reaction tubes (Thermo Fisher Scientific, Schwerte)
- wheighing machine (Mettler-Toledo GmbH, Giessen)
- hotplates and water baths (Jolabo, Seelbach & Techne, Staffordshire, UK)
- digital pH meter 646 (Knick, Berlin), incubator (Memmert, Schwabach)

In the case of *B. glabrata*, the animals were anesthetized with 7 % $MgCl_2$ by cooling on ice for 15 min. They were fixed and their shells were removed. The hybridization was carried out as follows by means of the protocol published by Streit et al. (2005). The individuals were treated with a freshly prepared solution of 0.5 % KOH / 3 % H_2O_2 for 30 min in order to remove the pigments (Fig. 8.5 C). The animals were washed with ascending concentrations of methanol/PBS. Methanol was exchanged

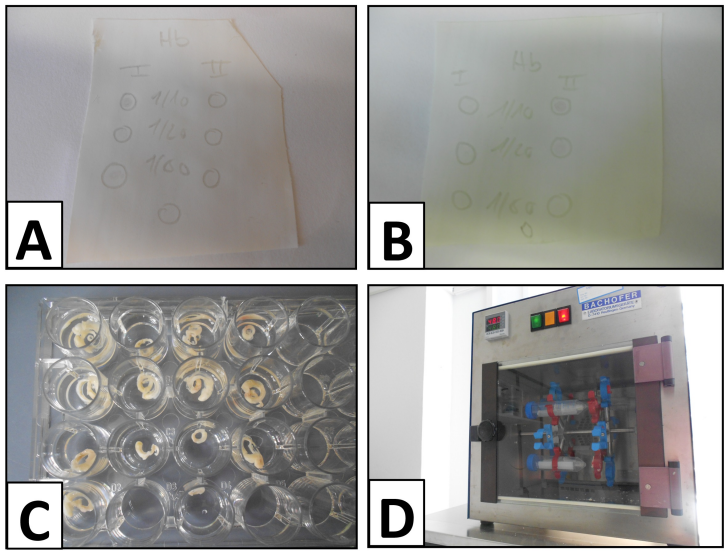

Figure 8.5. ***In situ hybridization experiment.*** *(A, B) Dot blot for BgHb. (C) Well plate with B. glabrata individuals treated with 3 % H_2O_2 in 0.5 % KOH. (D) Hybridization inside the incubator.*

with PBT and finally with PPE. After being washed for 5 min with ice cold PBT, they were treated with proteinase K (20 μg/ml in PBT) at 37 °C, in order to facilitate the penetration of the tissue from the probe and the antibody. Following washing steps with ice cold PBT to stop the action of proteinase K, the animals were incubated with 4 % paraformaldehyde in PBS. This solution was washed away with PBT. To avoid unspecific binding of DNA, pre-hybridization took place using the hybridization medium for 3 h in a water bath at 42 °C. The probes were denatured at 65 °C for 10 min. The denatured probe (10-40 μg/ml hybridization medium) was added to the animals and the hybridization was carried out overnight in the same temperature (Fig. 8.5 D). The next morning the samples were washed with 4x, 2x and 1x washing buffers at 50 °C to remove the hybridization medium. Afterwards, 1x SSC/0.1 % Tween was added and then exchanged with MAB solution for 10 min and with block solution for 2 h. The incubation with anti-DIG-AP antibody that followed took place overnight at 4 °C (the antibody was diluted 1:2,000 and the final concentration was 0.5 μl/ml block solution). The antibody was washed away with MAB/0.1 % Tween for 5x 15 min and with AP buffer/0.05M $MgCl_2$ for 2x 15 min. The color reaction that followed lasted approximately 10 min and was stopped by washing the animals with MAB and PBT. Finally, the animals were post-fixed in 4 % paraformaldehyde in PBS overnight at 4 °C. The next day, the animals were washed with PBS and stored at 4 °C in 70 % ethanol. The same protocol was used in the case of *L. stagnalis* but with the following alterations: After removing the pigments, the animals were washed with 1xPBS and ascending concentrations of ethanol, and were stored at 4 °C overnight. The next day, ethanol was exchanged

Table 8.12. ***Solutions for the in situ hybridization.***

hybridization buffer	50 % formamide, 5 mM EDTA 1 × Denhardt's solution, 100 µg/ml heparin 100 µg/ml herring sperm DNA 0.1 % Tween20 in 5 × SSC
20 × SSC stock solution	3 M NaCl, 0.3 M sodium citrate, pH 7.0
fixation medium	2 ml 5 × Salt, 5 ml 8 % parafolmadehyde 3 ml H_2O
5 × salt	0.5 M MOPS, 10 mM $MgSO_4$ 5 mM EGTA, 2.5 M NaCl, pH 7.5
1 × PBS	140 mM NaCl, 2.7 mM KCl 8.1 mM $Na_2HPO_42H_2O$ 1.5 mM KH_2PO_4, pH 7.4
PBT	1 × PBS, 0.1 % Tween20
PPE	1 × PBS, 4 % paraformaldehyde 0.05 M EGTA
4 × washing buffer	4 × SSC, 50 % formamide, 0.1 % Tween20
MAB buffer	0.1 M Malein acid, 0.15 M NaCl 0.1 % Tween20
block solution	2 % block reagent in maleic acid
color reaction	5 µl NBT, 3.75 µl BCIP/ml AP buffer
NBT	50 mg/ml Nitro blue tetrazolium chloride in 70 % dimethylformamide
BCIP	50 mg/ml 5-bromo-4-chloro-3-indolylphosphate in 100 % dimethylformamide

with PBT and finally with PPE. After the washing steps with ice cold PBT to stop the reaction of proteinase K, the animals were incubated directly with PPE and finally with PBT. The samples were incubated for 3 h in blocking solution, before the incubation with the antibody.

8.17. *In situ* hybridization on paraffin sections

According to Albrecht et al. (2001) *in situ* hybridization on paraffin sections was carried out as follows (Fig. 8.6): The sections were treated with xylol for 3x 10 min and after being washed with ethanol, were incubated for 30 min at 37 °C with 5 µg/ml proteinase K in 50 mM Tris, pH 7.5. This reaction was stopped by washing with 0.2 % glycine in PBS.

The sections were then washed with PBS and post-fixed with 4 % paraformaldehyde

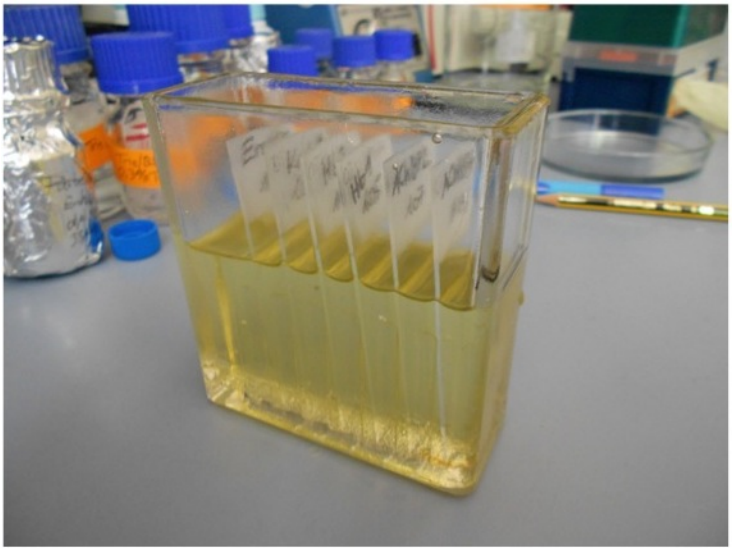

Figure 8.6. ***In situ hybridization on paraffin sections.***

in PBS for 5 min. After being acetylated with 0.1 M triethanolamine and 0.25 % acetic anhydride in 2x SSC and washed with distilled water, the sections were air-dried and the hybridization took place overnight at room temperature (10 ng/μl DNA probe in hybridization solution). The next day the sections were washed with 2x SSC and treated for 10 min with Tris/BSA. As a next step, the sections were incubated with 0.3 % TritonX-100 in Tris/BSA and then with anti-DIG-AP fab fragment at room temperature for 1 h (diluted 1:5,000 in Tris/BSA). Then, they were washed with Tris/BSA and incubated further with the development medium. After adding NBT and BCIP at room temperature, the color reaction was successful and the sections were washed with a solution of 10 mM Tris/HCl and 1 mM EDTA pH 8.1 and distilled water. The sections were air-dried. (for solutions see Table 8.13).

Table 8.13. ***Solutions for the in situ hybridization on paraffin sections.***

hybridization buffer	5 × SSC, 0.1 % SDS
Tris/BSA	100 mM Tris/HCl, 150 mM NaCl and 0.1 % BSA in pH 7.5
development / growth medium	50 mM Tris/HCl, 100 mM NaCl and 50 mM $MgCl_2$ pH 9.5
color reaction	6.6 μl NBT and 3.3 μl BCIP/ml development medium

9. Imaging techniques

9.1. Light microscopy

The slices were stained with hematoxylin and eosin stain (H&E) (according to protocols of the Handbook for Staining of the Institute for Pathology at the University Clinic, Mainz published by Ghanaati et al., 2010, 2011) and screened using light microscope. This is the most commonly used staining method in histology. It had the advantage that it was easy and fast, and could be used with every embedding medium. The staining involved the application of hemalum that led to a blue coloring of the cell nuclei. This was followed by counterstaining with eosin Y, which led to red, pink and orange coloring of other structures. Most of the cytoplasm was eosinophilic.

When an area of great interest was observed, two more sections were collected and were stained by Movat Pentachrome (MP) and Azan, according to protocols published by Ghannati et al. (2010, 2011). In the MP stain, nuclei of cells were blue-black, cytoplasm, elastic fibers and muscle cells were red, collagen and cartilaginous tissue yellow. Azan stain differentiated basophilic and chromophobe cells. It consisted of azo carmine that stained nuclei, erythrocytes, fibrin, acidophilic cytoplasm red and aniline blue that stained collagen fibers, basophilic cytoplasm and mucus blue.

The third and fourth consecutive slides at such a site remained unstained, to be further used for *in situ* hybridization experiments and immunohistochemistry. Following histological analysis led to total scan generation, which is a single large image of the whole histological specimen, assembled from 100-120 individual images in a 100x magnification and a resolution of 2500x1200 pixels.

The chemicals were ordered from Carl Roth GmbH (Karlsruhe).

The equipment necessary for these experiments was the following:

- Nikon Eclipse 80i histological microscope (Nikon, Tokyo, Japan)
- Nikon DS-Fi1 digital camera equipped with a digital sight control unit (Nikon, Tokyo, Japan)
- automatic scanning table (Prior scientific, Rockland, USA)

The software NIS-Elements 4.0 (Nikon, Tokyo, Japan) was needed for the collection of data during the immunohistology.

9.2. Immunofluorescence microscopy

Small pieces of mantle and foot of both *B. glabrata* and *L. stagnalis* were freshly collected and immediately frozen in isopentane (C_5H_{12}) that, in order to prevent water crystallization, was precooled in liquid nitrogen. They were kept at -80 °C. They were further embedded in the 'cryo embedding compound' (Microm, Walldorf). Cryo-sections of 5-7 μm were prepared at -25 °C, using the cryotome HM 500 OM (Microm, Walldorf). After that, the sections were further fixed with aceton for 20 min (-20 °C) and were encircled with the PAP PEN pencil (Micro-Bio-Tec, Giessen). The sections were incubated with 30 μl of the polyclonal guinea pig anti-nephrin antibodies NPHN/NPHS1 from Acris Antibodies GmbH (Herfold) (diluted 1:50 with PBS) and the monoclonal mouse anti-actin antibody 'clone C4' from Seven Hills Bioreagents (Cincinnati, USA) (diluted 1:100 with PBS) for 1 h in room temperature according to the method described by Schaffeld & Markl (2004). This antibody was initially characterized and successfully used in immune-electron microscopy by Lessard (1988); according to the data sheet it is directed against actin throughout the animal kingdom. In the case of *L. stagnalis*, the monoclonal mouse anti-actin antibody 05 from Thermo Scientific (Schwerte) was used. The sections were washed 3x 5 min with PBS and incubated with 30 μl of the secondary antibodies (diluted 1:200 in PBS) Texas Red-coupled goat-anti-guinea-pig and Cy2-coupled goat-anti-mouse (Dianova, Hamburg), respectively. They were further washed 3x 5 min with PBS and dehydrated for 5 min with ethanol. They were let to air-dry, embedded in Mowiol (Höchst AG, Frankfurt) based embedding medium and covered with a 24x60mm cover glass.

Mowiol-embedding medium:

- 6 g glycerol
- 2.4 g Mowiol
- 6 ml H_2O (stir for 2 h)
- 12 ml 0.2 M Tris/HCl pH 8.5 (stir overnight at 53 °C)
- 0.1 % DABCO, DAPI 1:1,000 (centrifuged at 5,000 rpm for 20 min at 20 °C before use) (centrifuge Megafuge 1.0R from Thermo Scientific, Schwerte)

Images were collected on a Leitz DM/RBD fluorescence microscope equipped with the Camera Leica DC 500 (Leica Microsystems GmbH, Wetzlar) in either phase contrast or epifluorescence optics with addition of oil. The images were collected using the program Paint Shop Pro (PSP, Jasc Software, Eden Prairie, Minnesota, USA).

The chemicals were ordered from Carl Roth GmbH (Karlsruhe).

9.3. Transmission electron microscopy (TEM)

The solutions needed for sample preparation and data collection were the following:

- glutaraldehyde, propylene oxide (Sigma-Aldrich, Munich)
- xylol (Carl Roth GmbH, Karlsruhe)
- phosphate buffer, lead citrate, paraformaldehyde (Merck, Darmstadt)
- araldite (Serva GmbH, Duisburg)
- grids, formvar, LR-white, gelatin capsels (Plano GmbH, Wetzlar; Agar Scientific, Essex, UK; Aurion, Wageningen, The Netherlands)
- monoclonal mouse anti-actin antibody 'clone C4' for *B. glabrata* experiments (Seven Hills Bioreagents, Cincinnati, USA)
- monoclonal mouse anti-actin antibody 05 for *L. stagnalis* experiments (Thermo Scientific, Schwerte)
- polyclonal pig anti-nephrin antibody NPHN/NPHS1 (Acris Antibodies GmbH, Herfold)
- polyclonal rabbit anti-*Aplysia* hemocyanin antibody (Charles River, Sulzfeld)
- hexadecane (Alfa Aesar), Dextran (Sigma), EPON (Fluca)

The following equipment and instruments were used:

- knife maker (LKB)
- light microscope Leica DM LS (Leica Microsystems, Wetzlar)
- diamond knife (Diatome, Weinheim)
- ultramicrotome Reichert Ultracut E (Leica Microsystems GmbH, Wetzlar)
- TemCam-F416 4K 4K CCD camera (TVIPS, Gauting)
- FEI (Eindhoven, Netherlands) Tecnai12 and F20 Transmission Electron Microscope

And finally the following softwares were used:

- EM-MENU 4 software package (TVIPS, Gauting)
- IMAGIC-4D software package (Van Heel et al., 1996)
- IMOD software package (Kremer et al., 1995)

- AMIRA (FEI Visualization Sciences Group, Bordeaux, France & The Zuse Institute Berlin, Germany; Stalling et al., 2005)
- EMAN2 software package (Tang et al., 2007)

9.3.1. Chemical fixation

Chemical fixation is the most widely used method for preserving biological specimen for light and electron microscopy (Hayat, 2000) due to the adequate preservation of many cellular components, the clarity of structural details and the ease of application to organisms. The goal of this method is to preserve the structure of cells with minimum alteration from the living state with regard to volume, morphology, spatial relationships of organelles, loss of tissue constituents and protection of sample against treatments including rinsing, dehydration, staining, vacuum and exposure to electron beam. Before embedding in resin, which is water-insoluble, free water must be exchanged with a solvent during dehydration. The fixative that will be used should provide more stable bonds that will hold the molecules together. This is accomplished by the formation of intermolecular and intramolecular crosslinks of proteins. Among various protocols, a double fixation with glutaraldehyde and osmium tetroxide (OsO_4) is the most effective in reducing the loss of cell constituents (Hayat, 2000).

1-3 mm^3 tissue pieces extracted from mantle and foot (Fig. 9.1 A, B, C) were fixed for a minimum of 2 h at room temperature in a freshly prepared medium of 1 % glutaraldehyde (a five-carbon aliphatic dialdehyde of a relatively simple structure, which has low viscosity and is soluble in water and organic solvents) in 0.02 M phosphate buffer of pH 7.2. Phosphate buffers are more physiological than any other buffer (Hayat, 2000), because they are found in living systems in the form of inorganic phosphates and phosphate esters. This buffer also stabilizes the pH of the fixative. After being rinsed in 0.1 M phosphate buffer of pH 7.2, the material was post-fixed for 1 h in 2 % OsO_4 (acting not only as fixative but also as a stain) in 0.05 M phosphate buffer of pH 7.2. Following washing steps in 0.1 M phosphate buffer and dehydration in ascending concentrations of ethanol, the samples were upgraded in propylene-oxide and embedded in araldite (Fig. 9.1 D & E), a glycerol-based aromatic epoxy resin that is water-immiscible (Hayat, 2000). This complete and uniform penetration of tissue specimens by the embedding medium is a prerequisite for satisfactory sectioning. The embedding medium not only impregnates and supports the tissue internally but also attaches the tissue to a block sufficiently strong to be handled safely during sectioning (Hayat, 2000). Semithin sections were cut with a glass knife and dried on a hot plate (70 °C). They were dyed with methylblue (1-2 min) and observed at the light microscope. Ultrathin sections (70-100 nm) were cut on an ultra-microtome (Fig. 9.1 F). After being stretched with fumes of

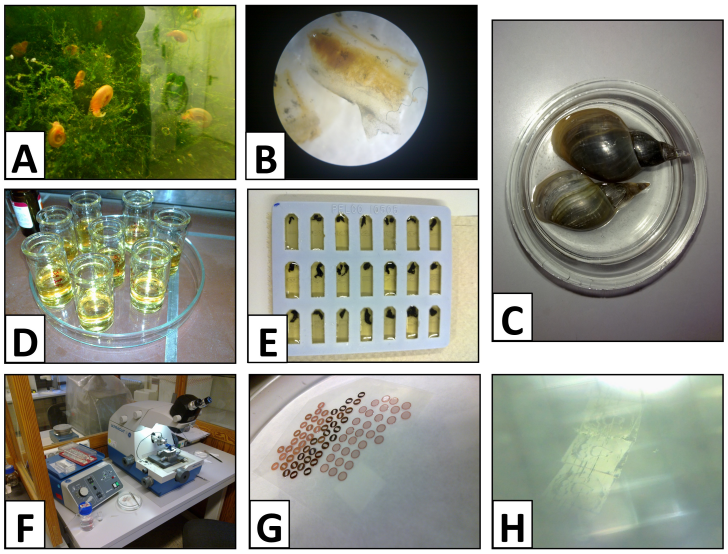

Figure 9.1. ***Sample Preparation for EM.*** *(A) B. glabrata in water tank. (B) Mantle tissue of B. glabrata. (C) Anesthesia of L. stagnalis. (D) Treatment of tissue with propylene oxide. (E) Samples embedded in araldite. (F) Ultra microtome. (G) Grids covered with formvar film. (H) Ribbon of ultrathin sections.*

xylol the sections were collected with copper grids, covered with formvar film (1.2 % in chloroform) (Fig. 9.1 G & H). Formvar films are really strong, stable and have great irradiation resistance (Hayat, 2000). They were stained with 2 % uranyl acetate in 50 % ethanol for 10 min and lead citrate for 2 min (Hanaichi, 1986; Sato, 1968). One drop of gold particles (1:50 diluted with water) was applied on each side of the grid that would be further used for collection of tilt series.

Phosphate buffer (0.2 M) according to Soerensen:

- 0.2 M Na_2HPO_4
- 0.2 M KH_2PO_4, until pH reaches value of 7.2

Embedding medium:

- 39 g Renlam M-1
- 36 g araldite Hardner Hy 964
- 1.5 g 2,4,6-tris-dimethyl-aminomethylphenol

For immune-electron microscopy, 1-3 mm^3 tissue pieces extracted from mantle and foot were fixed for 1.5 h in a solution of 3 % paraformaldehyde and 0.1 % glutaraldehyde in 0.1 M phosphate buffer pH 7.3. After washing steps in 0.1 M phosphate buffer and dehydration in ascending concentrations of ethanol, the material was embedded in LR-White and gelatin caps and polymerized in UV-light at 4 °C for

3 days, as previously described (Wolfrum & Schmitt, 2000). Ultrathin sections (70-100 nm) were collected on the grids and were further incubated for 2 min with sodium periodate ($NaIO_4$). Afterwards, they were washed with H_2O and incubated for 10 min with 0.1 % Tween in PBS. This solution works in a way, that the membranes are permeable for the antibody. 10 min incubation in 50 mM ammonium chloride (NH_4Cl) in PBS, washing steps with PBS and 30 min incubation with blocking solution (0.05 % cold water fish gelatin + 0.1 % ovalbumin in PBS) followed. 20 μl of the primary antibody was applied to the sections (1:100 in blocking solution). This binding took place at 4 °C for 2 days. For these experiments the following antibodies were tested:

- monoclonal mouse anti-actin antibody 'clone C4' for *B. glabrata* experiments from Seven Hills Bioreagents (Cincinnati, USA)
- monoclonal mouse anti-actin antibody 05 for *L. stagnalis* experiments from Thermo Scientific (Schwerte)
- polyclonal rabbit anti-*Aplysia* hemocyanin antibody from Charles River (Sulzfeld)

The next day, washing steps with PBS and 10 min incubation with immune-gold buffer (0.1 % ovalbumin + 0.05 % cold water fish gelatin + 0.01 % Tween20 + 0.5 M NaCl in 10 mM phosphate buffer pH 7.3) followed. The secondary nanogold-coupled anti-mouse antibody was applied on the sections (2 h in room temperature). The rest of the antibody was removed with washing steps in PBS and the antibody already bound on the tissue was fixed with 5 min incubation in 1 % glutaraldehyde in PBS. This solution was removed with H_2O and the sections were let to air-dry overnight. During the last day, nanogold-labeling was silver-enhanced according to Danscher (1981). The sections were contrasted with 2 % uranyl acetate and lead citrate (Hanaichi, 1986; Sato, 1968).

Some *B. glabrata* and *L. stagnalis* individuals were deprived of food by maintaining them for 96 h in pure freshwater, covered with aluminium foil. Other individuals that were fed normally were exposed to cadmium containing conditions. Different concentrations of cadmium chloride (0.025 mg/l, 0.05 mg/l & 0.1 mg/l) and different durations of the treatment (12, 48 and 96 h) were tested. The fixation of mantle and foot tissues followed as described above.

9.3.2. High pressure freezing and freeze substitution

For a better preservation of the tissue, the specimen was frozen under high pressure (2100 bars), (Cavalier et al., 2009) using the high pressure freezing machine (Engineering Office M. Wohlwend GmbH, Switzerland) (Fig. 9.2). The specimen (fresh and up to 200 μm thick) was enclosed and protected in a small volume between

two specimen carriers (aluminum type A specimen carrier, 100 μm/200 μm cavity; aluminum type B specimen carrier, flat/300 μm cavity) and locked inside the specimen pressure chamber. Dextran (20 % in water) was used as a cryo-protectant. Both carriers were dipped in hexadecene. Liquid nitrogen was used as a cooling medium.

To ensure high quality preservation of biological samples, the high pressure freezing technique was combined with freeze substitution and resin embedding. This included dehydration of the cryo-fixed samples at -90 °C by substituting the ice for an organic solvent. More detailed, the cryo-fixed samples were put at -90 °C into the substitution medium (0.1 % UA + 0.2 % OsO_4 + 5.0 % H_2O in acetone) inside the freeze substitution machine (EM, AFS, Leica Microsystems) for 2 days (Fig. 9.3). The whole duration of the protocol was between 17 and 20 h, depending on the time when the samples should be finished on the next day. During two thirds of the whole substitution time the samples were kept below -80 °C to prevent formation of ice crystals. After that, they were slowly warmed up to 0 °C and left at this temperature for 30 min before they were taken out and warmed up to room temperature. The samples were rinsed in pure acetone (3x 5 min) and infiltrated in EPON (aceton:EPON 3:1 for 2 h, 1:1 for 2 h, 1:3 for 2 h and pure EPON overnight). On the next day, polymerization took place at 60 °C for 48 h. Ultrathin sections were collected afterwards using a Leica ultramicrotome.

Figure 9.2. ***High Pressure Freezing Machine.*** *Enlargement view of the aluminium box for storage of grids.*

Figure 9.3. ***EM AFS Freeze substitution machine.*** *Enlargement view of the loading stage.*

9.3.3. Negative staining of proteins

The extraction of hemolymph proteins from snails was done as described (Lieb et al., 2006; Moeller et al., 2011). Using a pipette, the hemolymph was collected, centrifuged and the supernatant was diluted with 20 ml Tris buffer. The concentration of the hemolymph proteins was determined at 280 nm at the photometer.

For negative staining of proteins on carbon-coated copper grids (final concentration of protein: 0.1 mg/ml), the droplet method was applied with 1 % uranyl acetate (de Carlo & Harris, 2011; Harris & Scheffler, 2002).

9.3.4. Collection of data and tilt series at the electron microscope

Electron micrographs were taken on a TemCam-F416 4K 4K charge-coupled device (CCD) camera. The Tecnai12 transmission electron microscope was equipped with a LaB_6 electron source and operated at 120 kV. In order to view the cells in 3D (Baumeister et al., 1999; McIntosh et al., 2005), tilt series over a tilt range of -60 ° to +60 ° with 1.5 ° increments were recorded. The magnification of 23.000×

(0.929 nm pixel size on the CCD camera) was binned by the factor 2 (2048×2048 pixels micrographs). The EM-MENU 4 software package was used to collect the tilt series.

9.3.5. Data processing and 3D reconstruction

The set of TIFF image files was converted into a single "mrc" file using the IMAGIC software. Alignments and weighted back-projection-based reconstructions of raw tilt series using approximately 15 fiducials were computed with eTomo (a program of the IMOD software package). The reconstructions were further visualized using the AMIRA software package.

A semi-automated procedure using the module 'e2boxer' implemented in the EMAN2 software package was used in order to count the electron-dense granula in electron micrographs.

9.4. Energy dispersive X-ray spectroscopy - transmission electron microscopy (EDX-TEM)

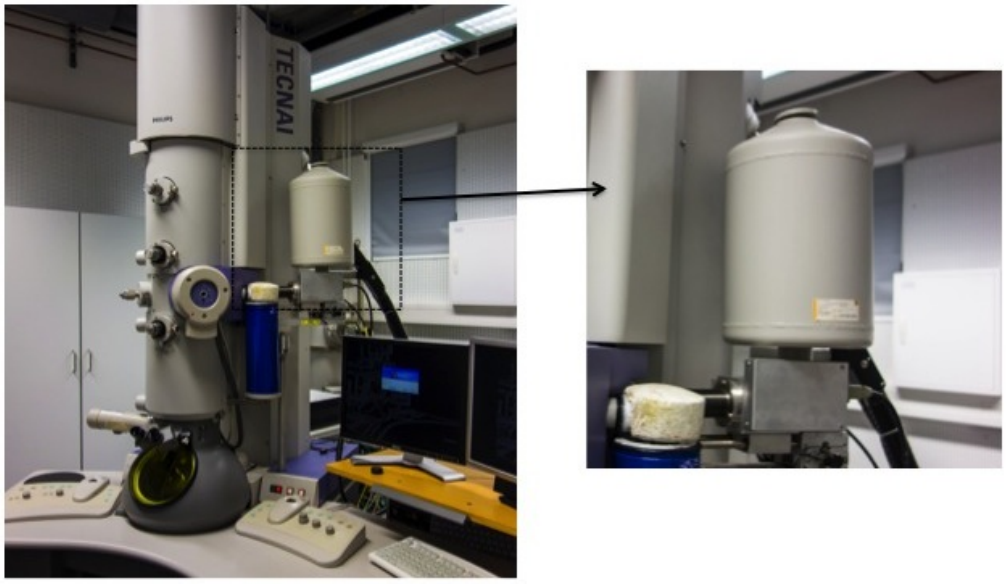

Figure 9.4. ***FEI Tecnai 30 equipped with the EDX spectrometer.***

In an attempt to study the elemental composition of the increased number of electron dense granula observed in our EM images after contamination, EDX analysis

was performed on an EM Tecnai F30 running in Scanning TEM (STEM) modus (Fig. 9.4). Without excitation, an atom within the sample contains electrons in discrete electron shells. When the beam hits the sample, it may excite one of the electrons and eject it from the shell, leaving a hole. An electron from an outer shell fills the hole and the difference in the energy between these shells releases via a photon with a wavelength corresponding to that energy difference. Every element has its own typical electron shell, and hence the energy spectrum of the emitted photons is an element specific fingerprint. By measuring the number and the energy of the x-ray photons from a sample with an X-ray spectrometer it was possible to characterize the chemical composition of the sample.

9.5. Scanning transmission electron microscopy (STEM)

Figure 9.5. ***Leica EM MED020 High Vacuum Coating System.***

The F20 microscope was operated in STEM mode in order to collect diffraction patterns of the structures that resemble protein crystals. The grids were carbon coated in advance (Leica EM MED020) (Fig. 9.5). This was done to prevent burning

of the film and the sample during the collection of the diffraction patterns in high magnification as the electron beam was focused on the structure of interest.

Part III.

Results

10. *Biomphalaria glabrata*

10.1. Tissue distribution and abundance of rhogocytes

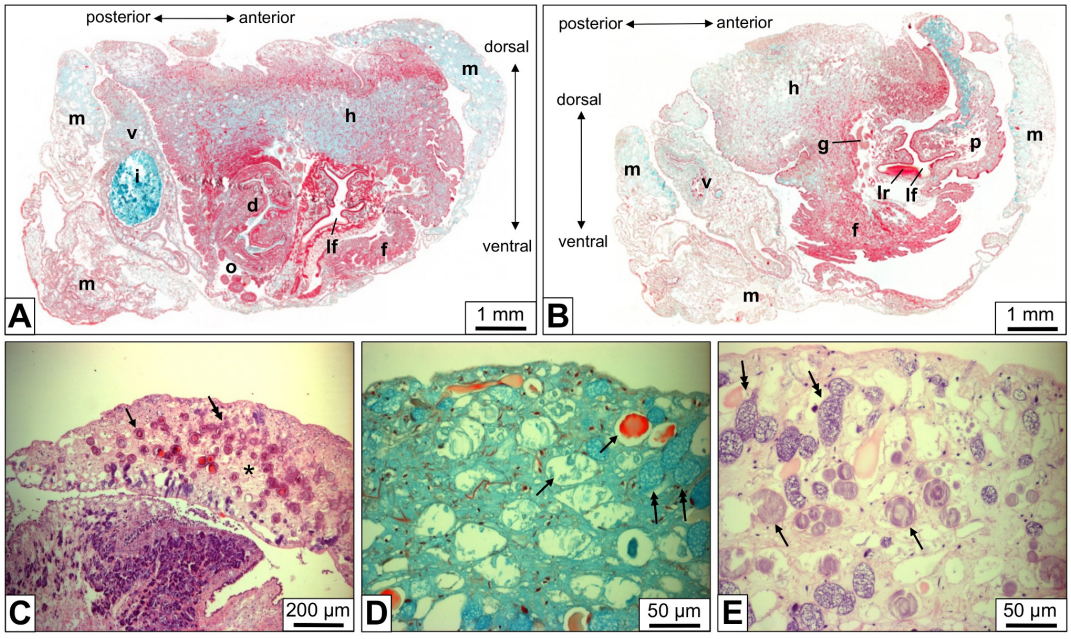

Figure 10.1. ***Light microscopy of paraffin-embedded mantle tissue sections of B. glabrata.*** *(A) Total scan of a diagonal cut across head, foot, visceral sac and mantle. (B) Total scan as in (A), but from a section 0.4 mm closer at the body surface. d, dart sac; f, foot; g, ganglion; h, head ; i, intestine with food mass; lf, lime fold; lr, lime ridge; m, mantle; o, ovo-testis; p, propodium; v, visceral hump. (C) Mantle tissue section, showing many scattered cells (arrow, double arrow) embedded in the connective tissue between muscle cells (asterisk). (D, E) At higher magnification, weakly stained cells filled with a homogeneous material (arrows) are discernable from somewhat smaller, strongly stained cells that are filled with a dense heterogeneous material (double arrows). Corresponding electron microscopical images (see Fig. 10.4) revealed that the strongly stained cells are rhogocytes and that the heterogeneous material is mostly endoplasmic reticulum and dense granula. The weakly stained cells are mucous glands. MP staining (A, B, D) and H & E staining (C, E) were applied. (Taken from Kokkinopoulou et al., 2014)*

3-5 μm sections of paraffin embedded *B. glabrata* were observed by light microscopy (Fig. 10.1 A, B). The foot was densely packed with muscle cells (horizontally or

vertically oriented). Such cells were also found in the mantle tissue, together with secretory cells containing material that might be further used for shell formation. Both body parts showed many solitary rhogocytes and clustered rhogocytes (Fig. 10.1 C-E). Their abundance was much higher in the mantle tissue. They were easily identified from their rich endoplasmic reticulum that was strongly stained. Corresponding ultrathin tissue sections are presented in Fig. 10.4 (for anatomy of *Biomplaharia* see Abdel-Malek, 1955).

10.2. Hemoglobin traced by immunohistochemistry and *in situ* hybridization

In situ hybridization was performed using two DIG-labeled antisense-cDNA probes, encoding a specific fragment of *B. glabrata* hemoglobin isoforms BgHb1 and BgHb2, respectively. The size of the PCR products was estimated by means of GeneRuler^{TM} DNA ladder mix (Fig. 10.2).

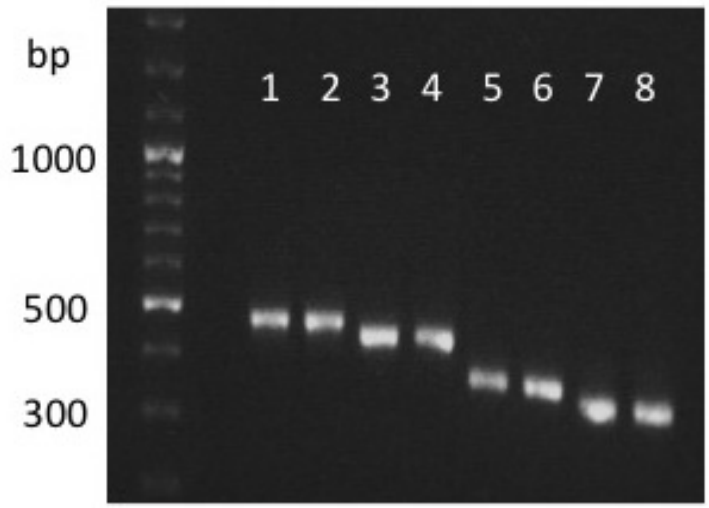

Figure 10.2. ***Agarose gel electrophoresis of PCR products.*** *First sample: GeneRuler^{TM} DNA ladder mix. Lane 1,2: B. glabrata acetylcholine binding protein isoform 1 (BgAChBP1). Lane 3,4: BgAChBP2. Lane 5,6: B. glabrata hemoglobin isoform 1 (BgHb1). Lane 7,8: BgHb2.*

In immunohistochemistry using rabbit anti-BgHb primary antibodies, cells identified from their morphology as rhogocytes showed a strong reaction (Fig. 10.3 A, B). The staining was much weaker in the hemolymph spaces. This higher concentration of hemoglobin inside the rhogocytes suggests that this cell type might synthesize the hemoglobin.

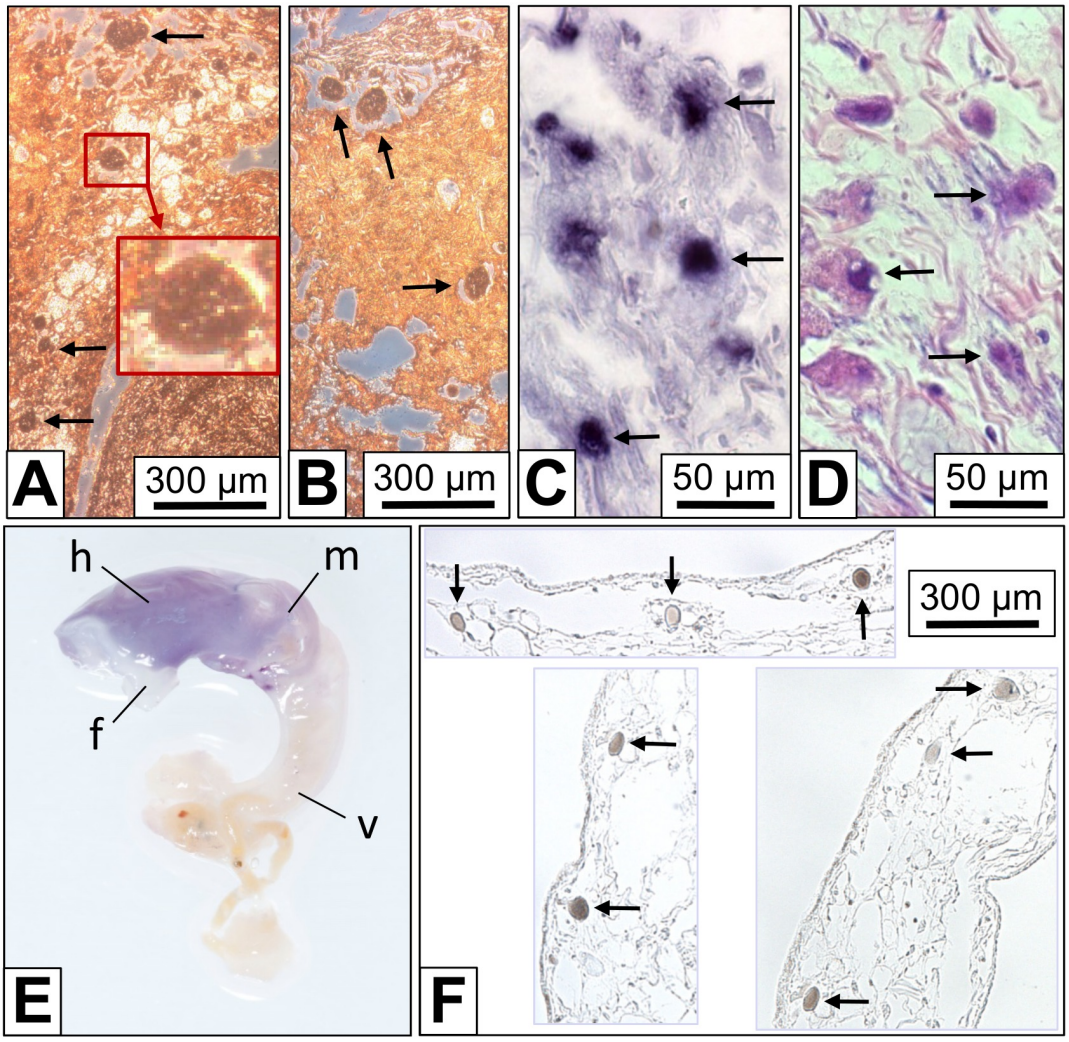

Figure 10.3. ***Detection of B. glabrata hemoglobin (BgHb) in tissue sections and whole mounts.*** *(A, B) Indirect immunohistochemistry with rabbit anti-BgHb antibodies on mantle tissue sections. The weak background staining might result from hemoglobin freely dissolved in the hemolymph spaces. The strongly stained cells are morphologically identified as rhogocytes (arrows). The insert shows an enlargement of the region in the red box. (C) In situ hybridization with antisense BgHb1-h cDNA (see Table 8.1 in Part II) performed on a mantle tissue section. Note strong reaction of cells that are morphologically identified as rhogocytes (arrows). (D) A section next to that seen in (C), stained with Movat's pentachrome to visualize rhogocytes (arrows). (E) Whole mount in situ hybridization using antisense BgHb2-i cDNA (see Table 8.1 in Part II). Note blue staining of head (h), foot (f) and mantle (m) and negative reaction of the visceral hump (v). Total length of the animal was 2 cm. (F) Three different paraffin-embedded tissue sections of a whole mount as shown in (E), but treated with antisense BgHb1-h cDNA. Note specific labeling of cells morphologically identified as rhogocytes (arrows). (Taken from Kokkinopoulou et al., 2014)*

For *in situ* hybridization, the probes were applied on paraffin sections (Fig. 10.3 C) and on whole mounts (Fig. 10.3 E, F); in both cases, a positive reaction in mantle and foot was observed. Both DNA probes reacted in a similar pattern. These results confirm that rhogocytes are the site of hemoglobin synthesis in *B. glabrata*.

10.3. Ultrastructure of rhogocytes

In the electron microscope, many rhogocytes were identified in tissue sections of *B. glabrata*. Fig. 10.4 presents an overview of mantle tissue.

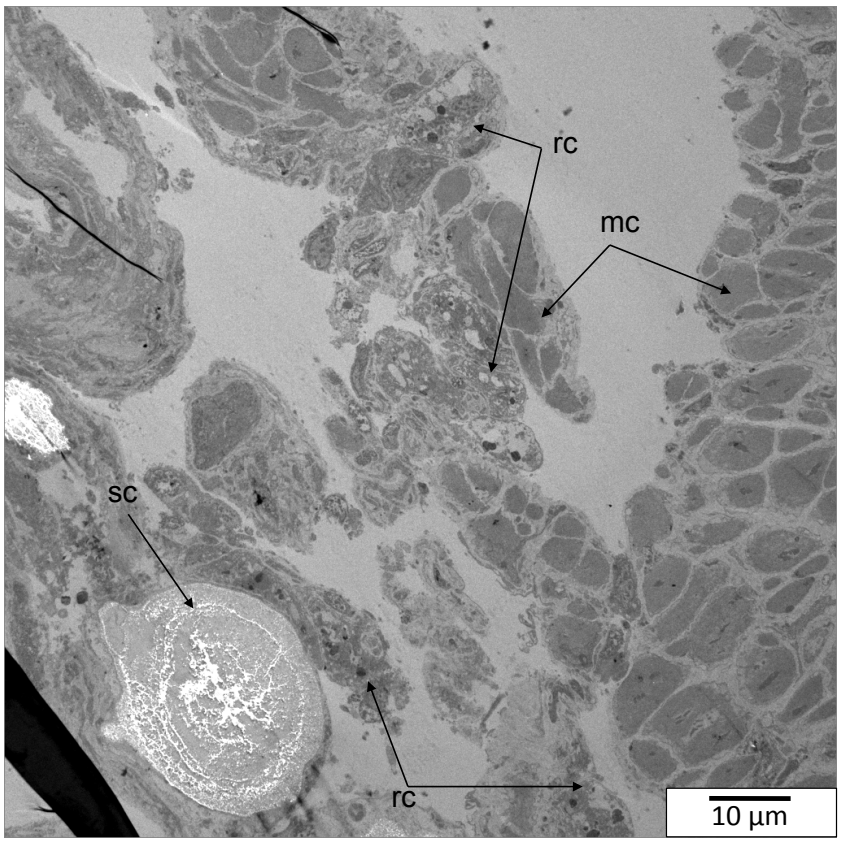

Figure 10.4. ***Electron microscopy image of chemically fixed mantle tissue of B. glabrata.*** *Rhogocytes (rc, arrows) were found between muscle cells (mc, arrows) and secretory cells (sc, arrows). They were easily identified by their ultrastructure.*

There was a great variation in size and shape. As shown in Fig. 10.5 B, the rhogocytes were easily identified by their large nucleus, many electron dense granula, a prominent rough endoplasmic reticulum and the enveloping basement membrane. Mitochondria and dictyosomes were also observed. In Fig. 10.5 C, the characteristic feature of rhogocytes is presented, namely the pocket-like lacunae created by

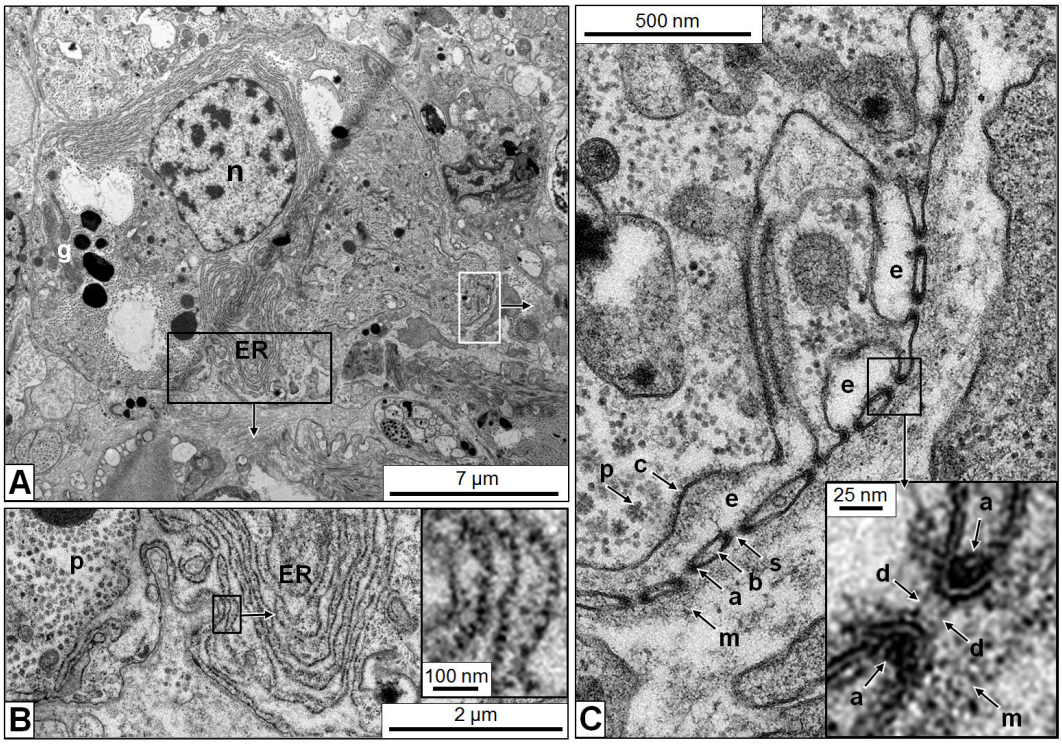

Figure 10.5. ***Electron microscopy of a foot tissue section showing a typical rhogocyte.*** *(A) Overview of the rhogocyte. Note the large nucleus (→n), electron-dense granula (→g) and the abundant endoplasmic reticulum (→ER). (B) Enlargement of the region indicated by a black box in (A), showing that the endoplasmic reticulum (→ER) is lined with ribosomes (i.e. rough ER). Note the protein-like material (→p) in the adjacent ER lacuna. The insert in (B) shows a further enlargement of the region indicated by the black box in (B) to visualize individual ribosomes. (C) Enlargement of the region indicated by a white box in (A), showing several extracellular lacunae (→e) with cytoplasmatic bars (→b) and 20 nm slits (→s). In the bars, adjacent to the slits, actin-containing electron-dense material is visible (→a). Also note the extracellular basement membrane (→m) and the coat (c) lining the plasma membrane at the extracellular lacunae. In the adjacent cytoplasm, protein-like material is seen (→p). The insert in (C) shows a further enlargement of the region indicated by a black box in (C) to visualize the slit diaphragm (→d) as a two parallel small rods. Also note, in this insert, the actin-containing electron-dense material (→a) and the basement membrane (→m). The gully cover-like cytoplasmic bars are cut here in transversal section; for a longitudinal section, see Fig. 10.6 B. (Taken from Kokkinopoulou et al., 2014)*

invaginations of the plasma membrane and bridged by cytoplasmic bars. The cytoplasmic bars left a gap with a width of approx. 20 nm, which formed a very short passage in this slit apparatus. These bars were connected by a thin diaphragm (Fig. 10.5 C).

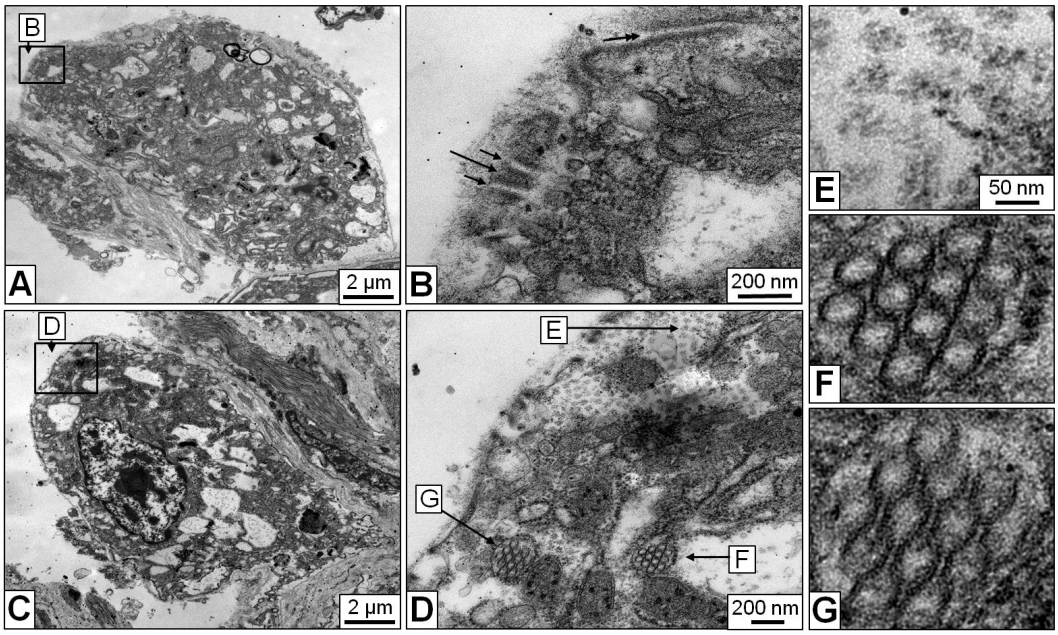

Figure 10.6. ***Electron microscopy of mantle tissue sections.*** *(A) Rhogocyte, with the nucleus not visible in this section. (B) Enlargement of the area marked in (A), showing a longitudinal cut through several cytoplasmic bars (for a transversal cut, see Fig. 10.5 C). It is obvious that the cytoplasmic bars (long arrow) border slits (short arrows). Note that these slits can be very long (double arrow). (C) Rhogocyte, with the large nucleus visible. (D) Enlargement of the area marked in (C), showing several ER lacunae filled with circular structures 40-50 nm in diameter (→F). These structures might be cylindrical hemocyanin molecules viewed from the top. However, in some areas these structures show open connections (→G) which is not explained by the typical hemocyanin structure (see, however, Fig. 10.12). Also note the more amorphous protein-like material in other lacunae (→E) that is interpreted as hemoglobin. (E-G) Enlargements of the regions marked in (D). (Taken from Kokkinopoulou et al., 2014)*

This path appeared longer, if viewed from a longitudinal view of the cytoplasmic bars (Fig. 10.6 A, B). The slit apparatus was probably not static and the width between the cytoplasmic bars could vary. Moreover a highly dense material was observed at the cytoplasmic bars at the insertion side of the slits (Fig. 10.6 C).

The extracellular lacunae of the rhogocytes were either empty or filled with material that was likely hemoglobin molecules (Fig. 10.6 C-E), as concluded from their large amount, particle size (approximately 25 nm) and globular shape. Intracellular vesicles containing electron dense hollow rings of approx. 50 nm, interpreted as top

views of hemocyanin molecules, were often found (Fig. 10.6 D, F, G). In *B. glabrata*, hemocyanin is expressed as a trace component (Lieb et al., 2006).

3D reconstruction revealed more details of the slit apparatus. The slit diaphragm was indeed a bundle of filaments (Fig. 10.7 A). Particles assumed to be hemoglobin and many coated vesicles were observed inside the invaginations (Fig. 10.7 A). Such vesicles were found further in the neighboring cytoplasm. Highly dense material was observed at the cytoplasmic bars adjacent to the slits. The corresponding 3D model is presented in Fig. 10.7 B.

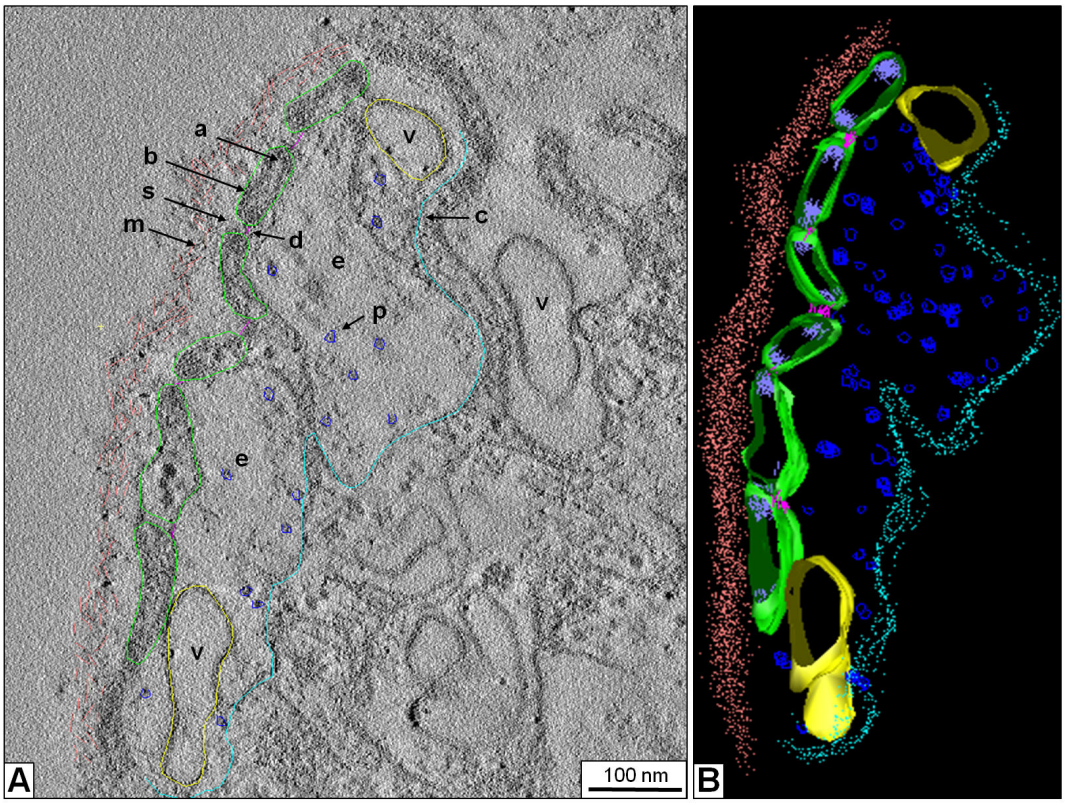

Figure 10.7. ***3D Ultrastructure of a rhogocyte region with slit apparatus.*** *(A) Electron tomogram slice of chemically fixed mantle tissue, superimposed by a 3D reconstruction performed in IMOD. (B) The corresponding 3D model visualized and sectioned by IMOD. Note the enveloping basement membrane (→m, salmon), the extracellular lacuna (→e) filled with protein particles (→p, blue), the coated plasma membrane (c, cyan), the bridging cytoplasmic bars (b, green), the slits (→s) with the diaphragm (→d, magenta). Coated vesicles (v, yellow) inside the extracellular lacuna and the neighboring cytoplasm are also seen. Highly dense material (a, purple) is observed at the cytoplasmic bars adjacent to the slits; it is likely to contain actin bundles (see Fig. 10.10). (Taken from Kokkinopoulou et al., 2014)*

The vesicles were often in contact with the plasma membrane, releasing their content. Moreover, the coated vesicles were either observed between the slit apparatus

and the basement membrane or directly fused with a slit (Fig. 10.8 A). Furthermore, vesicles were observed outside the basement membrane (Fig. 10.8 B). For further 3D reconstructions of *B. glabrata* rhogocytes see Part VI.

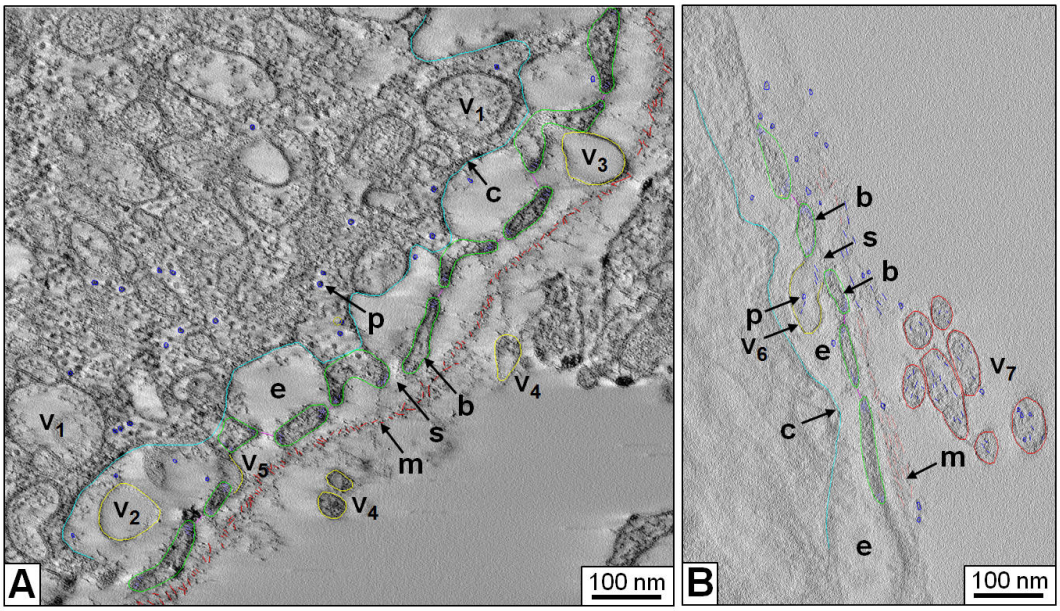

Figure 10.8. ***3D ultrastructure of a rhogocyte periphery with different locations of coated vesicles.*** *Electron tomograms with superimposed 3D reconstructions are shown. (A) Region showing the coated plasma membrane (c, cyan), several extracellular lacunae (e), diaphragmatic slits (→s) and the basement membrane (→m, red). Note coated vesicles (yellow) present in the cytoplasm (→v1), the extracellular lacunae (→v2), between slit apparatus and basement membrane (→v3), and outside of the latter in the adjacent hemolymph (→v4). A vesicle probably fused with the slit apparatus is also seen (→v5). (B) Region showing a coated vesicle (→v6, yellow) in open contact with a diaphragmatic slit (→s) formed by neighboring cytoplasmic bars (→b, green). The vesicle contains protein-like material (p, blue) that is likely to be transported by the vesicle through the slit. Note similar vesicles (→v7, red) outside of the basement membrane (→m). (Taken from Kokkinopoulou et al., 2014)*

In order to visualize the cells in close to native conditions, the mantle tissue was fixed by high pressure freezing and freeze substitution. In this procedure, a much lower amount of chemical fixatives is applied. The resulting samples showed a significantly better preservation of the structure (Fig. 10.9). In the rhogocytes, numerous vacuoles filled with protein particles were observed. The latter was either the putative hemoglobin (e.g. Fig. 10.9 D), or the putative hemocyanin (e.g. Fig. 10.9 F). The hemocyanin was also present as pseudo-crystalline arrays (e.g. Fig. 10.9 H).

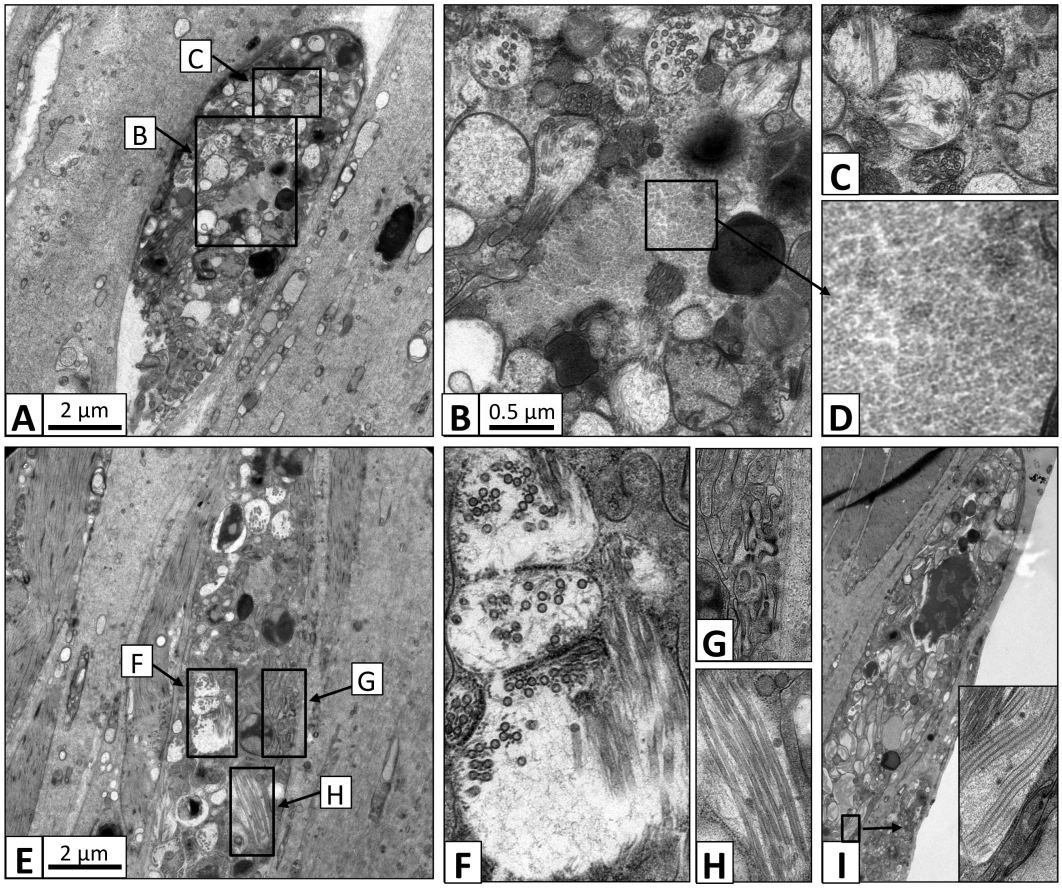

Figure 10.9. ***Electron microscopy of mantle tissue sections, fixed by high pressure freezing and freeze substitution.*** *(A) Rhogocyte filled with protein molecules. (B) Area seen in (A) with vacuoles filled with hemoglobin molecules and other circular structures. (C) Area seen in (A) with vacuoles filled with pseudo-crystalline arrays and circular structures. (D) Vacuole presented in (A) filled with putative hemoglobin molecules. (E) Rhogocyte with numerous vacuoles. (F) Vacuoles presented in (E), filled with circular structures (putative hemocyanin). (G) Invagination of plasma membrane bridged by cytoplasmic bars. Note the highly dense material at the edges. (H) Vacuole with longitudinal view of the circular structures, also referred to as pseudo-crystalline arrays. (I) Rhogocyte with a large nucleus. Area indicated in the black box presents a vacuole filled with perfectly ordered cylinders, probably representing a different form of longitudinal view of the circular structures.*

10.4. Immunogold localization of actin

As previously mentioned, a highly dense material was observed in the cytoplasmic bars at the insertion side of the slits. This material is assumed to play a role in the trafficking through the slits. Actin is one of the key players in the trafficking through the slits in case of mammalian podocytes and insect nephrocytes (Weavers et al., 2009; Ichimura et al., 2003). Therefore, a monoclonal anti-actin primary antibody (Lessard, 1988) that binds to all known actins throughout the animal kingdom and beyond was used for immune-gold electron microscopy.

As presented in Fig. 10.10, gold particles were detected in the cytoplasm and the nucleus of rhogocytes. This result was expected, as actin is a component of the cytoskeleton and chromatin complexes. Moreover, the gold particles were detected at the cytoplasmic bars, notably at the regions of the dense material (Fig. 10.10 B, C). That means that actin is likely to be one of the major components of this highly dense material.

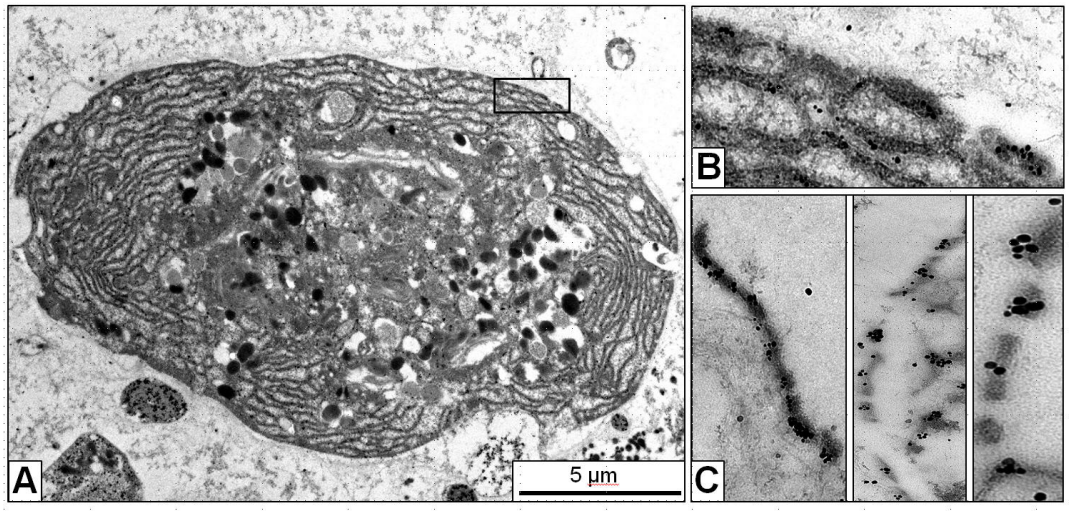

Figure 10.10. ***Immunogold localization of actin in the slit apparatus.*** *(A) Electron microscopy of a rhogocyte in a mantle tissue section labeled with immune-gold particles against actin. (B) A region in (A) imaged at higher primary magnification, showing gold labeling. (C) Part of the slit apparatus of three different rhogocytes, showing anti-actin immune-gold labeling in the electron-dense regions of the cytoplasmic bars adjacent to the slits. (Taken from Kokkinopoulou et al., 2014)*

10.5. Detection, structure and localization of nephrin

Zhuang et al. (2009) demonstrated that there is a phylogenetic relationship between mammalian podocytes and insect nephrocytes by proving that related proteins, notably nephrin, form the slit diaphragm. By screening the *B. glabrata* genome database, B. Lieb in our group found a gene encoding a complete nephrin. For all the structural domains present in human nephrin (Kestilä et al., 1998) an equivalent sequence exists in *B. glabrata* nephrin. Using a variety of crystal structures as templates, we produced a homology model of the protein (presented in Kokkinopoulou et al., 2014).

Furthermore, guinea pig anti-nephrin antibodies were used for immunofluorescence microscopy that revealed strong labeling of rhogocytes, mainly in the cell periphery (Fig. 10.11).

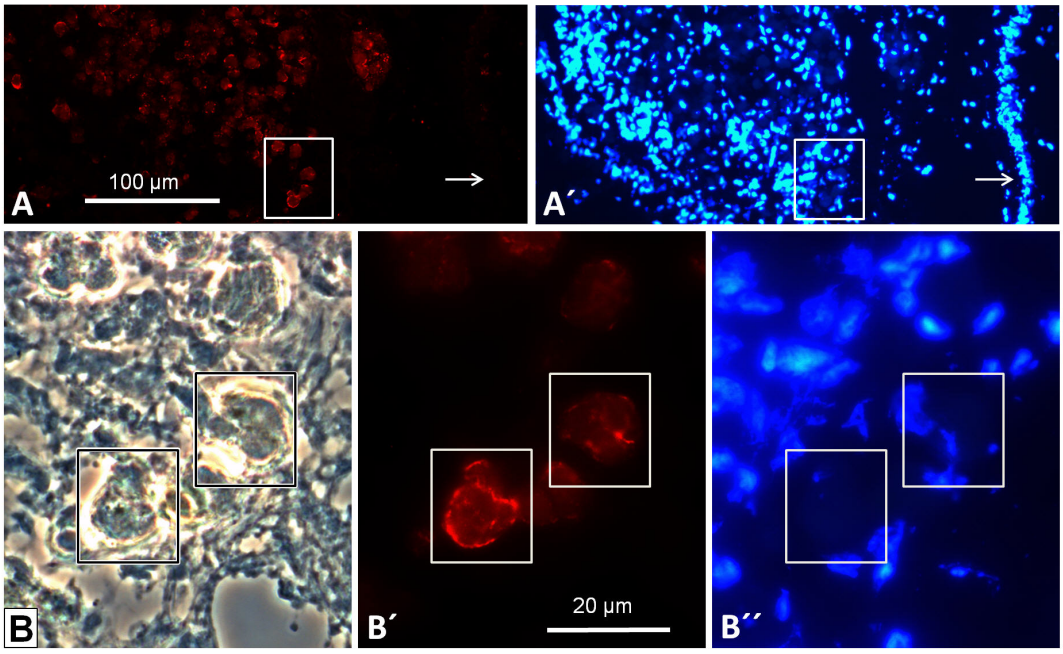

Figure 10.11. ***Immunofluoresence microscopy of a mantle tissue section with anti-nephrin antibodies.*** *(A) Cluster of rhogocytes at 250x primary magnification, showing positive reaction with guinea pig anti-nephrin antibodies. Note negative reaction of the mantle epithelium (arrow). (A') The same section stained with DAPI to visualize the cell nuclei (arrow, mantle epithelium). (B-B") The boxed area in (A, A') shown at 1000x primary magnification: Phase contrast optics (B), immunofluorescence (B'), and DAPI staining (B"). Two rhogocytes are highlighted in boxes. Note that the positive reaction is mostly restricted to the cell periphery. (Taken from Kokkinopoulou et al., 2014)*

10.6. Response of rhogocytes to deprivation of food and to cadmium stress

In order to check how the rhogocytes react in animals under stress conditions, we fixed *B. glabrata* individuals that were deprived of food for 96 h. The rhogocytes of such individuals showed less electron-dense granula and plasma membrane invaginations (Fig. 10.12 A). Moreover, we observed an increase of vesicles filled with the 50 nm rings interpreted as hemocyanin molecules (Fig. 10.12 B, C).

In case of *B. glabrata*, besides hemoglobin and a minor portion of acetylcholine-binding protein, traces of hemocyanin are expressed. In *B. glabrata*, it is a solitary decamer 35 x 18 nm (Fig. 10.12 D), composed of a cylinder wall, lacking the internal collar (Markl, 2013; Lieb et al., 2006; Saur et al., 2012). In general, gastropod hemocyanin is a cylindrical didecamer 35 x 35 nm with an outer wall and an internal collar (reviewed by Markl, 2013). The diameter seen in Fig. 10.12 B, C is probably a stain artifact. By reconstructing such vesicles it was proved that the rings represent the top-view of elongated stacks of short cylinders (Fig. 10.12 E). Prior to the fixation, hemolymph extracted from the starved animals showed a significant enrichment in hemocyanin molecules, suggesting that the hemocyanin synthesis is somehow up-regulated in starved snails.

Table 10.1. ***Number of electron-dense granula in individual rhogocytes from untreated and $CdCl_2$-contaminated animals (B. glabrata).***

untreated			contaminated		
2	4	6	8	14	21
2	5	6	8	14	22
3	5	8	10	16	24
3	5	8	10	16	24
3	5	9	12	20	28
3	5	9	13	21	
3	5	9	13	21	
$\varnothing = 5.2$			$\varnothing = 15.9$		

Next, we compared the previous rhogocytes response to the one to cadmium stress. Individuals that survived after 96 h in water containing 0.05-0.1 mg/l cadmium chloride showed numerous but small rhogocytes, indicating that their number was increased by cell division. The number of electron dense granula and mitochondria was also increased (Fig. 10.12 F). Using the module 'e2boxer' of the EMAN2 software package, the increase of electron dense granula could be quantified and thereby confirmed (Table 10.1). An important observation was that extracellular lacunae with slit apparatus were much more frequently detected due to the intensive

folding of the cell surface, indicating an overall increase of the filtration capacity (Fig. 10.12 G).

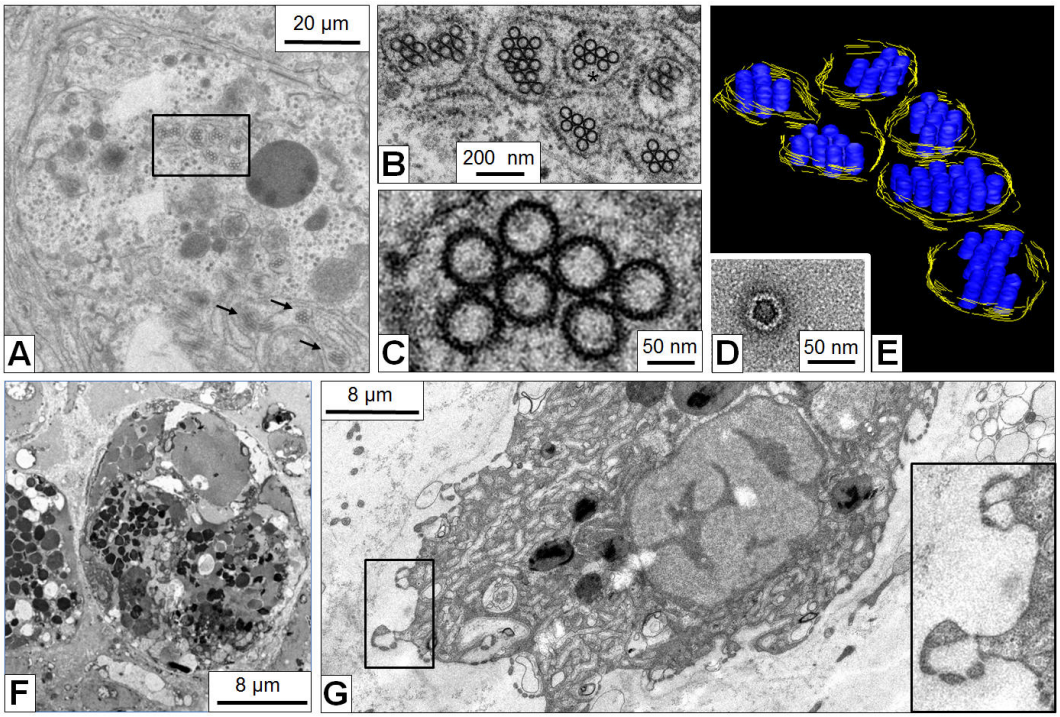

Figure 10.12. ***Response of rhogocytes to deprivation and cadmium stress.*** *(A) Electron microscopy of a rhogocytes from an individual of B. glabrata deprived of food for 96 h. Electron-dense granules and extracellular lacunae with slit apparatus are rarely observed. Vesicles containing hemocyanin-like particles are abundant (box and arrows). (B) Higher magnification of the region marked in (A) by a box. (C) Close-up view of the region marked in (B) by an asterisk. Note that the 50 nm rings show no connections, in contrast to those in Fig. 10.6. (D) A single B. glabrata hemocyanin molecule extracted from an electron microscopical image of negatively stained hemolymph proteins. Note that its outer diameter (approx. 35 nm) corresponds to the diameter of the internal material of the 50 nm rings. In other words, the black annulus visible in (C) is heavy metal stain and not the protein cylinder wall, and corresponds to the dark uranyl acetate halo surrounding the molecule in (D). (E) 3D model derived from electron tomography of a similar area as in (B). Note that the hemocyanin-like particles now appear as stacks of short cylinders. This is in good agreement with the quaternary structure of B. glabrata hemocyanin which is a hollow cylinder 35 nm in diameter and 18 nm in height. (F) Rhogocyte of a cadmium-contaminated animal. Note large number of electron-dense granula (for comparison, see Fig. 10.5). (G) Rhogocyte of a cadmium-contaminated animal, suggesting significant increase of the filtrating cell surface. The insert shows an enlargement of the boxed area. (Taken from Kokkinopoulou et al., 2014)*

11. *Lymnaea stagnalis*

11.1. Tissue distribution and abundance of rhogocytes

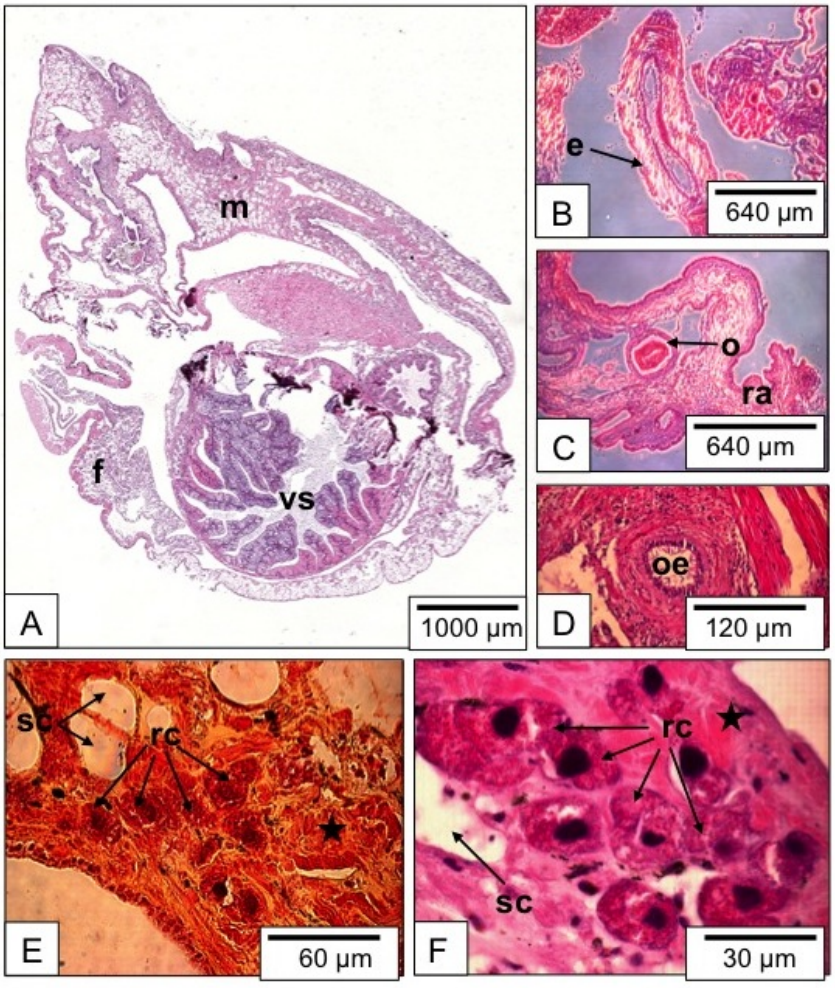

Figure 11.1. ***Light microscopy of paraffin-embedded tissue sections of L. stagnalis.*** *(A) Total scan of a diagonal cut through the animal. (B-F) Paraffin-embedded mantle tissue sections of L. stagnalis. (B-D) Prominent structures such as eye (→e), odontophore (→o), radula (ra) and oesophagus (oe). (E, F) Rhogocytes (→rc) are visible between muscle cells (star) and secretory cells (→sc). (A-D, F) H&E staining. (E) MP staining.*

An individual of *L. stagnalis* was entirely cut into sections 3-5 μm in thickness (Fig. 11.1 A). The slices were stained with H&E and MP (Fig. 11.1) and further analyzed by light microscopy. The rhogocytes were identified (often in clusters) due to their substructure among muscle cells, undifferentiated cells or secretory cells (Fig. 11.1 E, F). More muscle cells were observed in the foot tissue in comparison with the mantle tissue, where more secretory cells were seen, with material that would be further used for shell formation. Also, other important structures were seen, such as the eye (Fig. 11.1 B), the odontophore (Fig. 11.1 C) and the oesophagus (Fig. 11.1 D).

11.2. Hemocyanin traced by immunohistochemistry and *in situ* hybridization

In situ hybridization was performed on *L. stagnalis* whole mounts, using a DIG-labeled cDNA specific from RNA encoding a fragment of functional unit h of *L. stagnalis* hemocyanin (Fig. 11.2).

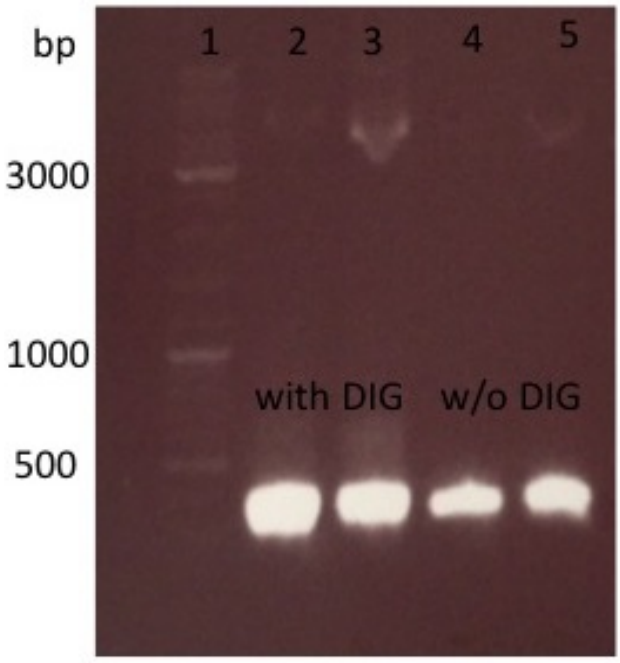

Figure 11.2. ***Agarose gel electrophoresis with DIG labeling of hemocyanin.*** *(1) GeneRuler^{TM} ladder mix. (2,3) Samples labeled with DIG labeling. (4,5) Samples without DIG labeling. The size of the PCR products was somewhat below 500 bp, which fits the value of 341 bp as calculated from the sequence.*

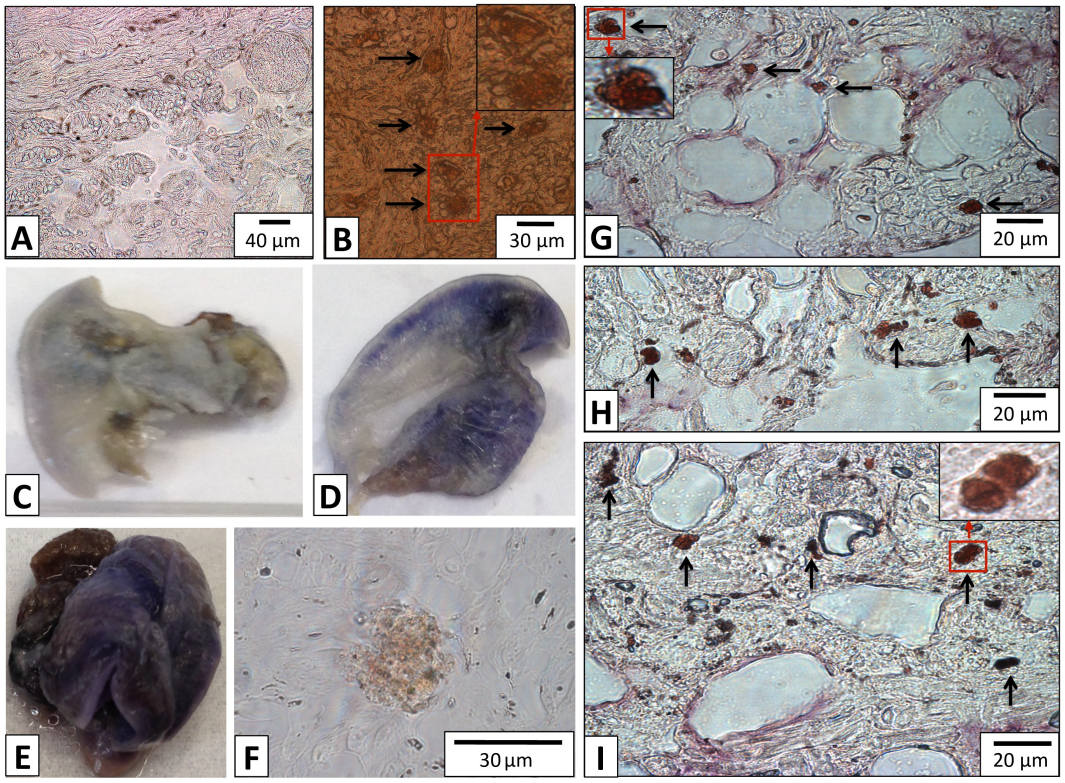

Figure 11.3. ***Detection of L. stagnalis hemocyanin (LsHc) in paraffin-embedded tissue and whole mounts.*** *(A,B) Immunohistochemistry on paraffin-embedded tissue sections of L. stagnalis. (A) Negative control. (B) Rabbit anti-Aplysia californica hemocyanin primary antibodies; note staining of rhogocytes (arrows). (C-E) Whole mount in situ hybridization. (C) The negative control, without addition of DIG-labeled probe. Mantle tissue is isolated. (D) 100 ng of DIG-labeled probe was added. Mantle tissue is isolated. Note the blue-purple staining. (E) 200 ng of DIG-labeled probe was added. Increased blue-purple staining of mantle tissue is observed. Total length of the animal was 2 cm. (F) Paraffin-embedded tissue section of the whole mount shown in (E). See specific labeling of cell morphologically identified as rhogocyte. (G-I) In situ hybridization with LsH cDNA on paraffin embedded tissue sections of new individuals of L. stagnalis. The strongly stained cells are morphologically identified as rhogocytes (arrows).*

Immunohistochemistry on *L. stagnalis* tissue sections with anti-*Aplysia californica* hemocyanin primary antibodies showed a strong signal in cells morphologically identified as rhogocytes (Fig. 11.3 A, B, arrows). The obviously high concentration of this protein in rhogocytes suggests that hemocyanin is synthesized in these cells. The hemolymph spaces in between showed a weaker signal.

Positive reactions of the mantle tissue were observed (Fig. 11.3 D, E, arrows). The mantle tissue presented in Fig. 11.3 E was further sectioned to localize the signal of this reaction in cells that resemble the rhogocytes (Fig. 11.3 F). The same probe was used to perform *in situ* hybridization on paraffin sections. A strong and specific labeling of cells morphologically identified as rhogocytes was obtained (Fig. 11.3 G, H, I, arrows).

11.3. Ultrastructure of *L. stagnalis* rhogocytes

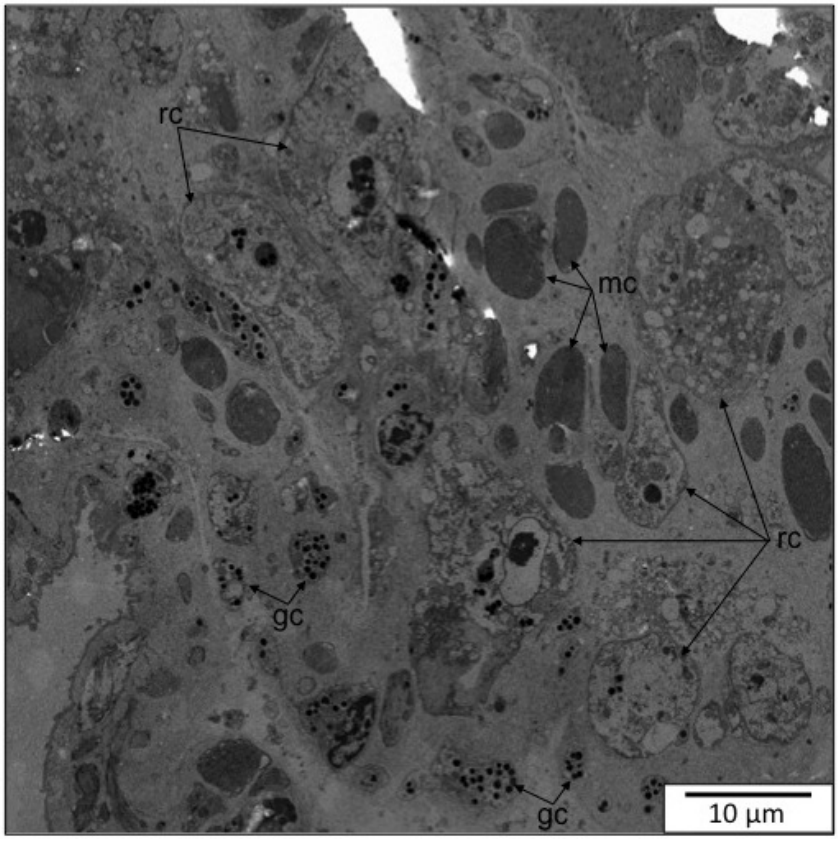

Figure 11.4. ***Electron microscopy image of chemically fixed mantle tissue of L. stagnalis.*** *Rhogocytes (→rc) were found between muscle cells (→mc) and granular cells (→gc), and they were identified by their ultrastructure.*

Electron microscopy data collected during this thesis confirmed previous studies on *L. stagnalis* (Sminia, 1972) that rhogocytes were abundant cell types besides muscle cells and granular cells in the connective tissue (Fig. 11.4). They were diverse in size and shape (Fig. 11.5 A). A typical rhogocyte is shown in Fig. 11.5 B (see also Figs. 11.6, 11.7, 11.8). A big nucleus, a prominent endoplasmic reticulum and a high number of electron dense granula were characteristic features. The most important feature was the invaginations of plasma membrane, bridged by cytoplasmic bars, seen either in longitudinal view (Fig. 11.5 C) or in top view (Fig. 11.5 E, F). The connecting slits were often observed along the whole surface of the bars if seen in side view. These invaginations were often filled with granular material, most likely being hemocyanin molecules (Fig. 11.5 D-F).

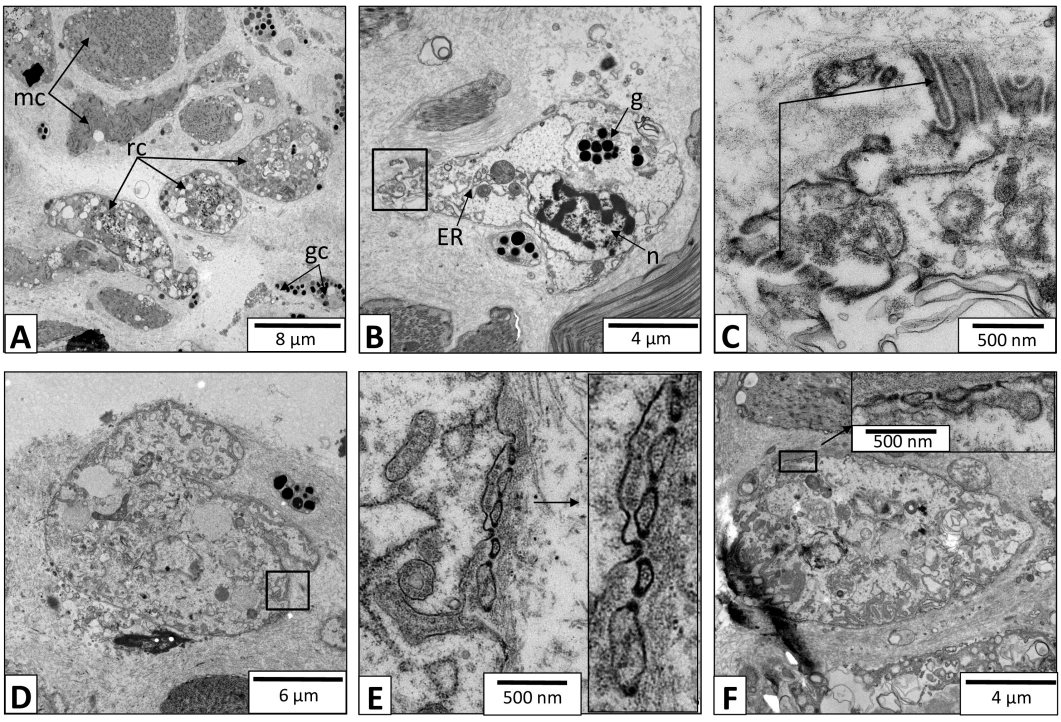

Figure 11.5. ***TEM of L. stagnalis mantle tissue sections.*** *(A-F): TEM images of chemically fixed mantle tissue of L. stagnalis. (A) Low magnification with rhogocytes (rc, arrows), muscle cells (mc, arrows) and granular cells (gc, arrows). (B) Medium magnification of a rhogocyte, exhibiting a big nucleus (n, arrow), endoplasmatic reticulum (ER, arrow) and many electron dense granula (g, arrow). The rectangle indicates the area seen in (C). (C) Higher magnification of the slit apparatus (arrows). The cytoplasmic bars are seen in longtangenital view. (D) Rhogocyte filled with hemocyanin. (E) Close-up view of the area marked in (D) showing the slit apparatus in top view. The invagination of plasma membrane is bridged by slits and filled with protein on both sides (arrow). See details in the close-up view. (F) Rhogocyte. Note the enlargement of the area marked in (F), showing individual molecules of hemocyanin inside the invagination and outside of the extracellular basal lamina.*

Numerous vacuoles filled with material resembling hemocyanin were identified in almost all rhogocytes (Fig. 11.6 B). The putative hemocyanin was observed in the rhogocytes either as individual cylindrical molecules 25 nm in diameter, reminiscent of those seen in the hemolymph as side and top views (Fig. 11.6 A), or as pseudo-crystalline arrays inside vacuoles (Fig. 11.6 C, F, see also Fig. 11.8). Particles resembling such hemocyanin molecules were often seen in the slit apparatus, either inside the invaginations or between the latter and the extracellular basal lamina-like structure (see also Fig. 11.5, 11.7, 11.8). In immunogold labeling experiments using anti-*Aplysia* hemocyanin antibodies, the hemolymph spaces between muscle cells and rhogocytes, and the interior of rhogocytes were marked (Fig. 11.6 D).

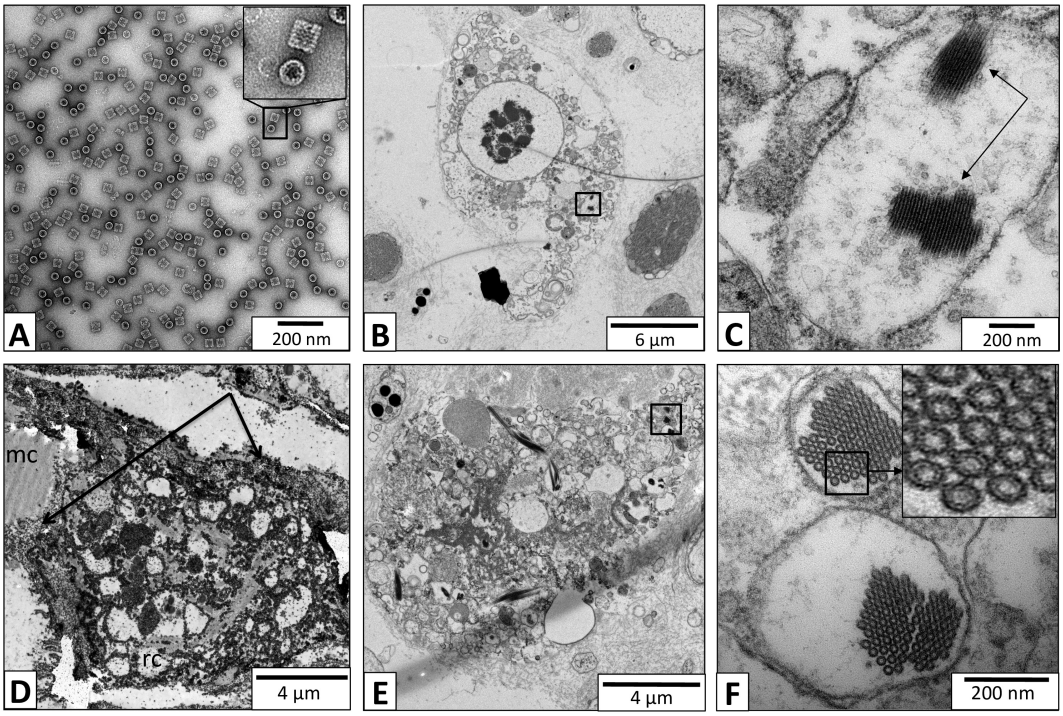

Figure 11.6. ***TEM of L. stagnalis mantle tissue sections.*** *(A) Purified hemocyanin and (B-F): TEM images of chemically fixed mantle tissue of L. stagnalis. (A) Negatively stained hemocyanin didecamers purified from L. stagnalis hemolymph (circles, top view; squares, side view). (B) Rhogocyte, with the area seen in (C) indicated by a rectangle. (C) A rhogocyte vacuole with two pseudo-crystalline hemocyanin arrays (arrows) surrounded by solitary hemocyanin molecules. (D) Overview of a rhogocyte (rc) labeled with immunogold particles against hemocyanin. Apart from staining inside the rhogocyte, note the staining of the area surrounding the rhogocyte and the neighboring muscle cell (mc) (arrows). (E) Overview of a rhogocyte with pseudo-crystalline arrays. (F) Close-up view of the area marked in (E), showing vacuoles filled with pseudo-crystalline arrays. The insert in (F) shows a further enlargement of the region indicated by the black box in (F) to visualize the top view of the proteins.*

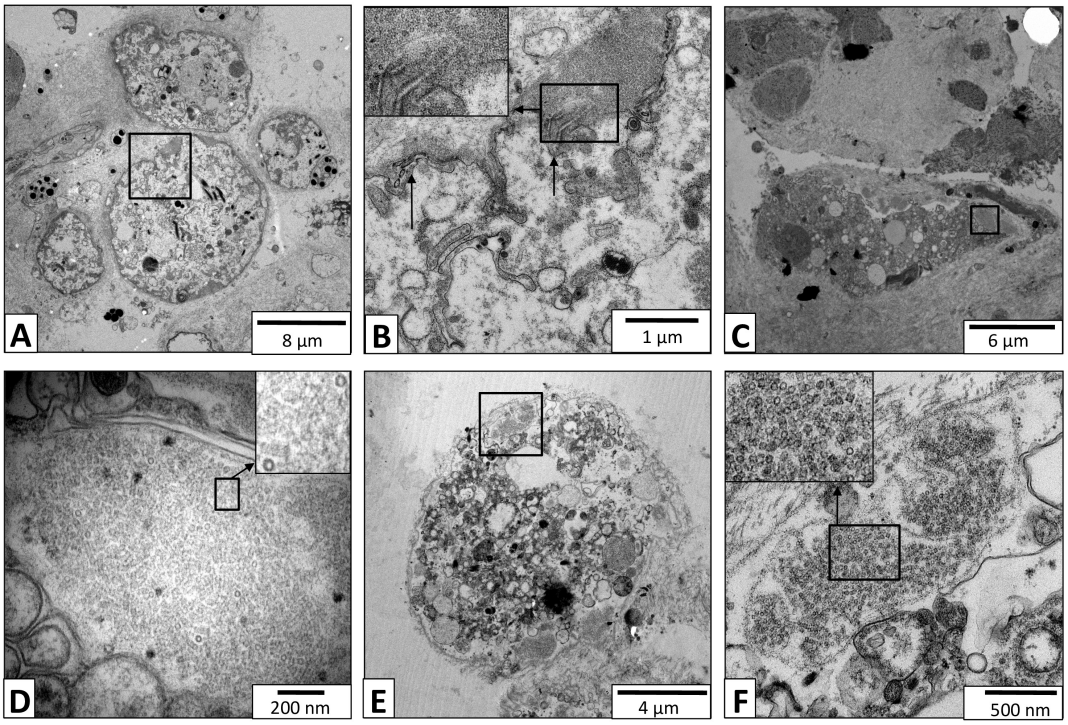

Figure 11.7. ***TEM of L. stagnalis mantle tissue sections.*** *(A) A group of rhogocytes in the connective tissue. (B) Close-up view of the area seen indicated in the box in (A). The insert shows a further enlargement of the region indicated by a black rectangle. The arrows show the invaginations of the plasma membrane filled with granular material. (C) Rhogocyte filled with protein. (D) Close-up view of the area seen in (C). The insert shows a further enlargement of the region indicated by a black box. The individual hemocyanin molecules appear in top and side view. (E) Overview of a rhogocyte filled with hemocyanin. (F) Close-up view of the area shown in (E). A vacuole filled with hemocyanin molecules seen in top and side view. For details see the insert.*

In Fig. 11.8 D, a vesicle transported its granular content to the invagination. As shown in the slices of the reconstructed tomogram in Fig. 11.9, such cytoplasmic vesicles seemed to release their granular contents inside the invagination. In the next step, they might be exported through the slits into the hemolymph. An external basal lamina-like structure surrounded each rhogocyte (Fig. 11.9 A, B). Our data supports the assumption that the cytoplasmic bars and the basal lamina-like structure were a two level apparatus for the ultrafiltration. Similar to the observations made for *B. glabrata* rhogocytes (see Fig. 10.7), we observed a highly dense material located at the cytoplasmic bars at the insertion side of the slits (Fig. 11.9, see also Fig. 11.5).

For further 3D reconstructions of *L. stagnalis* rhogocytes see Part VI.

In order to check whether the protein arrays showed crystallinity, we collected

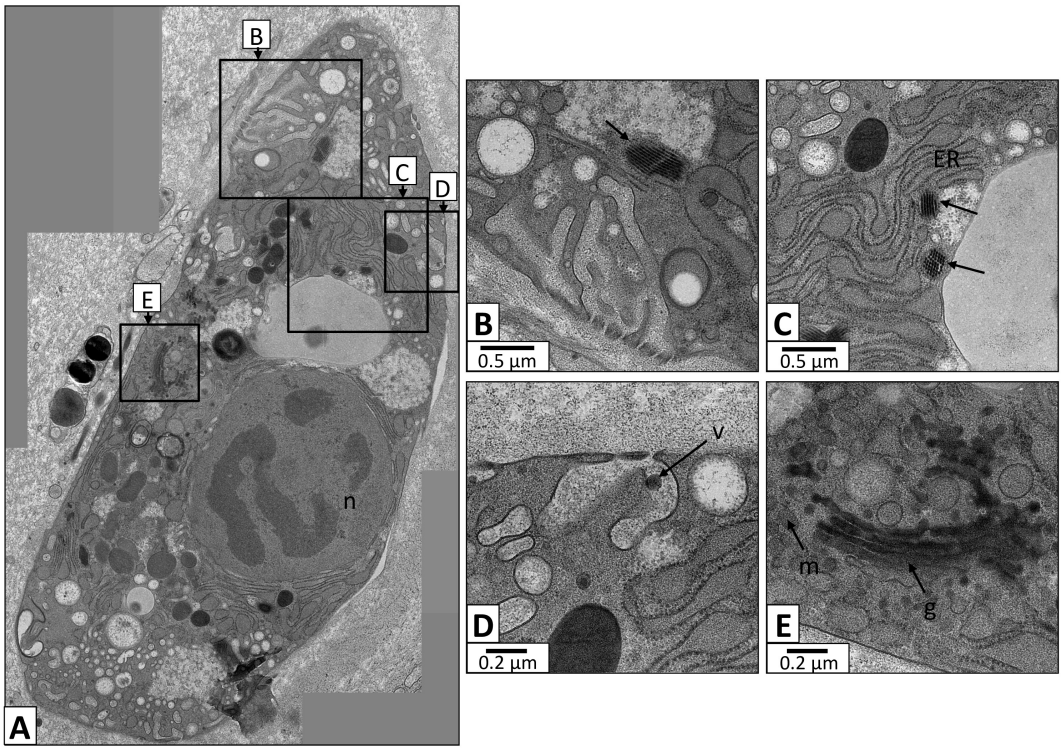

Figure 11.8. ***Electron microscopy of L. stagnalis mantle tissue sections fixed by high pressure freezing and freeze substitution.*** *(A) Rhogocyte with a big nucleus (n). (B) Area seen in (A) including a vacuole filled with pseudo-crystalline arrays (arrow) and the invaginations of plasma membrane bridged by cytoplasmic bars. (C) Area presented in (A) with vacuoles filled with pseudo-crystalline arrays (arrows). The area is enriched with ER. (D) Area seen in (A) pointing out a vesicle (→v) inside the invagination of plasma membrane. (E) Area indicated in (A) showing a Golgi apparatus (g, arrow) with numerous vesicles and mitochondria (→m).*

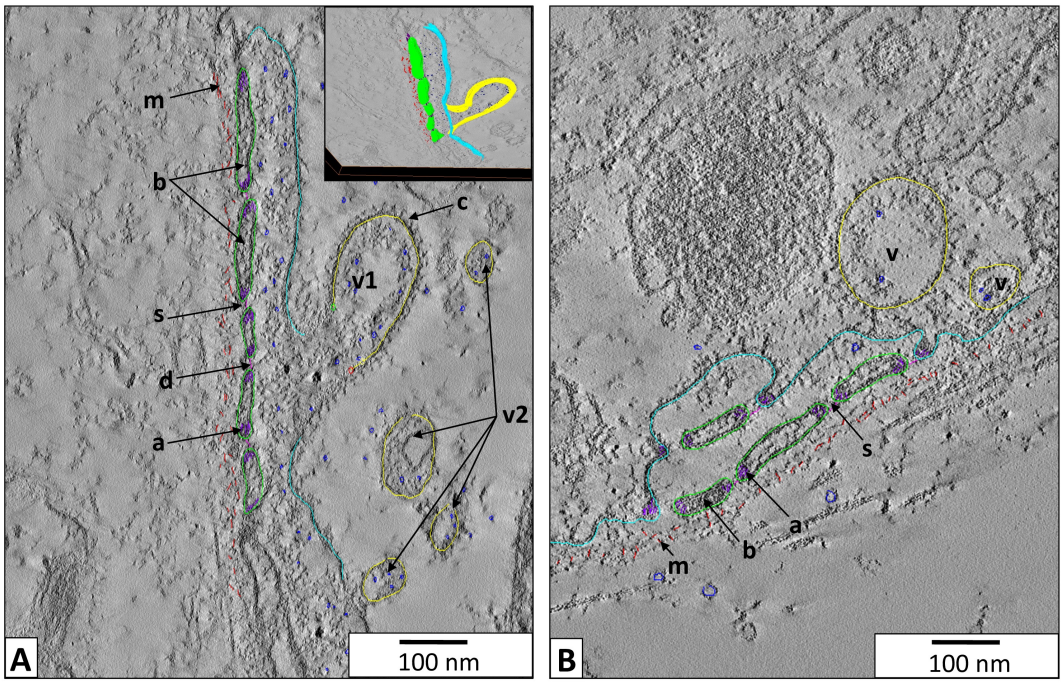

Figure 11.9. ***3D ultrastructure of a rhogocyte region with slit apparatus.*** *(A) Electron tomogram slice of mantle tissue of L. stagnalis, with its corresponding 3D model overlayed, calculated in IMOD. Invagination of coated plasma mebrane (→c, light blue) is bridged by cytoplasmic bars (→b, green) that form slits (→s, pink). Highly dense material (→a, purple) is observed at the cytoplasmic bars, at the insertion side of the slits. It is likely to contain actin bundles. A vesicle (→v, yellow) with granular context (blue) is connected to the extracellular pocket. The basal lamina-like envelope (→m, red) provides an additional filtration barrier. The insert shows the segmentation of the same tomogram performed in Amira. (B) Tomogram slice of a 3D- reconstruction with its corresponding 3D model overlayed, performed in IMOD. The basal lamina like membrane (→m, red) surrounds the rhogocyte. Its filtration apparatus further consists of the slits (→s, pink) that connect the cytoplasmic bars (→b, green) which bridge the invaginations of coated plasma membrane (light blue). There is a highly dense material at the cytoplasmic bars at the insertion sides of the slits, that is likely to contain actin bundles (→a, purple). Note the vesicles (v, yellow) found next to the invaginations, probably transporting the granular context (blue) found inside the extracellular lacuna and the neighboring cytoplasm.*

the diffraction patterns of these structures while using the EM in STEM mode (Fig. 11.10). However, due to the sample preparation and radiation damage of the crystals, we could not obtain any diffraction patterns.

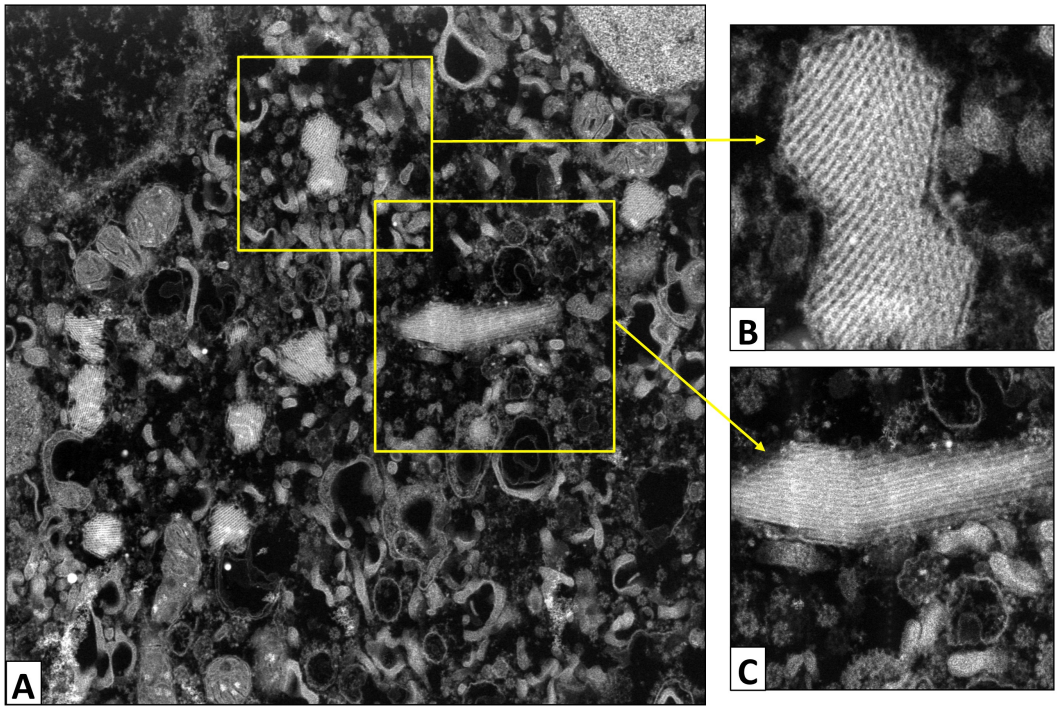

Figure 11.10. ***Observation of pseudo-crystalline arrays with STEM.*** *(A) Area of a rhogocyte filled with pseudo-crystalline arrays of proteins presented in the yellow boxes. (B) Pseudo-crystalline arrays presented in (A) in top view. (C) Pseudo-crystalline arrays presented in (B) in side view.*

11.4. Immunogold localization of actin

Using the monoclonal anti-actin primary antibody (Lessard, 1998), already applied to *B. glabrata* tissues (see Fig. 10.10), we could demonstrate by immunogold labeling experiments that actin is a major component in the slit apparatus of rhogocytes. The major localization was at the edges of the cytoplasmic bars, at the insertion side of the slits (Fig. 11.11), where a highly dense material is visible in the electron microscope (see Fig. 11.5 & 11.9).

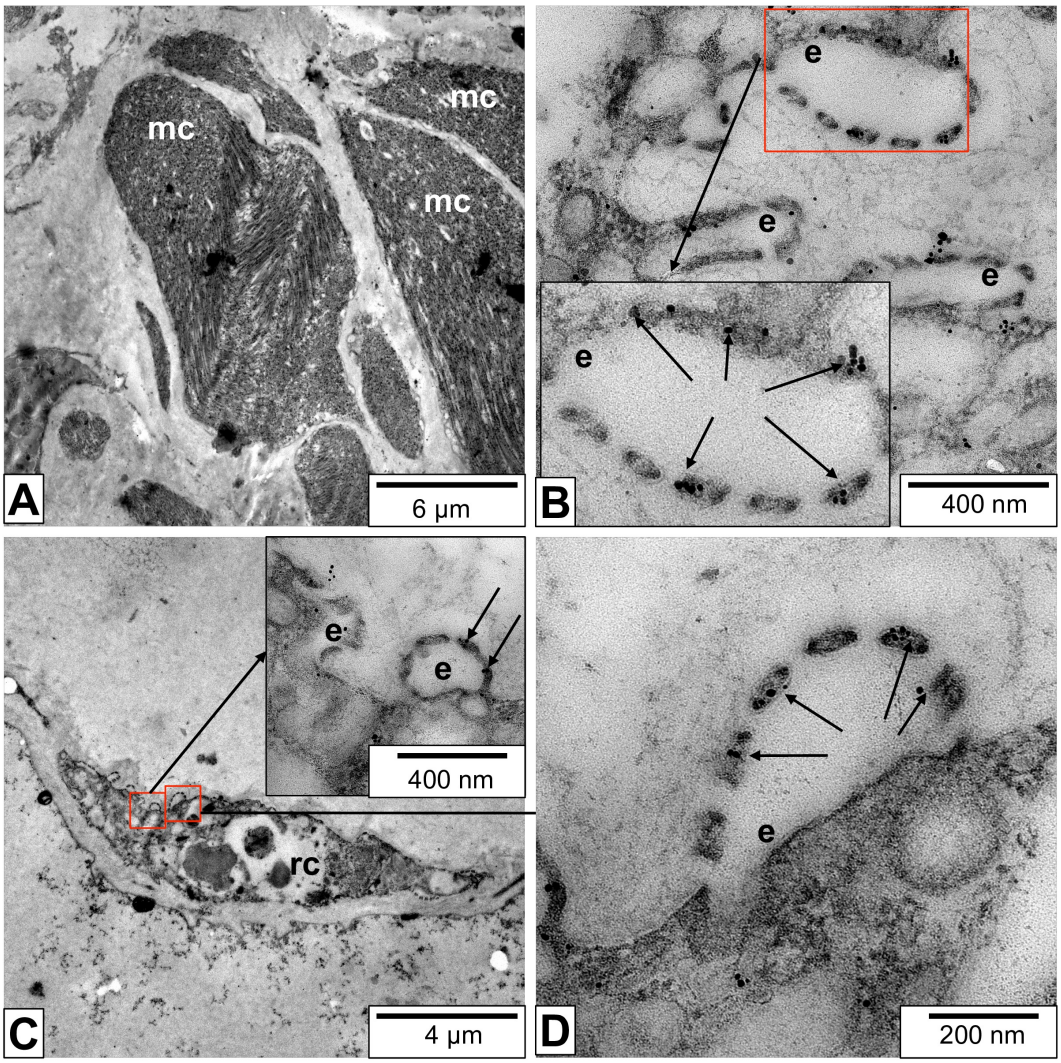

Figure 11.11. ***Immunogold localization of actin in the slit apparatus.*** *(A-D) TEM image of LR-white embedded mantle tissue of L. stagnalis. (A) A group of muscle cells (mc) labeled with the anti-actin antibodies. (B) Extracellular lacunae of a rhogocyte. Note the enlarged area, showing the immunogold labeling (arrows) at the edges of the cytoplasmic bars. (C) Overview of a rhogocyte in a mantle tissue section labeled with immungold particles against actin. Note the extracellular lacunae enlarged in the box, showing the immunogold labeling (arrows). (D) Close-up view of the region in (C), showing the localization of antibodies at the cytolasmic bars at the insertion side of the slits (arrows).*

11.5. Immunolocalization of nephrin

Polyclonal anti-nephrin antibodies were used on cryo sections of *L. stagnalis* tissues. Immunofluorescence microscopy showed strong labeling of cells (localized in their periphery) morphologically identified as rhogocytes (Fig. 11.12). This indicates the presence of this protein in the slit apparatus.

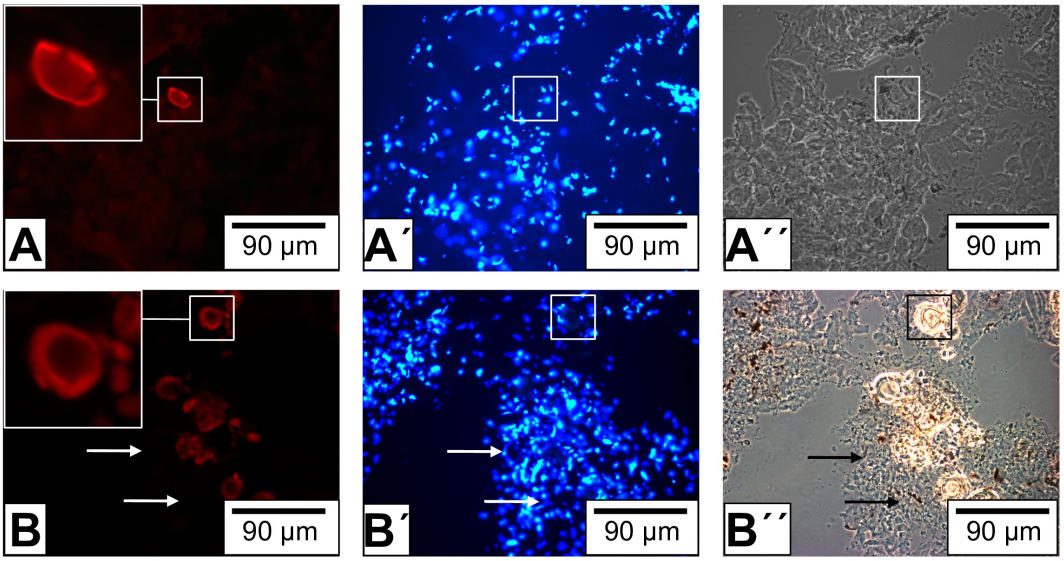

Figure 11.12. ***Immunofluorescence microscopy of mantle frozen tissue sections with anti-nephrin antibodies.*** *(A, B) Epifluorescence optics of a cluster of rhogocytes, showing a positive reaction (red signal) with anti-nephrin antibodies. Two rhogocytes are highlighted in the white boxes and two more with arrows. (A', B') The same sections showing DAPI (diamidino-2-phenylindole) staining. (A", B") The same sections with phase contrast optics.*

11.6. Response of rhogocytes to deprivation of food and cadmium stress

After deprivation of food for 96 h, individuals of *L. stagnalis* were fixed and the connective tissue was studied using TEM. The rhogocytes showed much less invaginations and cytoplasmic bars (Fig. 11.13 A, D) compared to the control. The endoplasmic reticulum was still the most prominent structure (Fig. 11.13 B). A high number of vesicles filled with the 25 nm rings interpreted as hemocyanin top views were observed. In addition, the elongated cylinders interpreted as stacks of hemocyanin molecules were seen (Fig. 11.13 C, E, F, arrows). Analyzing the

hemolymph of starved animals revealed a comparatively high amount of hemocyanin (Fig. 11.14).

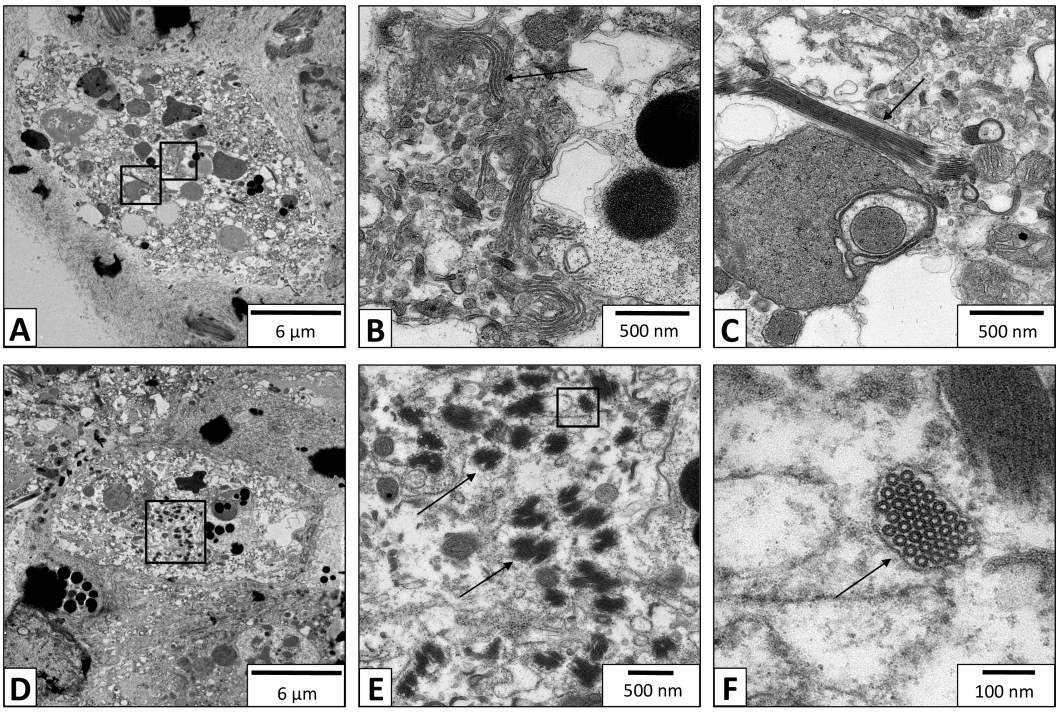

Figure 11.13. ***Response of rhogocytes to deprivation of food.*** *(A-F) TEM images of chemically fixed mantle tissue of L. stagnalis that deprived of food. (A) Rhogocyte from an animal deprived of food for 96 h in darkness, full of ER and pseudo-crystalline arrays. The rectangles indicate areas seen in (B) and (C). (B) ER seen in (A). (C) Pseudo-crystalline structure seen in (A). (D) Rhogocyte from an individual starved for 96 h in dark. Note the increased number of vacuoles filled with pseudo-crystalline arrays. The rectangle indicates the area seen in (E). (E) A large number of pseudo-crystalline structures (arrows). The rectangle indicates the area seen in (F). (F) Top view of pseudo-crystalline arrays, seen in (D-E).*

Relatively small rhogocytes were seen in the animals that survived for 96 h in water contaminated with 0.05-0.1 mg/l cadmium chloride (Fig. 11.15 A, B, D, E). They appeared mainly in groups and contain an unusual large number of electron dense granula (Fig. 11.15 C, arrows) and mitochondria (Fig. 11.15 C, arrows). Using the module 'e2boxer' of the EMAN2 software package, the increase of electron dense granula could be quantified and thereby confirmed (Table 11.1). This suggests that the number of rhogocytes is increased by cell division and that a material (most probably cadmium chloride) is deposited in the granula. We attempted to prove this by EDX-TEM. This analysis showed that a weak cadmium signal was observed both inside the granula as well as in the surrounding tissue (Fig. 11.16). Therefore, the presence of cadmium specifically in the granula could not be confirmed. Either

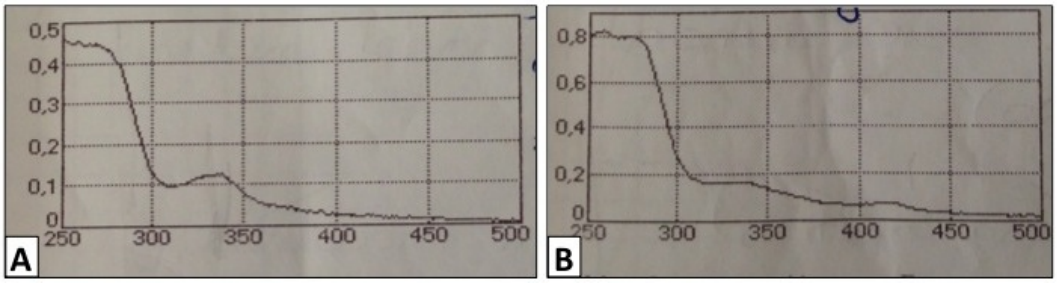

Figure 11.14. ***UV-spectrum of hemolymph samples of L. stagnalis.*** *(A) Unstarved control animal. (B) Animal after deprivation of food for 96h (in darkness). The higher optical density in (B) suggests a significantly higher hemocyanin concentration.*

there was no such process, or more likely, the cadmium was equally distributed over the section during the fixation and sectioning process. It is very likely that the whole fixation routine has to be optimized to prove that cadmium is concentrated inside the granula.

As another major change, we observed that compared to the controls, these rhogocytes exhibited much more extracellular pockets covered by slit-forming cytoplasmic bars (Fig. 11.15 D, E, arrows). In other words, it appears that the surface covered by slits was significantly increased. This strongly suggests an uptake of the cadmium chloride by ultrafiltration through the molecular sieve constituted by the slit diaphragm.

Table 11.1. ***Number of electron-dense granula in individual rhogocytes from untreated and $CdCl_2$-contaminated animals (L. stagnalis).***

untreated			contaminated		
4	2	2	8	15	16
3	4	4	11	8	28
4	3	0	7	16	8
4	2	8	7	11	9
0	1	1	9	19	28
$\varnothing = 2.8$			$\varnothing = 13.3$		

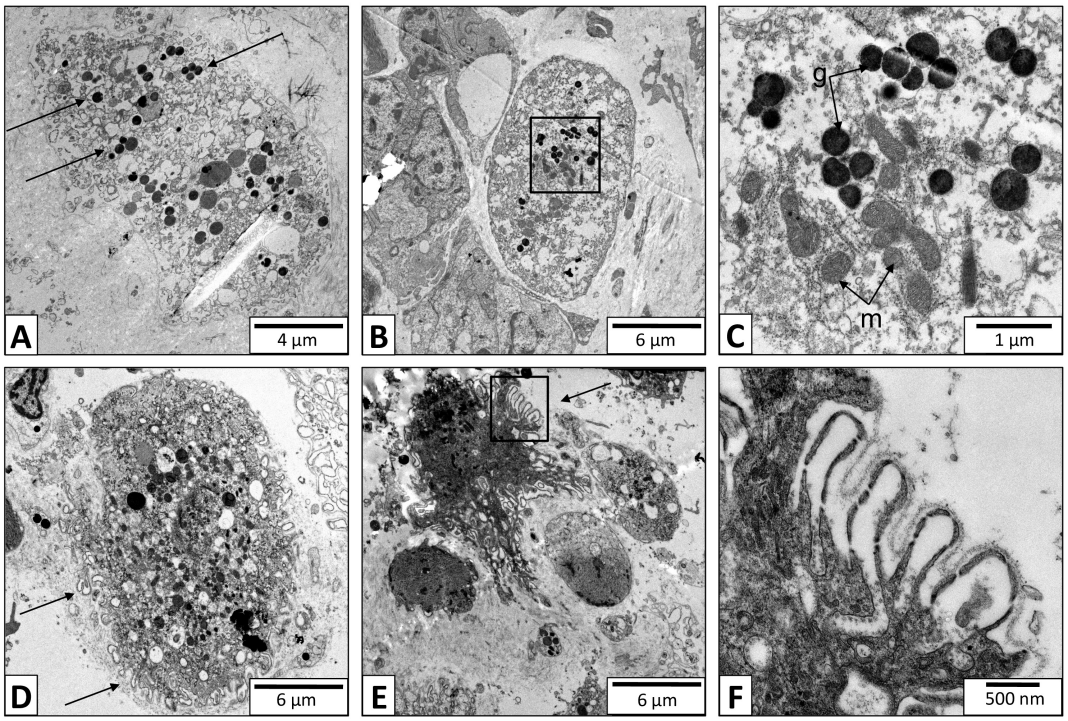

Figure 11.15. ***Response of rhogocytes to cadmium stress.*** *(A-F) TEM images of chemically fixed mantle tissue of cadmium stressed individuals of L. stagnalis. (A) Rhogocyte of a cadmium-contaminated animal (48 h, 0.05 mg/l of $CdCl_2$) enriched with electron dense granula (arrows). (B) Rhogocyte in a cadmium-contaminated animal (48 h, 0.05 mg/l of $CdCl_2$). The rectangle indicates the area seen in (C). (C) Lots of electron dense granula (g, arrows) and mitochondria (m, arrows) seen in (B). (D) Rhogocyte of a cadmium-contaminated animal (96 h, 0.1 mg/l of $CdCl_2$) with many invaginations and cytoplasmic bars (arrows). (E) Rhogocyte of a cadmium-contaminated animal (96 h, 0.1 mg/l of $CdCl_2$). Note the enlarged filtration cell surface. The rectangle indicates the area seen in (F). (F) An invagination seen in (E) indicating the enlarged surface covered with the slits.*

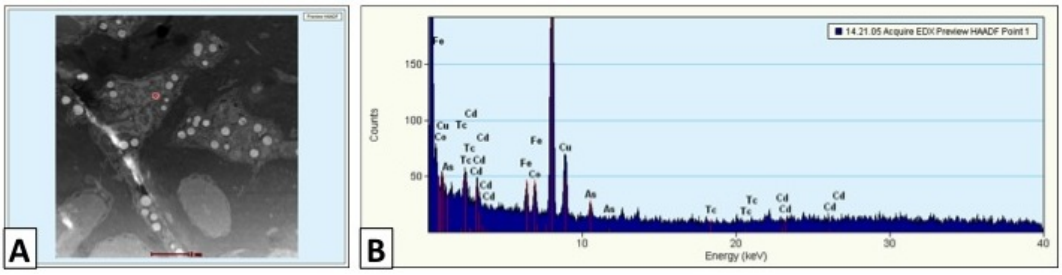

Figure 11.16. ***Distribution of cadmium inside the rhogocytes.*** *(A) STEM image indicating the electron dense granula inside the rhogocyte of L. stagnalis. (B) EDX spectrum of the electron dense granula in the rhogocyte of L. stagnalis presented in (A), which shows its elemental composition. Only the peaks for Fe and Cu are significant, but there is an indication that cadmium is present as well.*

Part IV.

Discussion

12. The rhogocytes of gastropods

In most studies on molluscan rhogocytes, emphasis is given to the extracellular lacunae, invaginations of plasma membrane, bridged by cytoplasmic bars. The slits between the cytoplasmic bars are approx. 20 nm and bridged by thin diaphragms (for review, see Haszprunar, 1996).

We found rhogocytes in the examined mantle and foot tissues of *B. glabrata* and *L. stagnalis* throughout the primary body cavity, either free in the hemolymph or embedded in the connective tissue between muscle cells, secretory cells and granular cells (Fig. 10.1, 10.4, 11.1 & 11.4). Their abundance was highest in the mantle tissue. This fits the results of Boer & Sminia (1976) on *L. stagnalis* who examined further the heart and kidney, where they found more rhogocytes. Often, they appear in groups. Their size varies and can reach up to 30 nm in diameter. The observed freshwater snail rhogocytes showed the same morphology as has been documented in vetigastropods, other gastropod taxa and molluscs in general (Haszprunar, 1996; Albrecht et al., 2001; Martin et al., 2011; Sminia & Boer, 1973; Skelding & Newell, 1975; Sminia, 1977; Jones & Bowen, 1979; Marigomez et al., 1990; Zaroogian & Anderson, 1995; Giamberini & Pihan, 1996; Zaroogian & Norwood, 2002; Prince & Johnson, 2006). Such rhogocytes also occur in non-feeding developmental stages of a direct developing gastropod (Fioroni et al., 1984).

Stewart et al. (2014) observed for the first time rhogocytes in gastropod larvae, on both sides of the foregut. They documented the transformation that takes place in four stages from protonephridial terminal cells into rhogocytes. A possible connection between rhogocytes and protonephridia was earlier proposed by Rivest (1992) and Ruppert (1994).

Furthermore, Stewart et al. (2014) identified some differences between adult and larval rhogocytes, such as the presence of stacked sieve complexes that probably increase selectivity and the presence of coated vesicles associated with the extracellular lacunae. In contrast to that, Haszprunar (1996) concluded that such coated vesicles are rare. This structure is controversial, as Prince & Johnson (2006) observed numerous coated vesicles associated with such lacunae of rhogocyte-like cells within the ink gland of adult sea hares *Aplysia californica*. In the present study, coated vesicles in the vicinity of the extracellular lacunae were often observed.

13. Synthesis of hemoglobin and hemocyanin

There is a variation in the location of hemocyanin synthesis among the gastropods. In the opisthobranch *Archidoris pseudoargus*, Schmekel & Weischer (1973) found hemocyanin in the blood gland cells located dorsally of the cerebropleural and pedal ganglia. In the vetigastropod *Concholepas concholepas*, cells of the hepatopancreas have been proposed (Manubens et al., 2010). In the following species, rhogocytes are suggested to synthesize hemocyanin: in the pulmonates *L. stagnalis* (Sminia et al., 1972; Sminia & Boer, 1973), *Helix aspersa* (Sminia & Vlugt-van Daalen, 1977), *Deroceras reticulatum* (Jones & Bowen, 1979) and *Arion hortensis* (Skelding & Newell, 1975), and in the vertigastropods *Haliotis tuberculata* (Albrecht et al., 2001) and *Megathura crenulata* (Miller & van Holde, 1982; Martin et al., 2011).

In our experiments, antibodies against hemoglobin and hemocyanin have been used on paraffin sections of *B. glabrata* and *L. stagnalis*, which identified these proteins inside rhogocytes (Fig. 10.3 & 11.3). In case of *L. stagnalis*, hemocyanin is electron microscopically observed, also directed in rhogocytes and in the hemolymph spaces on ultrathin sections. It should be mentioned that it seems to be a higher concentration of hemocyanin around the muscle cells (Fig. 11.6). This fits a high demand of oxygen around these muscle cells, an observation that has been discussed, for spider leg muscles, by Paul et al. (1991). They collected evidence using histochemical and immunofluorescence techniques that the hemolymph flow in an open circulatory system is well adapted to cellular oxygen demands.

Of course the presence of the respiratory protein alone is not a proof for its synthesis by the cell, which could as well serve as a compartment of storage or breakdown and recycling of hemoglobin and hemocyanin. It should be mentioned though that the abundance of RER and Golgi complexes within the rhogocytes is consistent with a high rate of protein synthesis (Plummer, 1966; Sminia, 1972). To prove this, *in situ* hybridization has been used. In the case of *H. tuberculata* and *M. crenulata*, hemocyanin expression in rhogocytes was already demonstrated (Albrecht et al., 2001; Martin et al., 2011). In the present study, the early hypothesis of Sminia et al. (1972) that in planorbid snails also the hemoglobin is synthesized by rhogocytes, was confirmed in this thesis for both hemoglobin isoforms (see Fig. 10.3; for structural details on this hemoglobin, see Fig. 4.1 and Lieb et al., 2006). Not all rhogocytes were labeled, indicating that not all rhogocytes produce this protein simultaneously, or because the mRNA is a transient product, and it was probably degraded in some of the rhogocytes at the time of the experiment. Comparable results were obtained in the case of *L. stagnalis* hemocyanin (Fig. 11.3). Whole

mount *in situ* hybridization identified the mantle tissue as the main body region where hemocyanin, respectively hemoglobin, is synthesized.

In contrast to these observations in the vetigastropoda and pulmonata, the sites of hemocyanin synthesis in cephalopods are the branchial gland (Dilly & Messenger, 1972; Schipp et al., 1973; Muzii, 1981) and the midgut gland (Ruth et al., 1988; Ruth, 1993). In the case of the sea hare *Aplysia*, and opisthobranch gastropod, the blood gland is discussed as the site of hemocyanin synthesis (Schmekel & Weischer, 1973).

In the arthropod subphylum *Chelicerata*, hemocyanin is synthesized in specific hemolymph cells called cyanocytes, where it is stored in a pseudo-crystalline form in the cytosol and later released through holocrine secretion. Fahrenbach (1970) identified this protein in the cyanocytes from the horseshoe crab *Limulus polyphemus* and these results are further substantiated by Wood & Bonaventura (1981) and confirmed by *in situ* hybridization in a tarantula by Markl et al., (1990). This fits the observation that chelicerate hemocyanins are not glycosylated, in contrast to crystacean and molluscan hemocyanins (Markl & Decker, 1992). In crustaceans, the hemocyanin is synthesized in midgut gland cells, and glycosylated (see ref. in Markl et al., 1990).

The respiratory proteins hemoglobin and hemocyanin are unrelated phylogenetically. Whereas molluscan hemocyanin evolved already in the late Precambrian (Lieb et al., 2001), planorbid hemoglobin is much younger phylogenetically. According to molecular trees it evolved from planorbid myoglobin (Lieb et al., 2006) that is predominately expressed in radula muscle cells (Weber & Vinogradow, 2001). The reason why the site of biosynthesis of hemoglobin is not muscle cells but rhogocytes might be connected with the body distribution, exocytosis pathway via slit apparatus and other features provided by the rhogocyte. In this context it should be mentioned that in gastropods, both proteins are composed of large multimeric polypeptide subunits, namely 300-550 kDa in molluscan hemocyanin (Markl, 2013; Gatsogiannis & Markl, 2009) and 240 kDa in *B. glabrata* hemoglobin (Lieb et al., 2006). Six to twelve functional units in the case of molluscan hemocyanin and 13 in *B. glabrata* hemoglobin, each with a single active site, are concatenated like a pearl chain via peptide linkers. It appears that the rhogocyte provides a unique cellular machinery for synthesizing such exceptionally large polypeptides.

Co-existence of hemoglobin and hemocyanin as observed in *B. glabrata* is unusual and has been reported only in the amphipod *Cyamus scammoni*, in the phylum Arthropoda (Terwilliger & Ryan, 2006). Because of the higher oxygen affinity of hemoglobin, planorbids have a more efficient physiological exploitation of the pulmonary O_2 store, resulting in an increased diving potential, compared to lymneids that live in the same habitats (Bugge & Weber, 1999). Our TEM studies demonstrate the presence of hemocyanin, either as individual molecules or as highly ordered pseudo-crystalline arrays, in the ER in parallel strands and in cisternae as

also discussed previously (Sminia & Boer, 1973; Sminia & Vlugt-van Daalen, 1977; Skelding & Newell, 1975; Albrecht et al., 2001). It also occurs inside the invaginations of plasma membrane.

It should be mentioned though, that the pseudo-crystalline arrays of *L. stagnalis* hemocyanin appear to have in top view a much smaller size than the ones seen in *B. glabrata* (25 nm versus 50 nm). The reason of this discrepancy is unclear, but we discuss two explanations: (i) the structures seen in *B. glabrata* are not hemocyanin, and (ii) it has something to do with the profound structural difference between a hemocyanin didecamer as expressed in *L. stagnalis*, and a collarless hemocyanin decamer as found in *B. glabrata* (for structural details, see Markl, 2013). Views of hemocyanin molecules inside *L. stagnalis* rhogocytes have a diameter of approx. 25 nm, which speaks against the 35 nm diameter of negatively stained hemocyanin didecamers purified from *L. stagnalis* hemolymph (Fig. 11.6); the latter diameter has been confirmed by 3D-cryoelectron microscopy (Gatsogiannis & Markl, 2009). We assume that the difference in diameter is due to the differences in chemical fixation and staining. The use of chemicals and heavy metals during this procedure might cause alterations in the electron microscopical appearance of these proteins.

14. Up regulation of hemocyanin synthesis during stress conditions

Hemocyanin is expressed in *B. glabrata* only as a trace component and therefore it is certainly not necessary for oxygen transport (Lieb et al., 2006). Instead, it might be expressed for its presumed prophenoloxidase/tyrosinase activity (Decker & Tuczek, 2000). In any case it should be biologically necessary, as it is up-regulated under stress conditions in our starvation experiments (Fig. 10.12). An up-regulation of hemolymph proteins, including a prophenoloxidase, was observed by Handke (2013) during starvation of *Drosophila larvae*. Independent experiments are needed to confirm this in *B. glabrata* and to prove that the 50 nm rings in *B. glabrata* rhogocytes are indeed hemocyanin. But provided the truncated hemocyanin molecules of *B. glabrata* are synthesized in rhogocytes, the 50 nm rings are the only visible candidates in our EM micrographs.

15. Passage through the slit apparatus

The existence of a sieve complex with cytoplasmic bars and diaphragms has led to the hypothesis that rhogocytes play a basic role in ultrafiltration (Boer & Sminia, 1976; Haszprunar, 1996). It has been documented that they take up small molecules and particles such as ferritin (Sminia, 1972; Wolburg-Buchholz, 1972a; Skelding & Newell, 1975; Rivest, 1992), radioactive iodine-labelled hemocyanin (Beuerlein et al., 2002b), colloidal gold (Beuerlein et al., 2002a) and trypan blue (Sminia, 1972), through endocytosis (Skelding and Newell, 1975; Boer & Sminia, 1976). Sminia (1972) and Skelding & Newell (1975) suggested that the external basement membrane contributes to the selectivity of substances by limiting the passage of larger ones, as it has been documented in the case of cyrtocytes of protonephridia and podocytes of metanephridia (Ruppert & Smith, 1988; Smith & Ruppert, 1988). Experimentally excluded from this passage are the following substances: ink particles (Sminia, 1972), larger than 15 nm colloidal gold particles (Skelding & Newell, 1975), *Pseudomonas sp. bacteria* (Beuerlein et al., 2002a), 110 nm latex granules and yeast cells (Haszprunar, 1996).

The question is, what happens at the slit apparatus to enable exocytosis of proteins and endocytosis of small molecules? The vesicles might follow the 'kiss and run' mechanism, as described by Schneider (2001). In our case, the vesicle could release the proteins to the extracellular lacunae, and then the same vesicle could undergo endocytosis with material that is present in the lacunae. During such a process, the integrity and balance of the membrane is not disrupted. The released proteins could follow the diffusion gradient outwards through the slits into the hemolymph whereas material from the hemolymph could diffuse in the opposite direction.

However, the presence of vesicles in different regions of the slit apparatus supports an alternative hypothesis that is illustrated in Fig. 15.1. After their synthesis in the ER, the vesicle-confined respiratory proteins have to be secreted into the hemolymph by exocytosis. In many secretory cell types, uncoated secretory vesicles fuse with any region of the plasma membrane. In rhogocytes we found that they are fused only with regions of the extracellular lacunae, and often contain protein-like particles. They are found either inside the extracellular lacunae, or fused with the slits, or between the slits and the surrounding basement membrane, or sometimes even outside of the latter. This indicates exocytotic activity through uncoated vesicles. Furthermore, only the bordering of the lacunae is covered by a clathrin coat, and coated vesicles are frequently observed in rhogocytes (see Fig. 11.9 and Haszprunar, 1996; Albrecht et al., 2001; Boer, 1976). Coated vesicles can be part of exocytosis as well (Helmy, 1986; Segawa, 1998; Zampighi et al., 1999), although

rare in comparison with endocytosis. It therefore appears that rhogocytes simultaneously perform exocytosis via uncoated vesicles and endocytosis via coated vesicles (see Fig. 15.1).

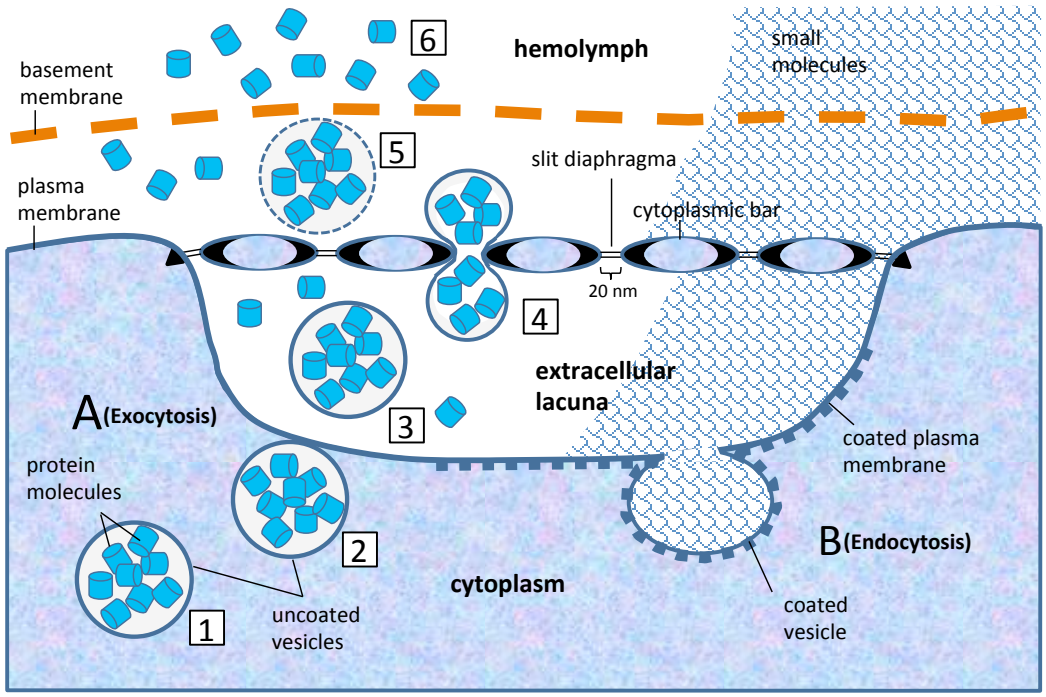

Figure 15.1. ***Hypothesis of the passage of particles through the slit apparatus.*** *(A) Exocytosis: (1) Transfer of newly synthesized respiratory proteins in uncoated vesicles to the plasma membrane. (2) Close contact between, and apparent fusion of, uncoated vesicle and plasma membrane. (3) Presence of protein-containing uncoated vesicles within the extracellular lacuna, suggesting that these vesicles do not fuse with the plasma membrane, but somehow pass through it. Images of 'budding' vesicles are lacking, and therefore, this step remains unclear. (4) Passage of vesicle through an enlarged slit. We assume that contact of the vesicle with the diaphragmatic slit somehow causes actin-driven constriction of the adjacent cytoplasmic bars, thereby enlarging the slit to allow passage of vesicle. (5) Protein-containing vesicles between slit apparatus and basement membrane, and breakdown of the vesicle membrane. (6) Release of the protein molecules into the hemolymph. The slit diaphragm blocks their diffusion back into the extracellular lacuna. (B) Endocytosis: Small particles in the hemolymph diffuse freely through the diaphragmatic slits into the extracellular lacuna and are engulfed by the coated plasma membrane, forming endocytotic coated vesicles. (Graphic: J. Markl)*

The diaphragm that bridges this slit has a tooth-like structure (Boer & Sminia, 1976). The 'teeth' from the opposite sides of the slit contact each other via a bridging material. The teeth of the same row are 20 nm apart, and the slit width is also 20 nm. That means that the diaphragm has holes of 20 x 20 nm, much larger

than the 15 x 4 nm slits observed in the mammalian podocyte (Wartiovaara et al., 2004). The latter have to prevent the passage of serum albumin, 8 x 8 x 3 nm in size. In the case of the slits of rhogocytes, they might prevent the passage of hemolymph proteins larger than 20 nm. That means that in the case of *L. stagnalis*, the 35 nm hemocyanin didecamers are excluded from the passage, and in the case of *B. glabrata*, the 25 nm hemoglobin and the 25 nm acetylcholine-binding protein particles are also excluded. In this context it should be mentioned that the slit diameter in *B. glabrata* has not been accurately measured so far. It could be somewhat smaller than in 'hemocyanin snails'.

This means that the molecular sieve has the right size to block the inward migration of the hemolymph proteins, without providing a diffusion barrier for smaller particles. These particles, like heavy metal ions, are able to pass freely through the slits by diffusion. This could explain the increased number of electron dense granula that we find inside the rhogocytes after a cadmium contamination (Fig. 10.12 & 11.15, Table 10.1). Presumably, the cadmium ions pass through the slits to accumulate in the rhogocytes. This is enabled by the observed increase of the overall filtration surface and is a further evidence for the role of rhogocytes in detoxification, proposed by Marigomez et al. (2002), Marigomez et al. (1990) and Nott et al. (1993).

Albrecht et al. (2001) showed an image in which an ER cisterna is in direct contact with the extracellular lacuna of the slit apparatus. This might suggest that protein molecules travel directly to the extracellular lacunae and there is no need for uncoated vesicles for exocytosis. This is controversial to what has been described by other authors, and is rarely observed during the present work. It is therefore unlikely that it represents the primary exocytosis pathway for the respiratory proteins.

As discussed above the slit apparatus should exclude the passage of large proteins. In order to export these molecules, there should be a gating mechanism that enlarges the slits. Under the electron microscope there is a highly dense material that is observed at the edges of the cytoplasmic bars, at the insertion sides of the slits. One of the components of this material is actin (see Fig. 10.10 & 11.11). Our speculation is that there is a chemical signal causing the actin bundles to interact with motor proteins, thereby changing the size of the holes of the sieve. Since whole vesicles seem to pass through (see Fig. 10.8), it may well be that the opening signal is anchored to the vesicle membrane. Changes in shape and size of the pores are also proposed for the podocyte slit diaphragm (Wartiovaara et al., 2004). Filtration pressure is probably caused by endocytosis in rhogocytes and by muscular activity in podocytes (Morse & Cooer, 1993; Haszprunar, 1996). Although this secretion mechanism of exocytosis is discussed here and also in many other cases (Skelding & Newell, 1975; Sminia, 1977), there are observations of holocrine and merocrine secretion in cephalopods (Ruth et al., 1988; Dilly & Messenger, 1972; Schipp et al.,

1973). Further studies are needed to establish the exact mechanism of the secretion of the respiratory proteins.

In biochemical studies of podocytes and nephrocytes, nephrin is one of the proteins composing the slit diaphragm (reviewed by Patrakka, 2007). Nephrin is a member of the immunoglobulin superfamily and belongs to the cell adhesion molecules (Brummendorf, 1994). It is a transmembrane protein that is necessary for the proper functioning of the renal filtration barrier. Nephrin forms homo- and heterodimers with a second protein, neph-1; together they transduce actin polymerization (Garg, 2007) and form the molecular sieve (Zhuang et al., 2009; Weavers et al., 2009; Kestilä et al., 1998). *Drosophila* orthologs of nephrin and neph-1 are termed sns and kirre. They are co-expressed in nephrocytes that contribute to detoxification of insect hemolymph by uptake of molecules through the nephrocyte slit diaphragm. The latter discriminates particles of different sizes in that larger molecules are taken up significantly slower than smaller molecules (Zhuang et al., 2009).

In support of the present study, nephrin was identified in *B. glabrata* by our group, and the complete primary structure is provided (results presented in Kokkinopoulou et al., 2014). We found that all important features known from human nephrin (Kestilä et al., 1998) are conserved. Furthermore, *B. glabrata* and *L. stagnalis* rhogocytes showed a positive reaction to anti-nephrin antibodies in the cell periphery (Figs. 10.11 & 11.12). Encompassing nine extracellular domains with a total length of approx. 35 nm, nephrin would allow stretching of the slits and enlargement of the pore size.

16. Possible homology between rhogocytes and other cell types

The extracellular basal lamina structure that surrounds the rhogocyte, its cytoplasmic bars with the diaphragmatic slits and the fenestration of the diaphragms suggest a common phylogenetic basis between rhogocytes, podocytes and nephrocytes (Haszprunar, 1996; Weavers et al., 2009; and present study). The structure of the proteins in podocytes and nephrocytes has been studied in detail (Zhuang et al., 2009; Weavers et al., 2009; Kestilä et al., 1998).

As discussed above, we localized actin in the slit apparatus. Therefore, it should play a role in the filtration through the rhogocyte slits as it does in podocytes and nephrocytes (Weavers et al., 2009; Ichimura et al., 2003). The discovery and localization of actin and nephrin that is performed in this work is an additional molecular argument in favor of the hypothesis reviewed by Haszprunar (1996), that rhogocytes, podocytes and nephrocytes are related. This links the rhogocytes to the metanephridial systems.

Haszprunar (1996) additionally pointed out that also cyrtocytes might belong to this group of cell types. Cyrtocytes are the terminal cells of protonephridia. They are responsible for ultrafiltration of extracellular body fluid during the process of excretion and osmoregulation in animals such as the Plathelminthes that are Bilateria but lack a blood vascular system (Ruppert & Smith, 1988). Podocytes, on the other hand, are ultrafiltration cells in *Bilateria* possessing a blood vascular system (Ruppert & Smith, 1988). However, due to fundamental structural differences, a homology between cyrtocytes and rhogocytes is not obvious.

Stewart et al. (2014) compared the sieve structures of rhogocytes and cyrtocytes in gastropod larvae (*Siphonaria denticulate*). Instead of several extracellular lacunae as in rhogocytes, cyrtocytes show a single large lacuna surrounding the flagellum bundle. Furthermore, rhogocytes are solitary cells (see also Sminia, 1972; Fioroni et al., 1984), whereas cyrtocytes are always associated with cells of the nephridioduct of the protonephridium (Ruppert & Smith, 1988; Smith & Ruppert, 1988).

Rieger & Tyler (1979) established criteria for homology in cellular ultrastructures. Their two main criteria are as follows: (i) similarity in physical and temporal location of the studied structures, (ii) the existence of structures with intermediate morphology. In the case of larval rhogocytes and protonephridial cyrtocytes, the first criterion is met but not the second (Stewart et al., 2014). However, a transformation from protonephridial terminal cells to rhogocytes during the ontogeny of a gastropod mollusc was documented which strongly suggests their homology

(Stewart et al., 2014). Thus, it appears that the rhogocyte has evolutionary and developmental links to both, metanephridial and protonephridial systems.

17. More functions of rhogocytes

Rhogocytes show acid phosphatase activity within their lysosomes, which could assist in breakdown of endocytosed molecules (Sminia, 1972; Jones & Bowen, 1979). Stewart et al. (2014) observed vesicles engulfed by electron dense vacuoles in the rhogocytes of *Amphissa columbiana* and *Marsenina stearnsii* (for similar observations see Fioroni et al., 1984). This could indicate storage or degeneration of material within the vacuole. That means that substances found inside the rhogocyte lacunae and vesicles can be waste products or material required for assembly of products.

In vacuoles and vesicles of rhogocytes, high concentrations of copper (Mason et al., 1984; Marigomez et al., 2002), iron and cadmium (Marigomez et al., 2002) have been monitored. The present responses of *B. glabrata* and *L. stagnalis* rhogocytes to cadmium contamination support previous ideas that these cells play a role in heavy metal accumulation (Marigomez et al., 2002; Marigomez et al., 1990; Nott, 1993). Their apparent reaction is cell division (deduced from the smaller size of cells) and formation of more extracellular lacunae with slits, both resulting in a significant increase of the overall filtration surface. The number of extracellular lacunae is increased with duration or grade of contamination. The number of electron dense granula is also increased. We assume that cadmium accumulates the rhogocytes, specifically in the electron dense granula, in order to remove it from the hemolymph. Furthermore, the number of mitochondria is increased during this stress period; probably due to the fact that the cells need more energy for detoxification.

Pulmonate gastropods are able to detoxify metals in intracellular structures, by having metallothionein to bind cadmium molecules (Streit, 1993). That means that they are sensitive and could be used as markers for environmental pollution. Coeurdassier et al. (2003) established protocols for developing tests in risk assessment for freshwater systems. Sullivan & Cheng (1975) used *B. glabrata* to check the stress responses of the uptake of heavy metals by studying the morphology of the epithelium and the underlying connective tissue. Dallinger et al. (1997) highlighted the role of rhogocytes in the regulation of copper in the snail *Helix pomatia*. Further discussion on biomarkers follows in the next chapter.

During deprivation of food for 96 h, the snails react to these stress conditions by showing more pseudo-crystalline hemocyanin arrays in their rhogocytes; mainly inside vacuoles. Similar structures were identified in the newt *Triturus viridescens* as microtubules (Gall, 1966). However, formation of such pseudo-crystals from purified hemocyanin was carefully studied in *M. crenulata* by Harris et al. (1992) and therefore we are sure that the pseudo-crystals seen in rhogocytes are hemocyanin.

We tried to prove that these structures show crystallinity, but due to the fixation and radiation damage of the pseudo-crystals, we did not succeed in obtaining any diffraction pattern (Fig. 11.10).

In caenogastropod larvae, hemocyanin molecules have not been detected (Stewart et al., 2014). This is not surprising as these tiny creatures may not need oxygen transport or storage proteins. On the other hand, the ultrastructure of these rhogocytes suggests protein synthesis activity. One candidate could be the prophenoloxidase, which is a copper-containing protein that has a common molecular ancestor with hemocyanin (van Holde et al., 2001). In the case of neritimorph larvae, Stewart et al. (2014) electron microscopically observed cylinders 25 nm in diameter that closely resemble the hemocyanin molecules and arrays documented in the present work.

It has been demonstrated that in terrestrial gastropods the rhogocytes are a site of glycogen storage (Kisker, 1923; Fernandez, 1966; Woudrak, 1969; Sminia et al., 1972; Bani et al., 1990; Haszprunar, 1996). Sminia (1972) identified only small amounts of glycogen in rhogocytes of the freshwater snail *L. stagnalis*. During this work, a decrease of electron dense granula was indicated after starvation. We assume that some of these granula contained glycogen, which is probably used up during this stress condition.

18. Bioaccumulation of cadmium and use of gastropods as bioindicators

The environmental pollution and the ways to reduce it has been one of the most important issues over the last decades. The concentration of carbon dioxide (CO_2) in the atmosphere has been dramatically increased. The impact on ocean chemistry, marine organisms and aquatic ecosystem created by CO_2 absorption from the atmosphere has been discussed (Parker et al., 2013). Molluscs provide important ecosystem services including habitat structure, food for benthic organisms and purification of water. Thus, the impact on the molluscs would cause serious consequences for global protein sources and aquatic ecosystems.

Cadmium is an extremely toxic element. In man, it can lead to critical effects on lung, kidney or bones. In mammals it can affect fertility. It can modify RNA and DNA metabolism by damaging the repair process. It is not highly harmful by itself, but as it modifies reactions of other chemical compounds, it can be a potential risk (Degraeve, 1981). Cadmium is not detoxified in the environment. The risk of human exposure is increasing. It is extensively used in modern industry and a world concern for human health.

Of great importance is that organisms have a large number of strategies to overcome the effects caused by chemical stress. This includes behavioral changes and biochemical changes (Walker et al., 2001). If the stress persists, it could have dramatic effects on the population number. These anti-stress responses start at the subcellular level and influence a variety of metabolic pathways. Moreover, these changes cause energetic costs, that were originally available for other vital processes, such as growth and reproduction. Lethality, age-related changes in resistance, alterations of the normal developmental changes in proteins, and alterations in specific transfer RNAs are some of the effects of cadmium on *Drosophila* (Jacobson et al., 1981).

In vertebrates, cadmium accumulates particularly in liver and kidney, where it is bound to metallothionein, a metal-binding protein (Degraeve, 1981). Metallothioneins are cytoplasmic, low molecular mass proteins (6-7 kDa), having high cysteine content (30 %), no aromatic acids and high metal content (6-11 % metal ions) (Ray, 1986). Metallothionein is expressed in response to the presence of cadmium and other trace elements as a protective detoxifying mechanism. In the case of the Japanese water flea *Moina macrocopa*, most of the accumulated cadmium was bound to a low molecular weight cadmium-binding protein (Yamamura et al., 1983). Such proteins are also discussed in the case of the blue crab *Callinectes sapidus* (Wiedow et al., 1981).

Many animals accumulate cadmium in intracellular electron-dense membrane-limited granules or vesicles (Ray, 1986). The vesicles trap heavy metals by a biomembrane, thereby isolating them from the other cell compartments. Such granules are involved not only in uptake but also in excretion of cadmium.

In the earthworm species *Dendrobaena rubida* and *Lumbricus rubellus*, cadmium is found in a more electron-lucent vesicular component, designated the 'cadmosome' (Morgan & Morris, 1982). This may correspond to a lysosome. Other metals such as calcium and zinc are found in the so-called chloragosomes. These authors studied the accumulation and detoxification of heavy metals within membrane-bound vesicles as a general phenomenon, but the precise mechanism was not analyzed. Some organisms deposit metals in different granules in the same cell, e.g. barnacles store copper and zinc in the midgut parenchyma cells of barnacles (Walker, 1977). In order to answer the questions regarding the accumulation of the heavy metals, atomic absorption spectrophotometry, radiography, TEM, SEM and statistics were used (Morgan & Morris, 1982).

The ability of aquatic molluscs to accumulate heavy metals is well documented (for review see Haszprunar, 1996). Thus, they efficiently monitor heavy metal contamination in marine and freshwater ecosystems. Cadmium is one of the rare elements in nature. It is found as a main compound or as impurity in other metals, such as zinc. Its use is increasing rapidly, as it is present in a range of technical products such as electroplating, pigments, batteries, plastics, TV tubes, solar cells, alloys, fungicides (Fishbein, 1981). Cadmium is recovered as a by-product from the smelting and refining of tin and zinc ores. There has been an increase in its deposition in atmospheric, aquatic and terrestrial environments. This is followed by an increase in the cadmium uptake by organisms via the food chain or the respiratory water. Ferard et al. (1981) and Hardy et al. (1984) studied an artificial phytoplankton-oyster-mouse food chain. They concluded that at high concentration of cadmium in the phytoplankton, the oysters are extremely efficient at concentrating the metal, but the overall transfer to mice is low. Nevertheless, cadmium is found in lots of foods and beverages: fish, meat, milk, eggs, cereals, vegetables.

Decrease in growth rate with increased metal concentration is observed for cadmium, zinc and copper, in the case of the three oyster *Crassostrea* species (Watling, 1982). Temperature, different types of organic ligands, chemical form of cadmium, metal interaction, body size (weight, length and age) and other environmental parameters such as salinity, pH, cadmium level of seawater and season play a role when determining cadmium toxicity to oyster (Hung 1982; Ray, 1986). In general, the factors affecting the bioconcentration of cadmium by aquatic animals are the following: the form in which the cadmium is present, environmental factors such as temperature and salinity, type of exposure, meaning the route of entry of the material either in water or in solid form, and the presence of synergistic and antagonistic effects (Taylor, 1981).

Even in unpolluted environments, snails have the ability to concentrate cadmium in their midgut gland (Dallinger et al., 1997). The observation that molluscs have this great ability to concentrate cadmium from the environment has led to suggestions for their use as sentinel organisms for cadmium and other marine pollutants (Ray, 1986). Molluscs accumulate cadmium directly from water or indirectly from food and detrital particles, and translocate it throughout the body by active and passive transport mechanisms (Ray, 1986). Accumulation from water occurs by passive diffusion through the body surface and from water passing through the gills. Accumulation from food is less well studied. The previous studies focus on *L. stagnalis* (Nikanorov et al., 1985; Balogh et al., 1988; Gomot, 1997; Pyatt et al., 2002; Russo et al., 2007; Gust et al., 2012), *B. glabrata* (Münzinger, 1987; Allah et al., 2002), *Bullia rhodostoma* (Watling & Watling, 1983), *Brachionus calyciflorus* and *Chironomus tentans* (Grosell et al., 2006).

Other studies show the presence of cadmium in the gills of marine bivalves (Hardy et al., 1981). This has established the use of bivalve gills as a convenient assay for measuring bioavailability of metals from seawater. Such effects have already been documented for *Mercenaria mercenaria* (Zaroogian & Anderson, 1995; Zaroogian & Norwood, 2001), *Donax serra* (Watling & Watling, 1983) and zebra mussels (Giamberini & Pihan, 1996).

Abd Allah et al. (2002) examined the effects of heavy metal exposure on the growth, mortality and reproduction of *B. glabrata*. Balogh et al. (1988) used cadmium, copper, iron, chromium, hydragyrum, lead, zinc and manganese to prove that there is a correlation between the pollution of the environment and the heavy metal concentrations found in *L. stagnalis*. Pyatt et al. (2002) showed that the individuals of *L. stagnalis* from a lead contaminated environment have significantly greater survivability than those form unpolluted environment to acute exposure to lead, which inhibits several behavioral activities. Gomot (1998) studied the effects of cadmium on the number of egg masses, number of eggs, embryo development and hatching of *L. stagnalis*. This author also observed that the egg production was reduced and the development and hatching were delayed.

Harley (www.safenano.org) proposed *L. stagnalis* as a suitable species for investigating life-cycle effects from nanoparticle exposure. These particles could cross cellular membranes and lead to cellular damage. Similar ideas are discussed by Ali et al. (2014). They demonstrated that silver nanoparticles induced oxidative stress and DNA damage in the digestive gland of *Lymnaea luteola*. Pollutants are transferred by blood cells to the digestive gland, which is one of the major targets of accumulation. They concluded that the following biomarkers could be used to monitor aquatic pollution: malondialdehyde, glutathione, catalase, glutathione peroxidase and glutathione S-transferase.

B. glabrata is considered as a bioindicator organism to assess cadmium, lead and arsenic exposure (Ansaldo et al., 2006). These metals are not detoxified in the

environment and the risk of human exposure is increasing. Cadmium and lead are extensively used in modern industry and the arsenic water contamination is considered a world concern for human health. The impacts of the chemical stress caused by 96 h exposure to different concentrations of these metals were tested (Ansaldo et al., 2006). Significant decreases in the polysaccharide content as well as in the levels of glycogen were observed. This suggests the use of the glycogen level as an indicator of the heavy metal stress in this animal. Glycogen is an important energetic reserve and used up rapidly under stress. Cadmium and lead followed a similar pattern of bioaccumulation mainly in the digestive gland region; arsenic bioaccumulation showed the highest values in the gonadal region. It should be mentioned that *B. glabrata* is so sensitive to environmental changes that even by modulating the temperature, its resistance phenotype to *Schistosoma mansoni* infection could be reversed (Ittiprasert & Knight, 2012).

The use of freshwater mussels for biomonitoring purpose is mostly a recent phenomenon (Singh et al., 2011). Behavioral changes can be used as warning systems for the water quality monitoring or in case of toxicity bioassays. A tool for such biotests is the multispecies freshwater biomonitor (MFB), which is based on the quadropole impedance conversion technology (Gerhardt et al., 1994; Gerhardt & Schmidt, 2002). The organisms are placed in a cylindrical flow through an acryl glass chamber and move freely between two pairs of electrodes on each side wall of this chamber. The movements produce changes in the electrical field, which can be measured as changes in the impedance of the system (for more information on the set up of the system see Gerhardt et al., 1994). Such a continuous monitoring by recording changes in different types of behavior, such as feeding, swimming, predation and ventilation as indicators for chemical stress could be a reliable system. The more parameters and species are included, the more sensitive and reliable the system will be, as one species may not react to the chemical stress. Wermann et al. (2003) described *L. stagnalis* as a test organism for the multispecies freshwater biomonitor. Also the related species *L. acuminate* has been proposed as a sentinel organism for monitoring the water pollutant (Singh et al., 2011).

Due to our results, we propose both *B. glabrata* and *L. stagnalis* as biomarkers for monitoring heavy metal impact on freshwater ecosystems. During this work, it has been demonstrated that rhogocytes play a role in the detoxification, as the cadmium ions appear to accumulate inside these cells after exposure of the animals to cadmium contamination. Furthermore, there seems to be a correlation between the level of exposure and structural changes of rhogocytes. Higher concentrations of cadmium contamination yielded more intense changes of the cell structure. Under the present conditions, exposure times significantly longer than 96 h led to the death of the animals. Our snails breed round the year and are very sensitive to changes in the quality of water. Also the expression pattern of prominent proteins such as hemocyanin changes due to environmental factors.

Conclusively, *B. glabrata* and *L. stagnalis* appear to be suitable candidates for biological monitoring and screening of effects of such substances on the freshwater environment. This might be done by recording, in a multispecies freshwater biomonitor, changes in behavior, and periodically assessing, in the electron microscope, structural changes of their rhogocytes.

19. Summary

Rhogocytes, also termed 'pore cells', exist free in the hemolymph or embedded in the connective tissue of different body parts of molluscs, notably gastropods. These unique cells can be round, elongated or irregularly shaped, and up to 30 μm in diameter. Their hallmark is the so-called slit apparatus: i.e. pocket-like invaginations of the plasma membrane creating extracellular lacunae, bridged by cytoplasmic bars. These bars form distinctive slits of ca. 20 nm width. A slit diaphragm composed of proteins establishes a molecular sieve with holes of 20 x 20 nm.

Different functions have been assigned to this special molluscan cell type, notably biosynthesis of the hemolymph respiratory protein hemocyanin. It has further been proposed, but not proven, that in the case of red-blooded snail species rhogocytes might synthesize the hemoglobin. However, the secretion pathway of these hemolymph proteins, and the functional role of the enigmatic slit apparatus remained unclear. Additionally proposed functions of rhogocytes, such as heavy metal detoxification or hemolymph protein degradation, are also not well studied.

This work provides more detailed electron microscopical, histological and immunobiochemical information on the structure and function of rhogocytes of the freshwater snails *Biomphalaria glabrata* and *Lymnaea stagnalis*. By *in situ* hybridization on mantle tissues, it proves that *B. glabrata* rhogocytes synthesize hemoglobin and *L. stagnalis* rhogocytes synthesize hemocyanin.

Hemocyanin is present, in endoplasmic reticulum lacunae and in vesicles, as individual molecules or pseudo-crystalline arrays. The first 3D reconstructions of rhogocytes are provided by means of electron tomography and show unprecedented details of the slit apparatus. A highly dense material in the cytoplasmic bars close to the diaphragmatic slits was shown, by immunogold labeling, to contain actin. By immunofluorescence microscopy, the protein nephrin was localized at the periphery of rhogocytes. The presence of both proteins in the slit apparatus supports the previous hypothesis, hitherto solely based on similarities of the ultrastructure, that the molluscan rhogocytes are phylogenetically related to mammalian podocytes and insect nephrocytes. A possible secretion pathway of respiratory proteins that includes a transfer mechanism of vesicles through the diaphragmatic slits is proposed and discussed.

We also studied, by electron microscopy, the reaction of rhogocytes *in situ* to two forms of animal stress: deprivation of food and cadmium contamination of the tank water. Significant cellular reactions to both stressors were observed and documented. Notably, the slit apparatus surface and the number of electron-dense cytoplasmic vesicles increased in response to cadmium stress. Food deprivation led to an increase in hemocyanin production. These observations are also discussed in the framework of using such animals as potential environmental biomarkers.

20. Zusammenfassung

Rhogocyten, auch Porenzellen genannt, existieren frei in der Hämolymphe oder eingebettet im Bindegewebe verschiedener Körperteile von Mollusken, insbesondere von Gastropoden (Schnecken). Sie können rund, länglich oder irregulär geformt sein und besitzen einen Durchmesser von bis zu 30 μm. Ihr auffälligstes Merkmal ist der so genannte Schlitzapparat; dabei handelt es sich um taschenförmige Einstülpungen der Plasmamembran, wodurch extrazelluläre, von cytoplasmatischen Stäben überbrückte Lakunen entstehen. Zwischen diesen Stäben existieren auffällige Schlitze von ca. 20 nm Breite. Ein Schlitz-Diaphragma aus Proteinen bildet ein Molekularsieb mit Filtrationsporen von 20×20 nm.

Diesem besonderen Zelltyp der Mollusken hat man eine ganze Reihe von Funktionen zugeschrieben, insbesondere die Produktion des respiratorischen Hämolympheproteins Hämocyanin. Zudem wurde vermutet, aber noch nicht nachgewiesen, dass die Rhogocyten bei Schneckenarten mit rotem Blut das Hämoglobin produzieren. Die Sekretionswege dieser Hämolympheproteine und die funktionelle Rolle des Schlitzapparats blieben unklar. Zusätzlich vorgeschlagene Funktionen von Rhogocyten, wie Schwermetallentgiftung oder der Abbau von Hämolympheproteinen, sind ebenfalls nicht gut untersucht.

Die vorliegende Arbeit liefert detaillierte elektronenmikroskopische, histologische und immunobiochemische Informationen zur Struktur und Funktion von Rhogocyten der Süsswasserschnecken *Biomphalaria glabrata* und *Lymnaea stagnalis*. Sie zeigt durch *in situ* Hybridisierung von Mantelgewebe, dass Rhogocyten von *B. glabrata* Hämoglobin und solche von *L. stagnalis* Hämocyanin synthetisieren. Hämocyanin wurde teils als pseudokristalline Felder, teils als Einzelmoleküle in Lakunen des Endoplasmatischen Reticulums sowie in Vesikeln beobachtet. Mittels Elektronentomographie wurden hier die ersten 3D-Rekonstruktionen von Rhogocyten erstellt; sie zeigen den Schlitzapparat in bisher nicht erreichten Details. Dabei wurde in den cytoplasmatischen Stäben nahe den Schlitzen ein hochdichtes Material beobachtet. Durch Immunogoldmarkierung wurden Belege dafür gesammelt, dass Aktin eine der Komponenten dieses Materials ist. Mittels Immunofluoreszenzmikroskopie konnte in der Peripherie der Rhogocyten das Protein Nephrin lokalisiert werden. Die Anwesenheit dieser beiden Proteine unterstützt die zuvor ausschließlich auf Ähnlichkeiten in der Ultrastruktur basierende Hypothese, dass die Rhogocyten der Mollusken phylogenetisch mit den Podocyten der Vertebraten und Nephrocyten der Insekten verwandt sind. Ein möglicher Sekretionsweg der respiratorischen Proteine, der einen Transfermechanismus von Vesikeln durch die diaphragmatischen Schlitze einschließt, wird vorgeschlagen und diskutiert.

Zudem wurde die Reaktion von Rhogocyten *in situ* auf zwei Formen von Tierstress elektronenmikroskopisch untersucht: Entzug von Nahrung und Cadmiumbelastung des Wohnwassers. Es wurden signifikante zelluläre Reaktionen auf beide Stressoren beobachtet und dokumentiert. Als Reaktion auf Cadmiumbelastung vergrößerte sich die Oberfläche des Schlitzapparats und erhöhte sich die Anzahl an elektronendichten cytoplasmatischen Vesikeln. Nahrungsentzug führte zu einer vermehrten Produktion von Hämocyanin. Diese Beobachtungen wurden auch unter dem Gesichtspunkt einer Verwendung dieser Tiere als potentielle Umwelt-Biomarker diskutiert.

Part V.

References

ABD ALLAH, A.T.; WANAS, M.Q.A.; THOMPSON, S.N. (2002): Dissolved heavy metals, lead, cadmium and mercury, accumulate in the body of the schistosome vector, *Biomphalaria glabrata* (Gastropoda: Pulmonata). J Moll Stud 69: 35-41

ABDEL-MALEK, E.T. (1955): Anatomy of *Biomphalaria boissyi* as related to its infection with *Schistosoma mansoni*. Am Midl Nat 54(2): 394-404

AFONSO, A.M.; ARRIETA, M.R.; NEVES, A.G. (1976): Characterization of the hemoglobin of *Biomphalaria glabrata* as a glycoprotein. Biochim Biophys Acta 439(1): 77-81

ALBRECHT, U.; KELLER, H.; GEBAUER, W.; MARKL, J. (2001): Rhogocytes (pore cells) as the site of hemocyanin biosynthesis in the marine gastropod *Haliotis tuberculata*. Cell Tissue Res 304: 455-462

ALI, D.; YADAV, P.G.; KUMAR, S.; ALI, H.; ALARIFI, S.; HARRATH, A.H. (2014): Sensitivity of freshwater pulmonate snail *Lymnaea luteola* L. to silver nanoparticles. Chemosphere 104: 134-140

ALMEIDA, A.P.; NEVES A.G. (1974): The hemoglobin of *Biomphalaria glabrata*: chemical composition and some physicochemical properties. Biochim Biophys Acta 371(1): 140-146

ANSALDO, M.; NAHABEDIAN, D.E.; HOLMES-BROWN, E.; AGOTE, M.; ANSAY, C.V.; VERRENGIA GUERRERO, N.R.; WIDER, E.A. (2006): Potential use of glycogen level as biomarker of chemical stress in *Biomphalaria glabrata*. Toxicology 224: 119-127

ARNDT, M.H.L.; NASCIMENTO, D.G.; XAVIER, L.P.; SANTORO, M.M. (1998): The myoglobin and the hemoglobin of *Biomphalaria glabrata*, an evidence of gene duplications. Mem Inst Oswaldo Cruz 93(Suppl 1): 171-172

BALOGH, K.V.; FERNANDEZ, D.S.; SALANKI, J. (1988): Heavy metal concentrations of *Lymnaea stagnalis* L. in the environs of lake Balaton (Hungary). Wat Res 22(10): 1205-1210

BANI, G.; FORMIGU, L.; COCCHI, R. (1990): Morphological study on the salivary glands of *Eobania vermiculans* (Müller) (Mollusca, Pulmonata). Z Mikrosk Anat Forsch 104: 856-870

BAUMEISTER, W.; GRIMM, R.; WALZ, J. (1999): Electron tomography of molecules and cells. Trends Cell Biol 9: 81-85

BEUERLEIN, K.; LÖHR, S.; WESTERMANN, B.; RUTH, P.; SCHIPP, R. (2002b): Components of the cellular defense and detoxification of the common cuttlefish *Sepia officinalis* (Mollusca, Cephalopoda). Tissue Cell 34(6): 390-396

BEUERLEIN, K.; RUTH, P.; WESTERMANN, B.; LÖHR, S.; SCHIPP, R. (2002a): Hemocyanin and the branchial heart complex of *Sepia officinalis*: are the hemocytes involved in hemocyanin metabolism of coleoid cephalopods? Cell Tissue Res 310: 373-381

BIELEFELD, U.; KÖRTJE, K.H.; RAHMANN, H.; BECKER, W. (1993): The shell-forming mantle epithelium of *Biomphalaria glabrata* (Pulmonata): Ultrastructure, permeability and cytochemistry. J Moll Stud 59: 323-338

BOER, H.H.; SMINIA, T. (1976): Sieve structure of slit diaphragms of podocytes and pore cells of gastropod molluscs. Cell Tissue Res 170: 221-229

BONAVENTURA, J.; BONAVENTURA, C. (1980): Hemocyanins: relationships in their structure, function and assembly. Am Zool 20: 7-17

BRUMMENDORF, T.; RATHJEN, F.G. (1994): Cell adhesion molecules. 1: immunoglobulin superfamily. Protein Profile 1: 951-1058

BUGGE, J.; WEBER, R.E. (1999): Oxygen binding and its allosteric control in hemoglobin of the pulmonate snail, *Biomphalaria glabrata*. Am J Physiol 276: R347-356

CAVALCANTI, M.G.S.; FILHO, F.C.; MENDONCA, A.M.B.; DUARTE, G.R.; BARDOSA, C.C.G.S.; De CASTRO, C.M.M.B.; ALVES, L.C.; BRAYNER, F.A. (2012): Morphological characterization of hemocytes from *Biomphalaria glabrata* and *Biomphalaria straminea*. Micron 43(2-3): 285-291

CAVALIER, A.; SPEHNER, D.; HUMBEL, B.M. (2009): Handbook of cryo-preparation methods for electron microscopy, CRC Press.

COEURDASSIER, M.; DE VAUFLEURY, A.; BADOT, P.M. (2003): Bioconcentration of cadmium and toxic effects on life-history traits of pond snails (*Lymnaea palustris* and *Lymnaea stagnalis*) in laboratory bioassays. Arch Environ Contam Toxicol 45: 102-109

DALLINGER, R.; BERGER, B.; HUNZIKER, P.; KÄGI, J.H.R. (1997): Metallothionein in snail Cd and Cu metabolism. Nature 388: 237-238

DALLINGER, R.; CHABICOVSKY, M.; HODL, E.; PREM, C.; HUNZIKER, P.; MANZL, C. (2005): Copper in *Helix pomatia* (Gastropoda) is regulated by one single cell type: differently responsive metal pools in rhogocytes. Am J Physiol Regul Integr Comp Physiol 289(4): R1185-1195

DANSCHER, G. (1981): Histochemical demonstration of heavy metals: A revised version of the sulphide silver method suitable for both light and electron microscopy. Histochemistry 71: 1–16

DE CARLO, S.; HARRIS, J.R. (2011): Negative staining and cryo-negative staining of macromolecules and viruses for TEM. Micron 42: 117-131

DECKER, H.; TUCZEK, F. (2000): Tyrosinase/catecholoxidase activity of hemocyanins: structural basis and molecular mechanism. TIBS 25: 392-397

DECKER, H.; HELLMANN, N.; JAENICKE, E.; LIEB, B.; MEISSNER, U.; MARKL, J. (2007): Minireview: Recent progress in hemocyanin research. Integr Comp Biol 47(4): 631-644

DEGRAEVE, N. (1981): Carcinogenic, teratogenic and mutagenic effects of cadmium. Mutation Res 86: 115-135

DILLY, P.N.; MESSENGER, J.B. (1972): The branchial gland: a site of hemocyanin synthesis in *Octopus*. Z Zellforsch 132: 193-201

DOS SANTOS SOUZA, S.; ANDRADE, Z.A. (2006): On the origin of the *Biomphalaria glabrata* hemocytes. Mem Inst Oswaldo Cruz 101(Suppl 1): 213-218

DRUMMOND, A.J.; ASHTON, B.; BUXTON, S.; CHEUNG, M.; COOPER, A.; DURAN, C.; FIELD, M.; HELED, J.; KEARSE, M.; MARKOWITZ, S.; MOIR, R.; STONES-HAVAS, S., STURROCK, S.; THIERER, T.; WILSON, A. (2011): Geneious v5.4. Available from http://www.geneious.com/

ELLERTON, H.D., ELLERTON, N.F.; ROBINSON, H.A. (1983): Hemocyanin - a current perspective. Prog Biophys Mol Biol 41(3): 143-248

FAHRENBACH, W.H. (1970): The cyanoblast: hemocyanin formation in *Limulus polyphemus*. J Cell Biol 44(29): 445-453

FERARD, J.F.; JOUANY, J.M.; TRUHAUT, R.; VASSEUR, P. (1981): Accumulation of cadmium in a freshwater food chain experimental model. Ecotox Environ Safety 7(1): 43-52

FERNANDEZ, J. (1966): Nervous system of the snail *Helix aspersa*. I. Structure and histochemistry of ganglionic sheath and neuroglia. J Comp Neurol 197: 157-182

FlORONI, P.; SUNDERMANN, G .; SCHEIDEGCER, D. P. (1984): Die Ultrastruktur der freien Rhogocyten bei intrakapsularen Veligem von *Nucella lapillus* (Gastropoda, Prosobranchia, Stenoglossa). Zool Anzeiger 212: 193-202

FISHBEIN, L. (1981): Sources, transport and alterations of metal compounds: An overview. I. Arsenic, beryllium, cadmium, chromium, and nickel. Environ Health Perspect 40: 43-64

FOURNIE, J.; CHETAIL, M. (1982): Accumulation calcique au niveau cellu- laire chez les mollusques. Malacologia 22: 265-284

GALL, J.G. (1966): Microtubule fine structure. J Cell Biol 31: 639-643

GAO, W.; WIEDERHOLD, M.L. (1997): The structure of the statocyst of the freshwater snail *Biomphalaria glabrata* (Pulmonata, Basommatophora). Hearing Res 109: 109-124

GARG, P.; VERMA, R.; NIHALANI, D.; JOHNSTONE, D.B., HOLZMAN, L.B. (2007): Neph1 cooperates with nephrin to transduce a signal that induces actin polymerization. Mol Cell Biol 27: 8698-8712

GATSOGIANNIS, C.; MARKL, J. (2009): Keyhole limpet hemocyanin: 9 Å cryo-EM structure and molecular model of the KLH1 didecamer reveal the interfaces and intricate topology of the 160 functional units. J Mol Biol 385(3): 963-983

GATSOGIANNIS, C.; MOELLER, A.; DEPOIX, F.; MEISSNER, U.; MARKL, J. (2007): *Nautilus pompilius* hemocyanin: 9 Å cryo-EM structure and molecular model reveal the subunit pathway and the interfaces between the 70 functional units. J Mol Biol 374(2): 465-486

GERHARDT, A.; CLOSTERMANN, M.; FRIDLUND, B.; SVENSSON, B. (1994): Monitoring of behavioural patterns of aquatic organisms with an impedance conversion technique. Environ International 20(2): 209-219

GERHARDT, A.; SCHMIDT, S. (2002): The multispecies freshwater biomonitor. A potential new tool for sediment biotests and biomonitoring. J Soils & Sediments 2(2): 67-70

GHANAATI, S.; BARBECK, M.; HILBIG, C.; UNGER, R.E.; SADER, R.A.; PETERS, F.; KIRKPATRICK, C.J. (2011): An injectable bone substitute composed of beta-tricalcium phosphate granules, methylcellulose and hyaluronic acid inhibits connective tissue influx into its implantation bed *in vivo*. Acta Biomater 11: 4018-4028

GHANAATI, S.; BARBECK, M.; ORTH, C.; WILLERSHAUSEN, I.; THIMM, B.W.; HOFFMANN, C.; RASIC, A.; SADER, R.A.; UNGER, R.E.; PETERS, F.; KIRKPATRICK, C.J. (2010): Influence of β-tricalcium phosphate granule size and morphology on tissue reaction *in vivo*. Acta Biomater 12: 4476-4487

GHANAATI, S.; ORTH, C.; BARBECK, M.; WILLERSHAUSEN, I.; THIMM, B.W.; BOOMS, P.; STÜBINGER, S.; LANDES, C.; SADER, R.A.; KIRKPATRICK, C.J. (2010): Histological and histomorphometrical analysis of a silica matrix embedded nanocrystalline hydroxyapatite bone substitute using the subcutaneous implantation model in Wistar rats. Biomed Mater 5(3) 035005

GIAMBERINI, L.; PIHAN, J.C. (1996): The pericardial glands of the zebra mussel: Ultrastructure and implication in lead detoxication process. Biol Cell 86: 59-65

GOMOT, A. (1997): Toxic Effects of cadmium on reproduction, development, and hatching in the freshwater snail *Lymnaea stagnalis* for water quality monitoring. Ecotoxicol and Environ Safety 41: 288-297

GROSELL, M.; GERDES, R.M.; BRIX, K.V. (2006): Chronic toxicity of lead to three freshwater invertebrates- *Branchionus calyciflorus*, *Chironomus tentans*, and *Lymnaea stagnalis*. Environ Toxicol Chem 1: 97-104

GUST, M.; FORTIER, M.; GARRIC, J.; FOURNIER, M.; GAGNE, F. (2013): Immunotoxicity of surface waters contaminated by municipal effluents to the snail *Lymnaea stagnalis*. Aquatic Toxicol 126: 393-403

HALL, R.L.; PEARSON, J.S.; WOOD, E.J. (1975): The hemocyanin of *Lymnaea stagnalis* (Gastropoda: Pulmonata). Comp Biochem Physiol 52B: 211-218

HANAICHI, T.; SATO, T.; IWAMOTO, T.; MALAVASI-YAMASHIRO, J.; HOSHINO, M.; MIZUNO, N. (1986): A stable lead by modification of Sato's method. J Electron Microsc 35:304

HANDKE, B.; POERNBACHER, I.; GOETZE, S.; AHRENS, C.H.; OMASITS, U.; MARTY, F.; SIMIGDALA, N.; MEYER, I.; WOLLSCHEID, B.; BRUNNER, E.; HAFEN, E.; LEHNER, C.F. (2013): The hemolymph proteome of fed and starved *Drosophila* larvae. PLoS One 8: e67208

HARDY, J.T.; SCHMIDT, R.L.; APTS, C.W. (1981): Marine sediment and interstitial water: Effects on bioavailability of cadmium to gills of the clam *Protothaca staminea*. Bull Environ Contam Toxicol 27: 798-805

HARDY, J.T.; SULLIVAN, M.F.; CRECELIUS, E.A.; APTS, C.W. (1984): Transfer of cadmium in a phytoplankton-oyster-mouse food chain. Arch Environ Contam Toxicol 13: 419-425

HARLEY, S.S.: Nanoecotoxicity testing with *Lymnaea stagnalis*. www.safenano.org

HARRIS, J.R.; GEBAUER. W.; GUDERIAN, F.U.M.; MARKL, J. (1997a): Keyhole limpet hemocyanin (KLH), I: reassociation from Immucothel® followed by separation of KLH1 and KLH2. Micron 28: 31–41

HARRIS, J.R.; GEBAUER, W.; SÖHNGEN, S.M.; NERMUT, MV.; MARKL, J. (1997b): Keyhole limpet hemocyanin (KLH), II: characteristic reassociation properties of purified KLH1 and KLH2. Micron 28: 43–56

HARRIS, J.R.; MARKL, J. (1992): Electron microscopy of a double helical tubular filament in keyhole limpet (*Megathura crenulata*) hemolymph. Cell Tissue Res 269: 411-420

HARRIS, J.R.; MARKL, J. (1999): Keyhole limpet hemocyanin (KHL): a biomedical review. Micron 30: 597-623

HARRIS, J. R.; SCHEFFLER, D. (2002): Routine preparation of air-dried negatively stained and unstained specimens on holey carbon support films: a review of applications. Micron 33: 461-480

HASZPRUNAR, G. (1996): The molluscan rhogocyte (pore cell, blasenzelle, cellule nucale) and its significance for ideas on nephridial evolution. J Moll Stud 62: 185-211

HAYAT, M.A. (2000): Principles and techniques of electron microscopy, Biological applications, Fourth Edition, Kean University, Union, New Jersey, Cambridge, University Press

HELMY, S.; PORTER-JORDAN, K.; DAWIDOWICZ, E.A.; PILCH, P.; SCHWARTZ, A.L.; FINE R.E. (1986): Separation of endocytic from exocytic coated vesicles using a novel cholinesterase mediated density shift technique. Cell 44: 497-506

HUNG, Y. (1982): Effects of temperature and chelating agents on cadmium uptake in the american oyster. Bull Environ Contam Toxicol 28: 546-551

ICHIMURA, K.; KURIHARA, H.; SAKAI, T. (2003): Actin filament organization of foot processes in rat podocytes. J Histochem Cytochem 51(12): 1589-1600

ITTIPRASERT, W.; KNIGHT, M. (2012): Reversing the resistance phenotype of the *Biomphalaria glabrata* snail host *Schistosome mansoni* infection by temperature modulation. PLoS Pathogens 8(4): e1002677

JACOBSON, K.B.; OPRESKO, L.; OWENBY, R.K.; CHRISTIE, N.T. (1981): Effects of cadmium on *Drosophila*: Toxicity, proteins, and transfer RNAs. Toxicol Appl Pharmacol 60: 368-378

JONES, G.W.; BOWEN, I.D. (1979): The fine structural localization of acid phosphatase in pore cells of embryonic and newly hatched *Deroceras reticulatum* (Pulmonata: Stylommatophora). Cell Tissue Res 204: 253-265

KESTILÄ, M.; LENKKERI, U.; MÄNNIKKÖ, M.; LAMERDIN, J.; McCREADY, P.; PUTAALA, H.; RUOTSALAINEN, V.; MORITA, T.; NISSINEN, M.; HERVA, R.; KASHTAN, C.E.; PELTONEN, L.; HOLMBERG, C.; OLSEN, A.; TRYGGVASON, K. (1998). Positionally cloned gene for a novel glomerular protein –nephrin– is mutated in congenital nephrotic syndrome. Mol Cell 1(4): 575-82

KISKER, L.G. (1923): Über die Anordnung und den Bau der interstitiellen Bindesubstanzen von *Helix pomatia* L.. Z Wiss Zool 121: 64-125

KITAJIMA, E.W.; PARAENSE, W.L. (1983): The ultrastructure of the spermatheca of *Biomphalaria glabrata* (Gastropoda, Pulmonata). J Morph 176: 211-220

KOKKINOPOULOU, M.; GÜLER, M.A.; LIEB, B.; BARBECK, M.; GHANAATI, S.; MARKL, J. (2014): 3D –ultrastructure, functions and stress responses of gastropod (*Biomphalaria glabrata*) rhogocytes. PLoS ONE 9(6): e101078

KREMER, J. R.; MASTRONARDE, D. N.; McINTOSH, J. R. (1995): Computer visualization of three-dimensional image data using IMOD. J Struct Biol 116: 71-76

LESSARD, J.L. (1988): Two monoclonal antibodies to actin: One muscle selective and one generally reactive. Cell Motil Cytoskel 10: 349–362

LIEB, B.; ALTENHEIN, B.; MARKL, J.; VINCENT, A.; VAN OLDEN, E.; VAN HOLDE, K.E.; MILLER, K.I. (2001): Structures of two molluscan hemocyanin genes: significance for gene evolution. PNAS 98(8): 4546-4551

LIEB, B.; BOISGUERIN, V.; GEBAUER, W.; MARKL, J. (2004): cDNA sequence, protein structure, and evolution of the single hemocyanin from *Aplysia californica*, an opisthobranch gastropod. J Mol Evol 59: 536-545

LIEB, B.; DIMITROVA, K.; KANG, H.S.; GEBAUER, W.; MARTIN, A.; HANELT, B.; SAENZ, S.A.; ADEMA, C.M.; MARKL, J: (2006): Red blood with blue-blood ancestry: Intriguing structure of a snail hemoglobin. PNAS 103(32): 12011-12016

LIEB, B.; GEBAUER, W.; GATSOGIANNIS, C.; DEPOIX, F.; HELLMANN, N.; HARASEWYCH, M.G.; STRONG, E.E.; MARKL, J. (2010): Molluscan megahemocyanin: an ancient oxygen carrier tuned by a 550 kDa polypeptide. Front Zool. 7: 14

MANUBENS, A.; SALAZAR, F.; HAUSMANN, D.; FIGUEROA, J.; DEL CAMPO, M.; MARTINEZ PINTO, J.; HUAQUIN, L.; VENEGAS, A.; BECKER, M.I. (2010): *Concholepas* hemocyanin biosynthesis takes place in the hapetopancreas, with hemocytes being involved in its metabolism. Cell Tissue Res 342: 423-435

MARIGOMEZ, I.; SOTO, M.; CAJARAVILLE, M.P.; ANGULO, E.; GIAMBERINI, L. (2002): Cellular and subcellular distribution of metals in molluscs. Microsc Res Tech 56: 358-392

MARIGOMEZ, J.A.; CAJARAVILLE, M.P.; ANGULO, E. (1990): Cellular cadmium distribution in the common winkle, *Littorina littorea* determined by x-ray microprobe analysis and histochemistry. Histochemistry 94: 191-199

MARKL, J. (2013): Evolution of molluscan hemocyanin structures. Biochim Biophys Acta 9: 1840-1852

MARKL, J.; DECKER, H. (1992): Molecular structure of the arthropod hemocyanins. Adv Comp Environ Physiol 13: 325-376

MARKL, J.; STUMPP, S.; BOSCH, F.X.; VOIT, R. (1990): Hemocyanin biosynthesis in a tarantula, studied by *in situ* hybridization and immunocytochemistry. Invertebrate dioxygen carriers (Preaux G, Lontie R, eds.). University Press, Louvain, Belgium, pp 497-502

MARTIN, A.M.; MARTIN, G.G.; BUTLER, R.; GOFFREDI, S.K. (2011): Synthesis of keyhole limpet hemocyanin by the rhogocytes of *Megathura crenulata*. Invertebrate Biol 130(4): 302-312

MASON, A.Z.; SIMKISS, K.; RYAN, K.P. (1984): The ultrastructural localization of metals in specimens of *Littorina littorea* collected from clean and polluted sites. J. Mar Biol Assoc UK 64: 699-720

McINTOSH, R.; NICASTRO, D.; MASTRONARDE, D. (2005): New views of cells in 3D: an introduction to electron tomography. Trends Cell Biol Vol 15: 43-51

MEISTER, G. (1977): Untersuchungen an vakuolisierten Rundzellen im Blut von Embryonen verschiedener Tintenfisch-Arten (Mollusca, Cephalopoda). Zool Jahrb Abt Anat 97: 54-67

MILLER, K.I.; VAN HOLDE, K.E. (1982): The structure of *Octopus dofleini* hemocyanin. Comp Biochem Physiol 73B(4): 1013-1018

MOELLER, V.; DÜRR, R.; SARRAF-ZADEH, L.; KELLER, S.; HEINZ, S.; HELLMANN, N.; MOELLER, A.; LIEB, B.; MARKL, J. (2011): Recombinant functional multidomain hemoglobin from the gastropod *Biomphalaria glabrata*. IUBMB Life 63: 323-328

MORGAN, A.J.; MORRIS, B. (1982): The accumulation and intracellular compartmentation of cadmium, lead, zinc and calcium in two earthworm species (*Dendrobaena rubida* and *Lumbricus rubellus*) living in highly contaminated soil. Histochem 75(2): 269-285

MORSE, P.M.; COOPER, M.S. (1993): Endocytosis of hemolymph fluid in the connective tissue pore cells of the pectinid scallop, *Chlamys hastate*. Am Zool 33: 22A

MÜNZIGER, A. (1987): *Biomphalaria glabrata* (say), a suitable organism for a biotest. Environ Technol Lett 8: 141-148

MUZII, E. (1981): Intracellular polymerized hemocyanin in the branchial gland of a cephalopod. Cell Tissue Res 220: 435-438

NIKANOROV, A.M.; ZHULIDOV, A.V.; POKARZHEVSKIJ, A.D. (1985): Biomonitoring of heavy metals in freshwater ecosystems (in Russian). Lenigrad, Hydrometeoizdat, 144 pp., 30 Tabs., 8 Figs., Rubel 1, 50

NOTT, J.A.; BEBIANNO, M.J.; LANGSTON, W.J.; RYAN, K.P. (1993): Cadmium in the gastropod *Littorina littorea*. J Mar Biol Ass UK 73(3): 655-665

PARKER, L.M.; ROSS, P.M.; O'CONNOR, W.A.; PÖRTNER, H.O.; SCANES, E.; WRIGHT, J.M. (2013): Predicting the response of molluscs to the impact of ocean acidification. Biology 2(2): 651-692

PATRAKKA, J.; TRYGGVASON, K. (2007): Nephrin - a unique structural and signaling protein of the kidney filter. Trends Mol Med 13: 396-403

PAUL, R.J.; ZAHLER, S.; WERNER, R.; MARKL, J. (1991): Adaption of an open circulatory system to the oxidative capacity of different muscle cell types. Naturwissenschaften 78: 134-135

PLUMMER, J.M. (1966): Collagen formation in Achatinidae associated with a specific cell type. Proc Malacol Soc London 37: 189-197

PRINCE, J.S.; JOHNSON, P.M. (2006): Ultrastructural comparison of *Aplysia* and *Dolabrifera* ink glands suggests cellular sites of anti-predator protein production and algal pigment processing. J Moll Stud 72: 349-357

PYATT, A.J. PYATT, F.B. PENTREATH, V.W. (2002): Lead toxicity, locomotion and feeding in the freshwater snail, *Lymnaea stagnalis* (L.). Invert Neurosci 4: 135-140

RAGHAVAN, N.; KNIGHT, M. (2006): The snail (*Biomphalaria glabrata*) genome project. Trends Parasitol 22: 148-151

RAY, S. (1986): Bioaccumulation of cadmium in marine organisms. Experientia Suppl. 50: 65-75

RIEGER, R.M.; TYLER, S. (1979): The homology theorem in ultrastructure research. Am Zool 19: 655-664

RIVEST, B.R. (1992): Studies on the structure and function of the larval kidney complex of prosobranch gastropods. Biol Bull 182: 305-323

RUPPERT, E.E. (1994): Evolutionary origin of the vertebrate nephron. Amer Zool 34: 542-553

RUPPERT, E.E.; SMITH, P.R. (1988): The functional organization of filtration nephridia. Biol Rev 63: 231-258

RUTH, P. (1993): Die Mitteldarmdrüse als Syntheseort für Hämocyanin bei tetrabranchiaten cephalopoden. Verh Dtsch Zool Ges 86: 175

RUTH, P.; SCHIPP, R.; KLUSSENDORF, B. (1988): Cytomorphology and copper content of the basal cell in the midgut gland of *Nautilus* (Cephalopoda, Tetrabranchiata) - a contribution to the location of hemocyanin. Zoomorphology 108(1): 1-11

SAMBROOK, J.; RUSSELL, D.W. (2001): Molecular Cloning, a laboratory manual. Third edition, Cold Spring Harbor Laboratory Press, Cold Spring Harbor, New York

SATO, T. (1968): A modified method for lead staining of thin sections. J Electron Microsc (Tokyo) 17(2): 158-159

SAUR, M.; MÖLLER, V.; KAPETANOPOULOS, K.; BRAUKMANN, S.; GEBAUER, W.; TENZER, S.; MARKL, J. (2012): Acetylcholine-binding protein in the hemolymph of the planorbid snail *Biomphalaria glabrata* is a pentagonal dodecahedron (60 subunits). PLoS One 7: e43685

SCHAFFELD, M.; MARKL, J. (2004): Fish keratins. Method Cell Biol 78: 627-671

SCHIPP, R.; HÖHN, P.; GINKEL, G. (1973): Elektronenmikroskopische und histochemische Untersuchungen zur Funktion der Branchialdrüsse (Parabranchialdrüsse) der Cephalopoda. Z Zellforsch 117: 252-274

SCHMEKEL, L.; WEISCHER, M.L. (1973): Die Blutdrüse der Doridoidea (Gastropoda, Opisthobranchia) als Ort möglicher Hämocyanin-Synthese. Z Morph Tiere 76: 261-284

SCHNEIDER, S.W. (2001): Kiss and run mechanism in exocytosis. J Membr Biol 181: 67-76

SEGAWA, A.; LOFFREDO, F.; PUXEDDU, R.; YAMASHINA, S.; RIVA, F.T.; RIVA, A. (1998): Exocytosis in human salivary glands visualized by high-resolution scanning electron microscopy. Cell Tissue Res 291: 325-336

SIMKISS, K.; MASON, A.Z. (1983): Metal ions: metabolic and toxic effects. in The Mollusca Vol. 2. Environmental Biochemistry and Physiology. Hochachka, P.W., ed., 101-164. Academic Press, New York

SINGH, V.; SINGH, N.; KUMAR, P. (2011): Bioindicator: *Lymnaea acuminate* as sentinel organism for monitoring and analyzing the water pollutant: A Lake study. LAP LAMBERT Academic Publishing

SKELDING, J.M.; NEWELL, P.F. (1975): On the function of pore cells in the connective tissue of terrestrial pulmonate molluscs. Cell Tissue Res 156: 381-390

SMINIA, T. (1972): Structure and function of blood and connective tissue cells of the freshwater pulmonate *Lymnaea stagnalis* studied by electron microscopy and enzyme histochemistry. Z Zellforsch 130: 497-526

SMINIA, T. (1977): Haemocyanin-producing cells in gastropod molluscs. In: Bannister JV (ed) Structure amd function of haemocyanin. Springer, Berlin, 279-288

SMINIA, T.; BOER, HH. (1973): Haemocyanin production in pore cells of the freshwater snail *Lymnaea stagnalis*. Z Zellforsch Mikrosk Anat 145(3): 443-445

SMINIA, T.; BOER, HH.; NIEMANTSVERDRIET, A. (1972): Haemoglobin producing cells in freshwater snails. Z Zellforsch Mikrosk Anat 135(4): 563-568

SMINIA, T.; VLUGT-VAN DAALEN, J.E. (1977): Hemocyanin synthesis in pore cells of the terrestrial snail *Helix aspersa*. Cell Tissue Res 183: 299-301

SMITH, P.R.; RUPPERT, E.E. (1988): Nephridia. In: The ultrastructure of the Polychaeta. W. Westheide and C.O. Hermans (eds.). Microfauna Marina 4: 231-262

STALLING, D.; WESTERHOFF, M.; HEGE, H.C. (2005): Amira: a highly interactive system for visual data analysis. The Visualization Handbook (Elsevier): 749-767

STEWART, H.; WESTLAKE, H.E.; PAGE, L.R. (2014): Rhogocytes in gastropod larvae: developmental transformation from protonephridial terminal cells. Invertebrate Biol 133(1): 47-63

STREIT, B. (1993): Protein binding of lead and cadmium in freshwater snails. Fres Environ Bull 2: 109-113

STREIT, K.; JACKSON, D.; DEGNAN, B.M.; LIEB, B. (2005): Developmental expression of two *Haliotis asinina* hemocyanin isoforms. Differentiation 73: 341-349

SULLIVAN, J.T.; CHENG, T.C. (1974): Structure and function of the mantle cavity of *Biomphalaria glabrata* (Mollusca: Pulmonata). Trans Am Microsc Soc 93(3): 416-420

SULLIVAN, J.T.; CHENG, T.C. (1975): Heavy metal toxicity to *Biomphalaria glabrata* (Mollusca: Pulmonata). Ann NY Acad Sci 266: 437-444

SÜDHOF, T.C.; RIZO, J. (2011): Synaptic vesicle exocytosis. Cold Spring Harb Perspect Biol 3(12): a005637

TANG, G.; PENG, L.; BALDWIN, P.R.; MANN D.S.; JIANG, W.; REES, I.; LUDTKE, S.J. (2007): EMAN2: an extensible image processing suite for electron microscopy. J Struct Biol 157(1): 38-46

TAYLOR, D. (1983): The significance of the accumulation of cadmium by aquatic organisms. Ecotoxicol and Environ Safety 7: 33-42

TERWILLIGER, N.B.; RYAN M.C. (2006): Functional and phylogenetic analyses of phenoloxidases from brachyuran (*Cancer magister*) and branchiopod (*Artemia franciscana*, *Triops longicaudatus*) crustaceans. Biol Bull. 210 (1): 38-50

VAN HEEL, M.; HARAUZ, G.; ORLOVA, EV.; SCHMIDT, R.; SCHATZ, M. (1996): A new generation of the IMAGIC image processing system. J Struct Biol 116: 17-24

VAN HOLDE, K.E. (1997): Respiratory proteins of invertebrates: structure, function and evolution. Zoology 100: 287-297

VAN HOLDE, K.E.; MILLER, K.I. (1995): Hemocyanins. Adv Protein Chem 47: 1-81

VAN HOLDE, K.E.; MILLER, K.I.; DECKER, H. (2001): Hemocyanins and invertebrate evolution. J Biol Chem 276(19): 15563-15566

WALKER, G. (1977): 'Copper' granules in the barnacle *Balanus balanoides*. Marine Biol 39: 343-349

WALKER, C.H.; HOPKIN, S.P.; SIBLY, R.M.; PEAKALL, D.B. (2001): Principles of Exotoxicology. Taylor & Francis, London

WARTIOVAARA, J.; ÖFVERSTEDT, L.G.; KHOSHNOODI, J.;ZHANG, J.; MÄKELÄ, E.; SANDIN, S.; RUOTSALAINEN, V.; CHENG, R.H.; JALANKO, H.; SKOGLUND, U.; TRYGGVASON, K. (2004): Nephrin strands contribute to a porous slit diaphragm scaffold as revealed by electron tomography. J Clin Invest 114(10): 1457-1483

WATLING, H.R. (1982): Comparative study of the effects of zinc, cadmium, and copper on the larval growth of three oyster species. Bull Environ Contam Toxicol 28: 195-201

WATLING, H.R.; WATLING, R.J. (1983): Sandy beach molluscs as possible bioindicators of metal pollution 2. Laboratory studies. Bull Environ Contam Toxicol 31: 339-343

WEAVERS, H.; PRIETO-SANCHEZ, S.; GRAWE, F.; GARCIA-LOPEZ, A.; ARTERO, R.; WILSCH-BRAEUNINGER, M.; RUIZ-GOMEZ, M.; SKAER, H.; DENHOLM, B. (2009): The insect nephrocyte is a podocyte-like cell with a filtration slit diaphragm. Nature 457(7227): 322-326

WEBER, R.E.; VINOGRADOV, S.N. (2001): Nonvertebrate hemoglobins: functions and molecular adaptions. Physiol Rev 81(2): 569-628

WERMANN, F.; RADEHAUS, P.; GERHARDT, A. (2003): Eignung der Schlammschnecke *Lymnaea stagnalis* L. als neuer Testorganismus für den Multispecies Freshwater Biomonitor (MFB). (S.I.:s.n.)

WIEDOW, M.A.; KNEIP, T.J.; GARTE, S.J. (1982): Cadmium-binding proteins from blue crabs (*Callinectes sapidus*) environmentally exposed to cadmium. Environ Res 28: 164-170

WILLIAMS, D.B.; CARTER, C.B. (1996): Transmission electron microscopy, Basics. Plenum Press

WOLBURG-BUCHHOLZ, K. (1972): Blasenzellen im Bindegewebe des Schlundrings von *Cepaea nemoralis* L. (Gastropoda, Stylommatophora) II. Aufnahme und Speicherung von Ferritin. Z Zellforsch Mikrosk Anat 130: 262-278

WOLFRUM, U.; SCHMITT, A. (2000): Rhodopsin transport in the membrane of the connecting cilium of mammalian photoreceptor cells. Cell Motil Cytoskel 46: 95–107

WOOD, E.J.; BONAVENTURA J. (1981): Identification of *Limulus polyphenus* haemocyanin messenger RNA. Biochem J. 196 (2): 653-656

WOOD, J.E.; CORFIELD, G.C.; SIGGENS, K.W. (1981): Biosynthesis of haemocyanin in *Lymnaea stagnalis* (Gastropoda). Comp Biochem Physiol 69B: 877-880

WOUDRAK, G. (1969): Die Ultrastruktur der Zellen aus dem interstitiellen Bindegewebe von *Arion rufus* (L.), Pulmonata, Gastropoda. Z Zellforsch 95: 249-262

YAMAMURA, M.; HATAKEYAMA, S.; SUZUKI, K.T. (1983): Cadmium uptake and induction of cadmium-binding protein in the waterflea (*Moina macrocopa*). Bull Environ Conta. Toxicol 30: 298-302

YAN, K.; KHOSHNOODI, J.; RUOTSALAINEN, V.; TRYGGVASON, K. (2002): N-linked glycosylation is critical for the plasma membrane localization of nephrin. J Am Soc Nephrol 13: 1385-1389

ZAMPIGHI, G.A.; LOO, D.D.; KREMAN, M.; ESKANDARI, S.; WRIGHT, E.M. (1999): Functional and morphological correlates of connexin50 expressed in *Xenopus laevis* oocytes. J Gen Physiol 113: 507-524

ZAROOGIAN, G.; ANDERSON, S. (1995): Comparison of cadmium, nickel and benzo(a)pyrene uptake into cultured brown cells of the hard shell clam, *Mercenaria mercenaria*. Comp Biochem Physiol 111C: 109-116

ZAROOGIAN, G.; NORWOOD, C. (2002): Glutathione and metallothionein status in an acute response by *Mercenaria mercenaria* brown cells to copper *in vivo*. Ecotox Environ Safe 53: 285-292

ZHUANG, S.; SHAO, H.; GUO, F.; TRIMBLE, R.; PEARCE, E.; ABMAYR, S.M. (2009): Sns and Kirre, the *Drosophila* orthologs of nephrin and neph1, direct adhesion, fusion and formation of a slit diaphragm-like structure in insect nephrocytes. Development 136: 2335-2344

Part VI.

Appendices

A. Electron tomogram slices and their corresponding 3D model

Further 3D reconstructions of rhogocytes are presented in this part. The focus is given on the area of the slit apparatus. The figures show the slices of the reconstructed tomograms on the left and the corresponding 3D model in the right; otherwise it is indicated.

The following explanation of colors and abbreviations corresponds to all figures: The enveloping basement membrane (→m, salmon) surrounds each rhogocyte. The coated plasma membrane (c, cyan) makes some invaginations bridged by the cytoplasmic bars (b, green) that form the slits (→s) of approx. 20 nm with diaphragms (→d, magenta). The extracellular lacunae (→e) are either empty or filled with protein-like particles (→p, blue). Coated vesicles (v, yellow) inside an extracellular lacuna and the neighboring cytoplasm are also seen. Highly dense material (a, purple) is observed at the cytoplasmic bars adjacent to the slits; it is likely to contain actin bundles.

A.1. *Biomphalaria glabrata* rhogocytes

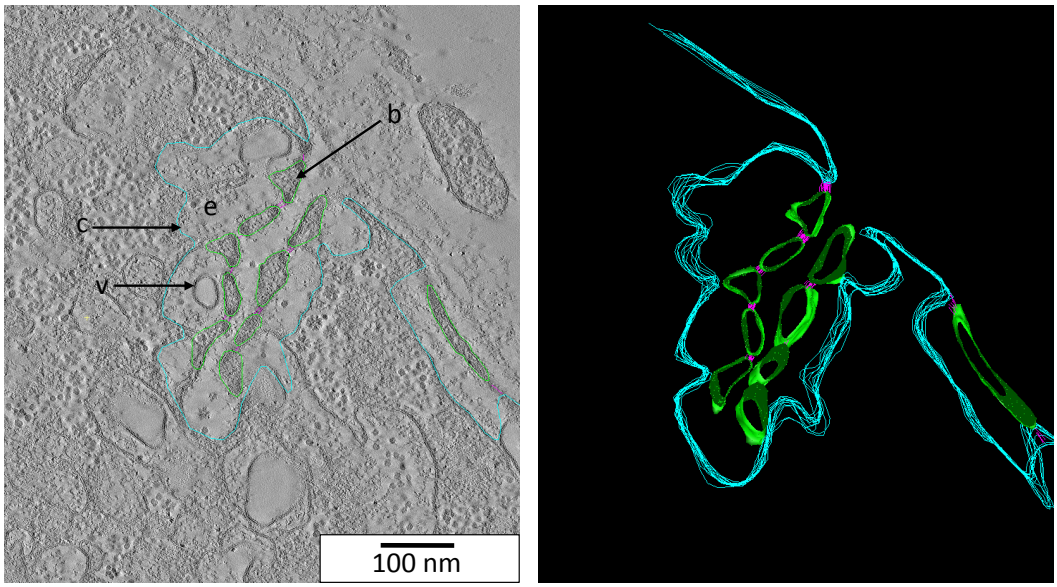

Figure A.1. ***3D ultrastructure of a rhogocyte region with slit apparatus, from B. glabrata.*** *Note the strong invaginations of the coated plasma membrane (→c) to form an extracellular lacuna (e) covered by cytoplasmic bars (→b). A vesicle (→v) is present inside the invagination.*

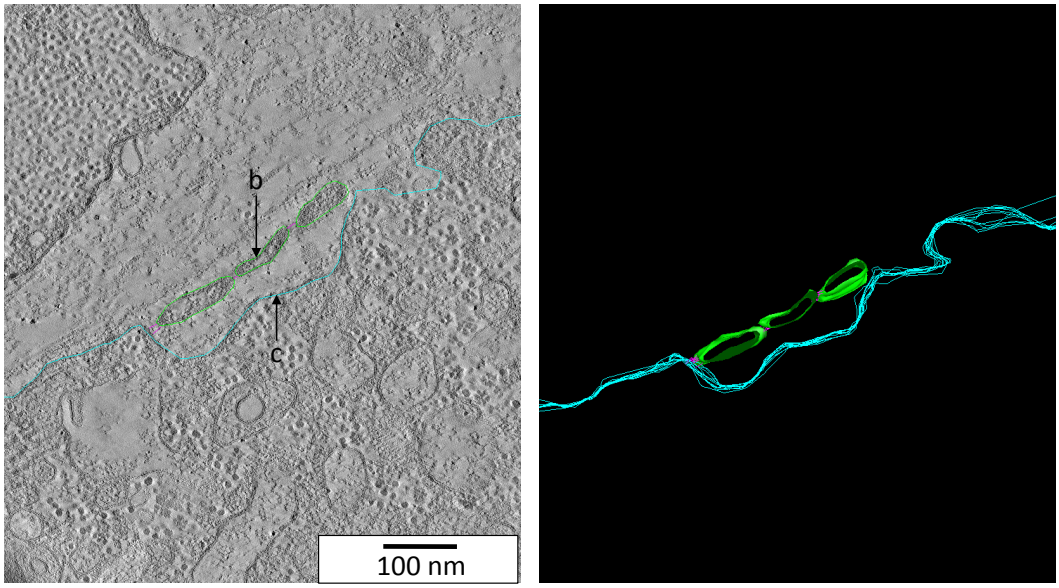

Figure A.2. ***3D ultrastructure of a rhogocyte region with slit apparatus, from B. glabrata.*** *(→b, cytoplasmic bar; →c, coated plasma membrane)*

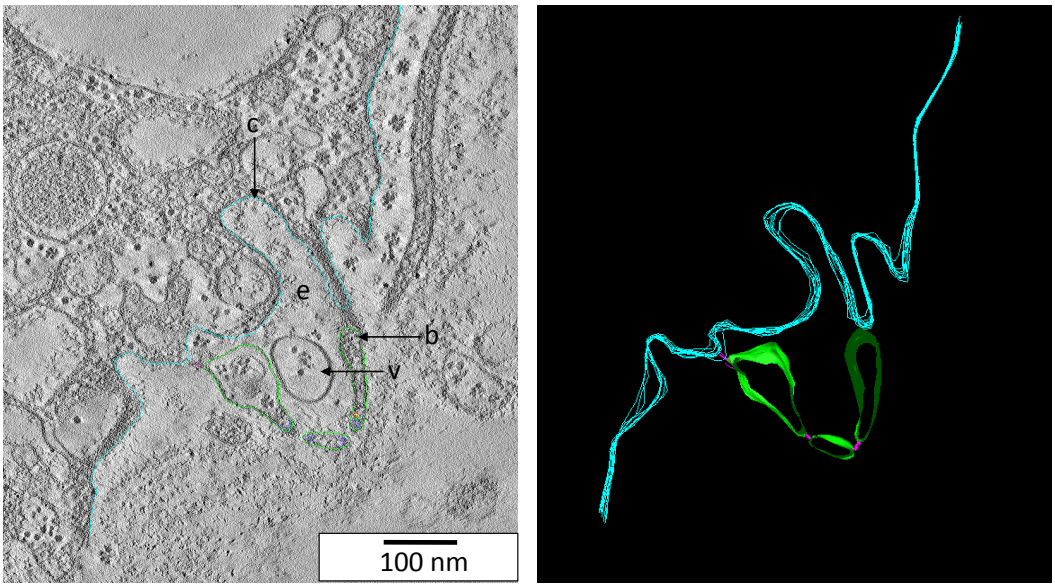

Figure A.3. ***3D ultrastructure of a rhogocyte region with slit apparatus, from B. glabrata.*** *Note the vesicle (→v) inside the extracellular lacuna (e) formed by the coated plasma membrane (→c). (→b, cytoplasmic bar)*

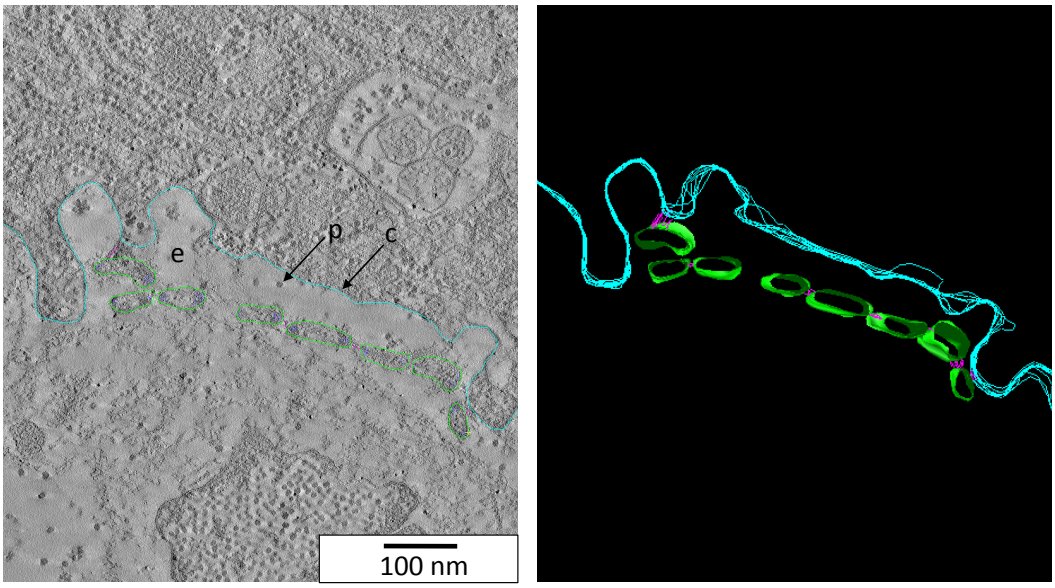

Figure A.4. ***3D ultrastructure of a rhogocyte region with slit apparatus, from B. glabrata.*** *The extracellular lacuna (e) formed by invagination of the plasma membrane (→c) filled with a few protein-like material (→p).*

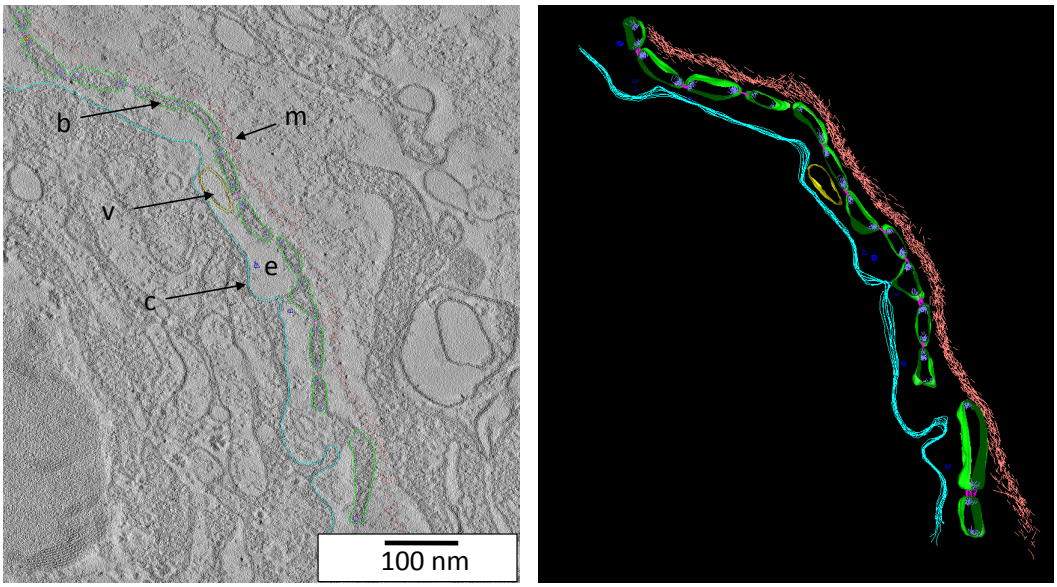

Figure A.5. ***3D ultrastructure of a rhogocyte region with slit apparatus, from B. glabrata.*** *Note the high number of cytoplasmic bars (→b) covering the elongated extracellular lacunae (e) that occasionally contains vesicles (→v). (→c, coated plasma membrane; →m, enveloping basement membrane)*

A.2. *Lymnaea stagnalis* rhogocytes

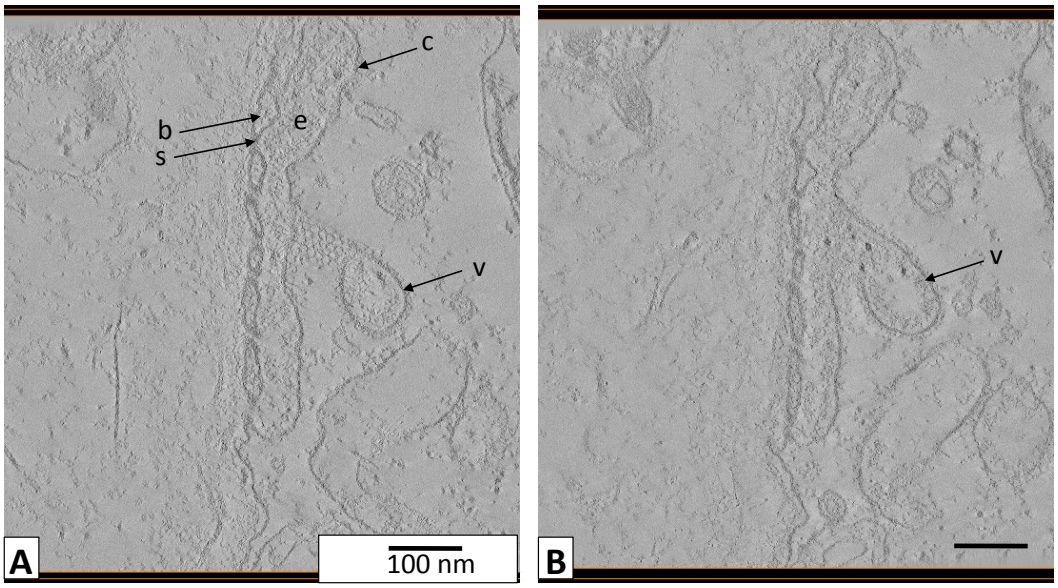

Figure A.6. ***Slices of the tomogram presented in Fig. 11.9 A (see Results), visualized here by Amira.*** *(A) A coated vesicle (→v) transporting material to or from the extracellular lacuna (e). (B) The same coated vesicle in open contact with the extracellular lacuna (view of a higher tilt during the collection of tilt series). (→b, cytoplasmic bar; →c, coated plasma membrane; →s, slit)*

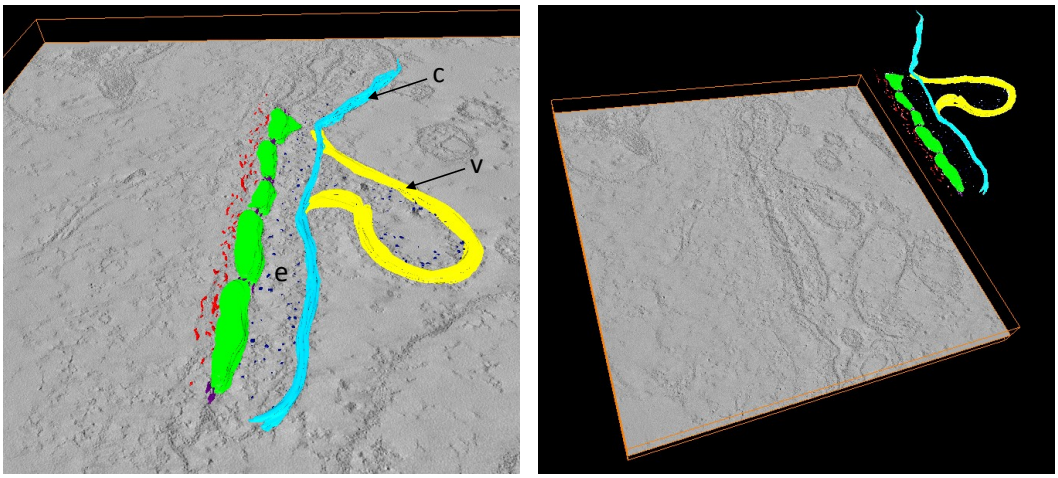

Figure A.7. ***Slices of the tomogram of a rhogocyte region with slit apparatus from L. stagnalis presented in Fig. 11.9 A (see Results), overlayed by a 3D model constructed in Amira.*** *Note a vesicle (→v) fusing with the plasma membrane (→c) beyond an extracellular lacuna (e).*

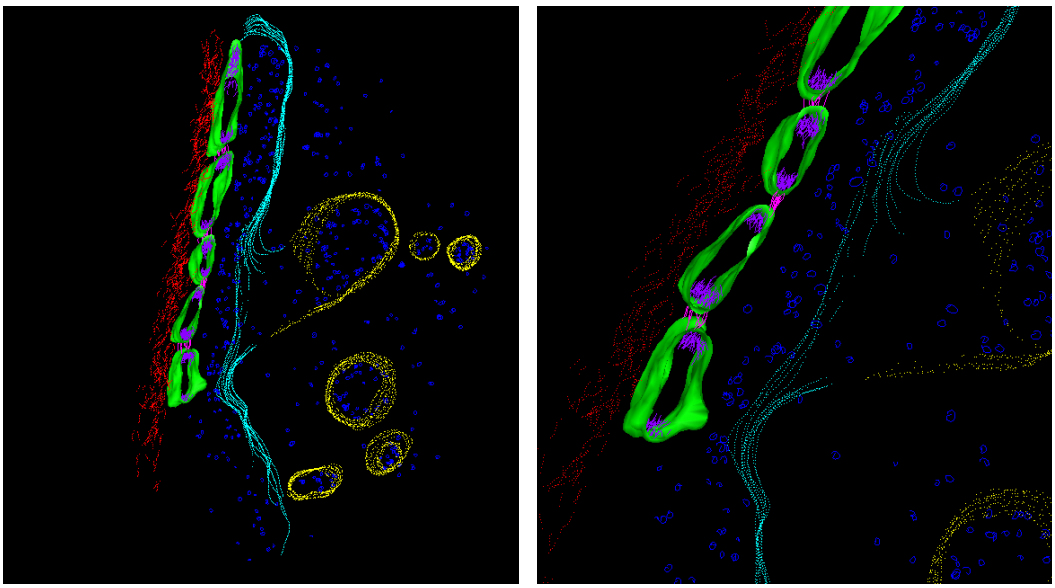

Figure A.8. ***3D model of a slit apparatus derived from the tomogram of an L. stagnalis rhogocyte presented in Fig. 11.9 A (see Results).*** *Note intracellular vesicles (yellow) containing protein-like material (dark blue) in the vicinity of, or partially fused with, the plasma membrane (cyan).*

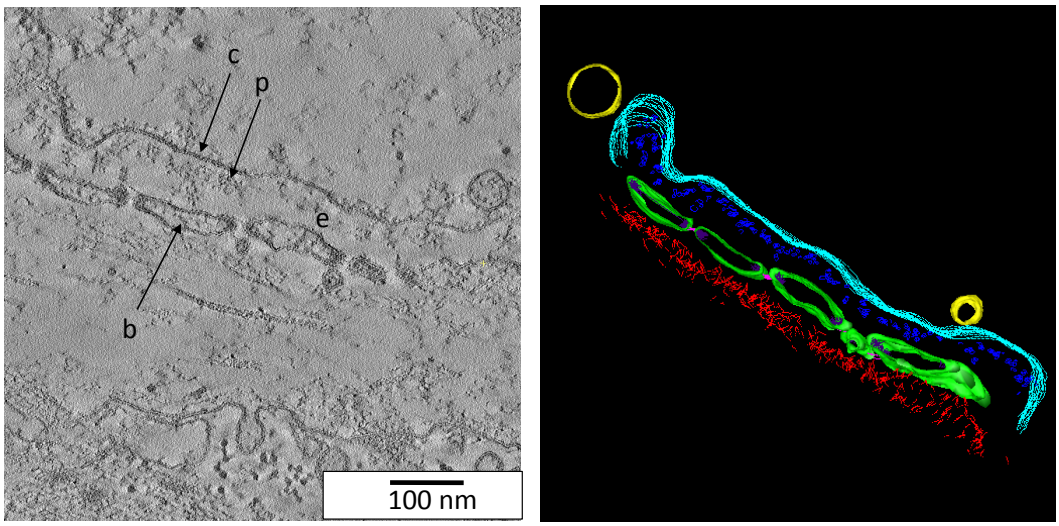

Figure A.9. ***3D ultrastructure of a rhogocyte region with a slit apparatus, from L. stagnalis.*** *Note the abundant protein-like material (→p) present in the extracellular lacunae (e). (→b, cytoplasmic bar; →c, coated plasma membrane)*

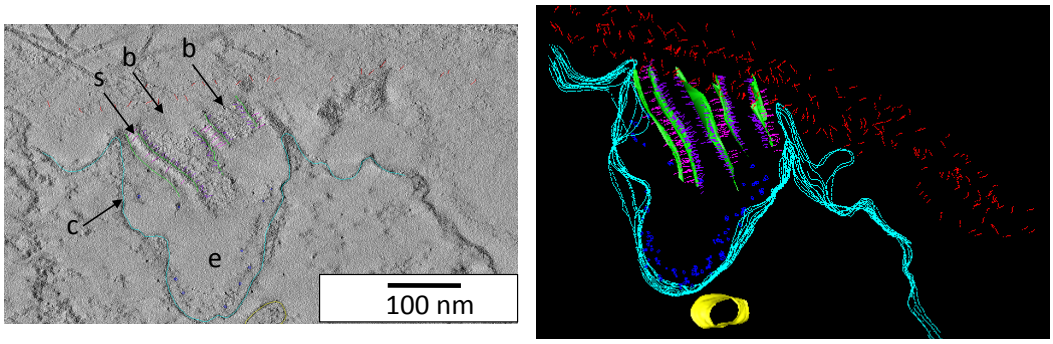

Figure A.10. ***3D ultrastructure of a rhogocyte region with a slit apparatus, from L. stagnalis.*** *The cytoplasmic bars (→b) are seen in longitudinal view. (e, extracellular lacuna; →c, coated plasma membrane; →s, diaphragmatic slit)*

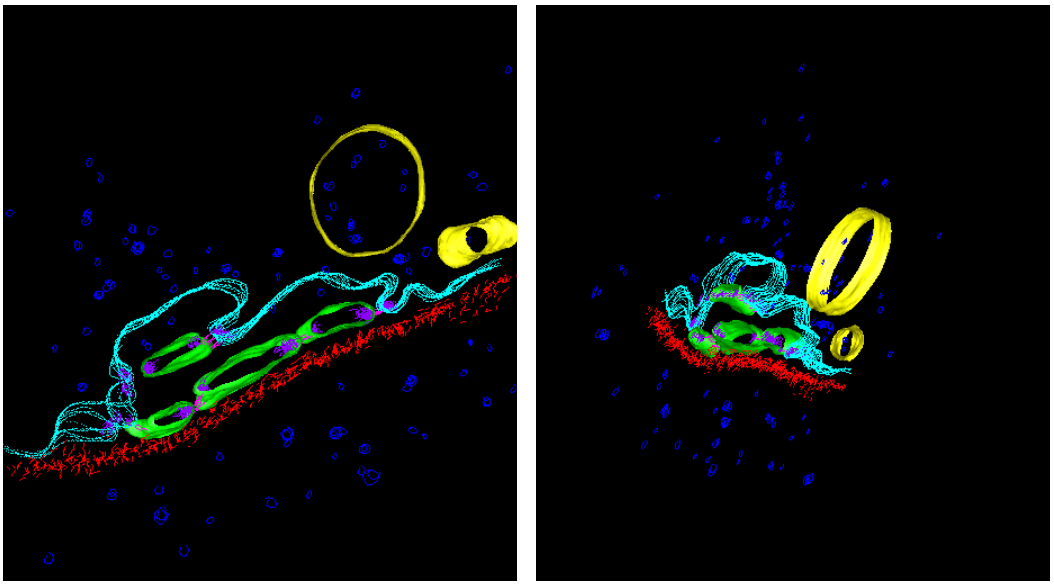

Figure A.11. ***Two different views of a 3D model derived from the 3D ultrastructure of a rhogocyte region with a slit apparatus and two intracellular vesicles, from L. stagnalis.*** *Note the protein-like particles (dark blue) visible outside of the cell, within the extracellular lacuna within the larger vesicle, and in the cytoplasm.*

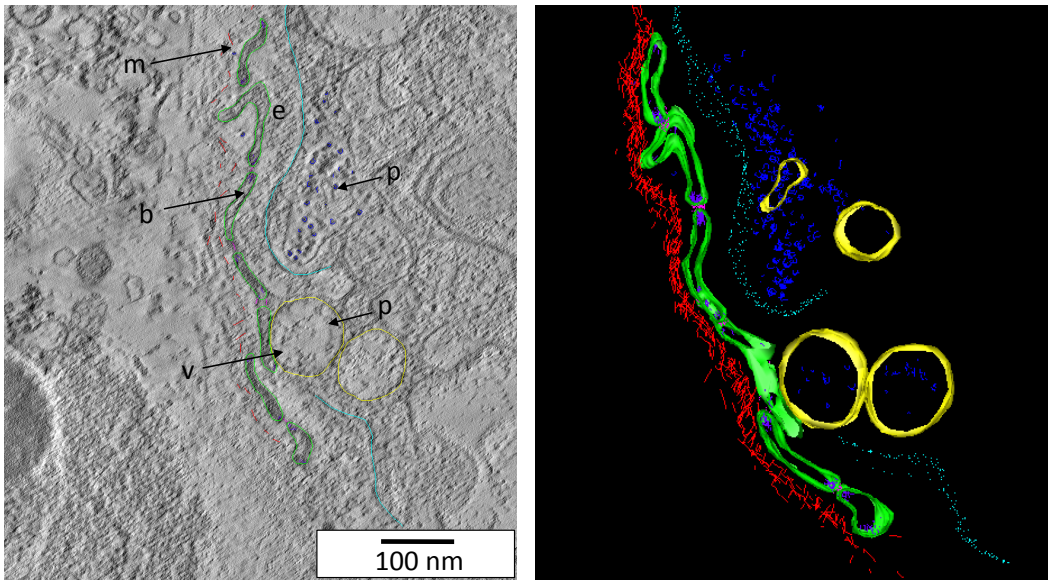

Figure A.12. ***3D ultrastructure of a rhogocyte region with a slit apparatus, from L. stagnalis.*** *It seems that vesicles (→v) transport material to the extracellular lacunae (e) formed by the coated plasma membrane (→c). (→m, enveloping basement membrane; →b, cytoplasmic bar; →p, protein-like material)*

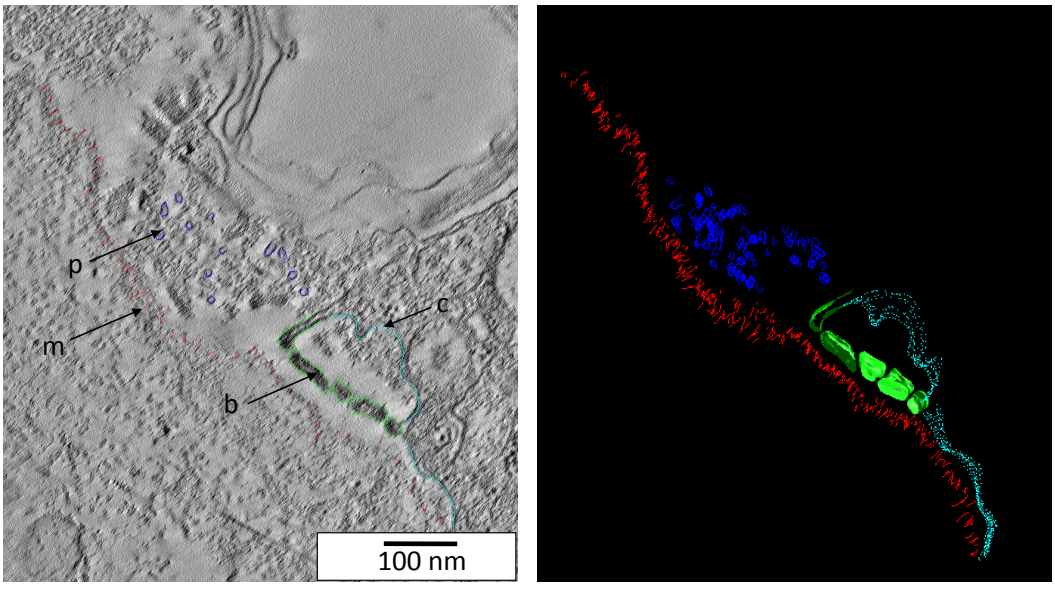

Figure A.13. ***3D ultrastructure of a rhogocyte region with a slit apparatus, from L. stagnalis.*** *Note the protein-like material (→p) resembling hemocyanin molecules in the vicinity of a slit apparatus with cytoplasmic bars (→b). (→c, coated plasma membrane; →m, enveloping basement membrane)*

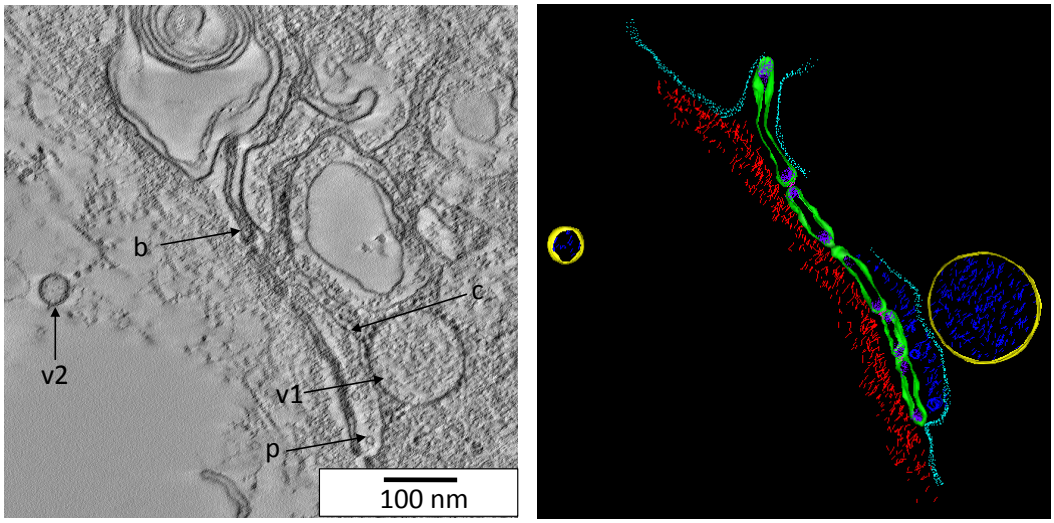

Figure A.14. ***3D ultrastructure of a rhogocyte region with a slit apparatus, from L. stagnalis.*** *A vesicle (v1) apparently loaded with protein-like material (→p) resembling hemocyanin molecules in close contact with the plasma membrane (→c) beyond a slit apparatus. Also note the extracellular vesicle (→v2). (→b, cytoplasmic bars)*

List of Figures

List of Tables

21. Acknowledgments

A skillful team is necessary for a successful Thesis. That is why I would like to say a sincere thank you to each and every person that was involved in this project. Every single contribution is deeply appreciated.

I would have never been part of this team, if [redacted] had not given me the opportunity to work at his group. I am grateful for his excellent support and guidance during my PhD studies; for his helpful discussions and comments, which were inspiring, his active role and critical view in this work, in the analysis and interpretation of the data and for correcting the manuscripts and this PhD Thesis.

The Max Planck Graduate Center, I would like to acknowledge for the honor of the grant and the financial aid for the past 3 years.

My gratitude is also directed to [redacted], my second supervisor, for her support and the time that she provided me for discussions and analysis of data. I also thank her group members [redacted], [redacted] and [redacted] for their excellent support during the cryo experiments.

I extend my appreciation to [redacted] and [redacted] for support and discussions, [redacted] and [redacted] for helpful discussions, suggestions and advices at the beginning of the project, [redacted] for his great contribution to the *in situ* experiments with *L. stagnalis* and to the nephrin analysis of *B. glabrata*, and [redacted] for his help with purifying the hemolymph proteins.

For the pleasant working environment and for the great time at the lab, I wish to thank all members of this group, past and present, [redacted]. My special thanks go to [redacted] for his great assistance with image processing and computer-related hurdles that occurred within the framework of this study, [redacted] and [redacted] for their contribution to the *in situ* experiments with *B. glabrata*, [redacted] for his assistance with the experiments done on the EDX-TEM and the students [redacted], [redacted] and [redacted], who worked on this project under my supervision, for their great contribution on the experiments. A great help during the experiments was [redacted] for taking care of the cultures of

B. glabrata and *L. stagnalis*, [redacted] for her guidance with immune-gold labeling and [redacted] for her excellent technical support during the experiments.

I would like to thank [redacted] and [redacted] for their great contribution in histological analyses; [redacted] and [redacted] for their technical assistance with paraffin-embedded samples.

I owe special thanks to [redacted] for critical reading of the manuscript of our paper from 2014 and for his valuable suggestions.

I thank all my friends, especially [redacted] and [redacted], for their great assistance and accompany that helped me throughout the difficult times.

I am forever indebted to my mother [redacted], my father [redacted] and my sister [redacted] for supporting me in every step I take. For their understanding, endless patience and encouragement when it was most required. You made who I am today.

Last but not least, I thank my partner in life, [redacted], for making everything easier with his constant love and affection and for standing by me to find the sun in every raining season.

22. Erklärung und Copyright

22.1. Erklärung

I hereby declare that I wrote the dissertation submitted without any unathorized external assistance and used only sources acknowledged in the work. All textual passages which are appropriated verbatim or paraphrased from published and unpublished texts as well as all information obtained from oral sources are duly indicated and listed in accordance with bibliographical rules. In carrying out this research, I complied with the rules of standard scientific practice as formulated in the statutes of Johannes Gutenberg-University Mainz to insure standard scientific practice.

Ort, Datum Maria Kokkinopoulou

22.2. Copyright